# HYDROKINETIC OSCILLATORS FOR ENERGY HARVESTING VIA COUPLING POLYVINYLIDENE FLUORIDE (PVDF) AND ELECTROMAGNETICS

by

**Alan Michael Hudzik II**

B.S. in Mechanical Engineering, University of Pittsburgh, 2007

Submitted to the Graduate Faculty of

the Swanson School of Engineering in partial fulfillment

of the requirements for the degree of

**Master of Science**

University of Pittsburgh

2009

UNIVERSITY OF PITTSBURGH

SWANSON SCHOOL OF ENGINEERING

This thesis was presented

by

Alan Michael Hudzik II

It was defended on

July 17, 2009

and approved by

William W. Clark, Ph. D., Professor of Mechanical Engineering Department

Lisa Mauck Weiland, Ph. D., Assistant Professor of Mechanical Engineering Department

Daniel G. Cole, Ph. D, Assistant Professor of Mechanical Engineering Department

Thesis Advisor: William W. Clark, Ph. D., Professor of Mechanical Engineering Department

# HYDROKINETIC OSCILLATORS FOR ENERGY HARVESTING VIA COUPLING POLYVINYLIDENE FLUORIDE (PVDF) AND ELECTROMAGNETICS

Alan Michael Hudzik II, M.S.

University of Pittsburgh, 2009

Sustainable energy generation has received a great deal of interest recently because the presence of greenhouse gases in our atmosphere is at an unprecedented high. There are multiple existing renewable energy sources but the most abundant of the known is hydro. Most of the hydro-energy is predicted to be present in the oceans but this thesis focuses on harnessing energy through inland river currents (known as hydrokinetic energy) because it has become apparent that there is still plenty of this energy to be extracted. Although an immature field, most of the work done to harness hydrokinetic energy has been through in-stream turbines such as the Derrius and Gorlov helical turbines. There is a concern that these in-stream turbines can have an adverse effect on their local environment [12], therefore, two other methods were investigated in depth: 1) a bender/flapper method and 2) an oscillating foil. The bender/flapper method was built and tested experimentally. A mathematical model was developed to analyze the potential of the oscillatory foil because the bender/flapper method did not meet expectations. Also, because of the advancement of smart materials, these two methods considered harnessing energy simultaneously through an electromagnetic inductor and piezoelectric material transducer.

## TABLE OF CONTENTS

## LIST OF TABLES

## LIST OF FIGURES

# 1.0 INTRODUCTION AND LITERATURE REVIEW

Renewable energy, in theory, is energy that has an infinite source because it is generated from such things as the sun, wind, or water. It is well understood that renewable energy sources must begin to take some of the burden off of the conventional fossil fuel energy sources for multiple reasons. One of the main reasons is the ever increasing costs of fossil fuel energy sources which adversely effect the economy. Among other reasons, new technologies that harness renewable energy sources increase the overall energy production for the growing demand of the population, but most importantly these renewable energy sources offset the harmful effects of greenhouse gases. Take, for example, the advances of wind capacity, which is highly unpredictable, has gone from essentially zero in the late 1970's to approximately 10,000 MW in 2006 [1]. Harnessing energy from water can be a more effective source of energy because water is approximately 1000 times more dense than air and it has a rather predictable occurrence in most cases. Scientists and engineers have realized that water power based energy, with the addition of improving conventional hydropower plants, has a great potential for higher energy production just like the wind energy sources did but even greater.

Roger Bedard of the Electric Power Research Institute (EPRI) defines hydrokinetic energy as the energy possessed by a body of water because of its motion [5]. A hydrokinetic project is defined as a project that generates electricity from waves or directly from the flow of water in ocean currents, tides, or inland waterways [23]. According to the Federal Energy Regulatory Commission (FERC), an informal definition of a hydrokinetic project is to convert hydrokinetic energy to electrical energy. These two definitions promote two major qualities of a hydrokinetic project: 1) it utilizes a renewable energy source; and 2) it allows the extraction of energy through moving water without impoundment or diversion required by conventional hydro power technologies [5].

A hydrokinetic project utilizes kinetic energy. This has traditionally meant there will be rigid body motion relative to two bodies accompanied by stresses and strains with in these bodies. Most dynamic devices harness electricity through electromagnetic induction but since the advancement of smart materials it may be worth investigating the possible applications that a smart material could have in producing energy as well. A smart material is a material that exhibits coupling between multiple domains, for example converting electrical signals into mechanical deformation or deformation can be induced and recovered through thermal stimulation [38]. This thesis focuses on the subclass of smart materials that produce a voltage when a stress is applied, and more specifically polyvinylidene fluoride (PVDF). The ability of these materials to produce a voltage means that a current will be able to flow and hence electrical energy will be produced. A hydrokinetic system can produce forces which can be utilized to apply a stress to said smart material. In the system developed here, while harnessing energy from the smart material there will be rigid body motion, therefore, coupling of the smart material to an electromagnet is possible for maximum power production.

The goal of this thesis is to design a hydrokinetic device that harnesses energy through the coupling of smart materials and electromagnetic induction. Two methods were investigated in depth: 1) benders/flapper method and 2) oscillating foil. The bender/flapper method was investigated because it is the simplest oscillating device that could be built and tested for experimentation and analysis. The oscillating foil method was explored because the bender/flapper method did not meet expectations and therefore a mathematical model of this design was constructed and analyzed through the use of Matlab.

## 1.1 THESIS PROBLEM

The central obstacle of this work is to design a hydrokinetic device with the following three major requirements:

1. The device must be considered an in-stream, continuous flow device, meaning that it can harness energy from uni-directional currents.

2. The dynamics of the device must not be rotational (e.g. not like a turbine).
3. The dynamics of the system are not velocity dependent/sensitive.

The first requirement must be satisfied because it is an inherent constraint to this specific project. The second requirement is desirable because coupled with the first requirement non-rotational generators make up an extremely immature technology. The Department of Energy (DOE) separates hydrokinetic devices into two broad categories, rotating and wave energy conversion devices. In 2005 the DOE workshop states that "Rotating machines are designed to be deployed within a stream or current, capturing energy from the flow of water across or through the turbine (which may take various forms) to power a generator without impounding or diverting the flow of the water resource". The workshop sub classifies these rotating devices into horizontal and vertical axis turbines and then states that, "Other types of in stream devices have been proposed, for example, oscillatory devices and hydro venturi turbines; however none of them are developed to the point of significantly affecting the emergence of this new technology" [5]. Therefore, this led to the development of a device in this thesis that has oscillatory dynamics. Another motivation for choosing a device with oscillatory dynamics is that there is a concern that in-stream turbines can have an adverse effect on their local environment [12]. The third requirement is desirable because it will be shown that natural river streams can have an annually fluctuating flow velocity where flow dependent systems can not operate effectively. Unfortunately, this rules out the method of exciting a system with vortex induced vibrations, which is a powerful method to oscillating a structure. Section 1.3, 'The Pros and Cons of the VIVACE and Wingmill', shows why this is the case.

## 1.2 THE POTENTIAL OF HYDROKINETICS AND EXISTING DEVICES

According to the Energy Information Administration (EIA) from 2003 to 2007 water was the leading renewable energy source for generating and consuming electrical power in the United States, as shown in Figure 1 [7]. The renewable hydropower generation data given is for conventional hydroelectric plants only.

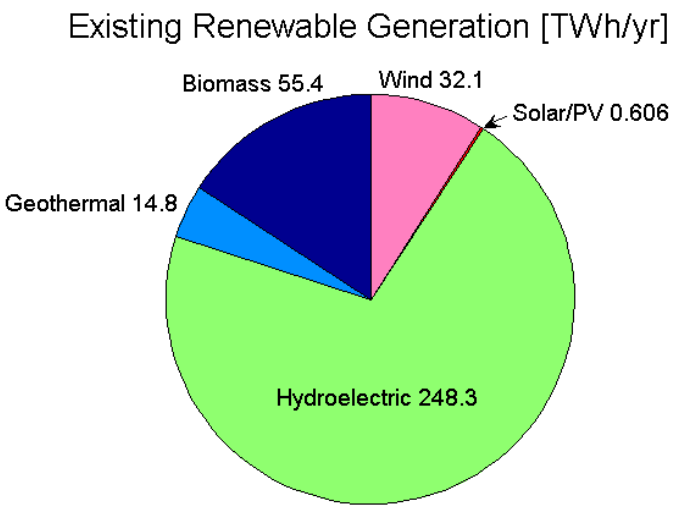


Figure 1: Existing Renewable Energy Generation [7].

These conventional hydroelectric plants are only operational where well suited waterways are accessible because the construction of a dam is necessary. Currently there are in-stream devices undergoing research to attempt to harness *wasted* energy from streams and waterways that conventional hydroelectric plants can not extract. The need for these devices is becoming more and more evident as the U.S. DOE workshop reports that, "Given that hydrokinetic devices can be deployed in any water resource having sufficient velocity to drive them, their energy generation potential is gargantuan" [5], and EPRI reports that, "The assessment of water resources with hydrokinetic energy potential has been limited to date, although the preliminary studies indicate a significant resource is available" [1]. Obviously, according to the U.S. DOE and EPRI there is energy 'out there', but the question then becomes how much is *gargantuan* and how much is *significant*? EPRI and the U.S. DOE both clearly state that the potential for natural river in-stream energy conversion (RISEC) devices have been researched on a limited basis. The main basis of information for an approximation of the potential of energy production of these devices is taken from Miller et al. [43] who estimates the total potential as 12,500 MW which according to EPRI [1] may be a

conservative number. EPRI also states that, "The uncertainty of this estimate,", given by Miller et al., "and the lack of a clear definition of the resource clearly points to the need for further research". Because of the preceding statements the amount of hydrokinetic energy available in the United States is obviously an open-ended research question that needs to be answered and the following potential hydrokinetic energy numbers for the RISEC devices need to be evaluated with caution. According to Figure 2 the RISEC devices constitute about 26 % of the total potential hydrokinetic energy production. As previously mentioned, some of these devices are currently under research and development. The following sections elaborate on some of these devices to show some of the benchmarks and expectations that have been set for new hydrokinetic designs.

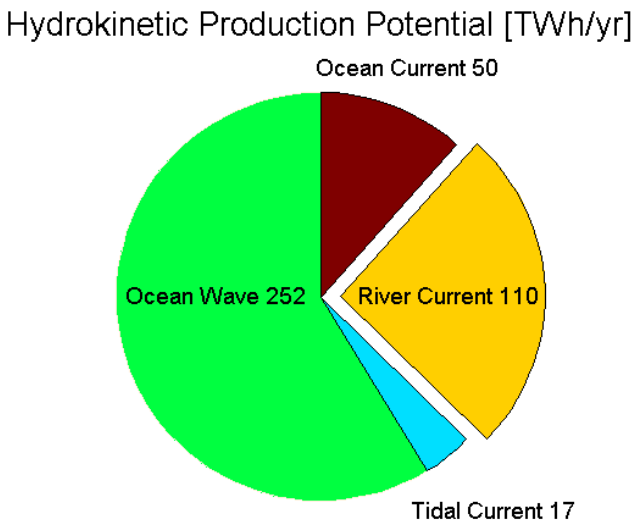


Figure 2: Potential Hydrokinetic Energy Production (EPRI) [1].

### 1.2.1 Wave Energy Conversion Devices

According to Figure 2, a considerable portion of the potential hydrokinetic production is predicted to come from the wave energy conversion devices. This type of hydrokinetic device is not the topic of this thesis, but for completeness and because wave energy conversion devices

currently contribute major aspects to the field of hydrokinetics it is worth mentioning. The current four major wave energy conversion devices are shown in Figure 3.

(a) Pelamis

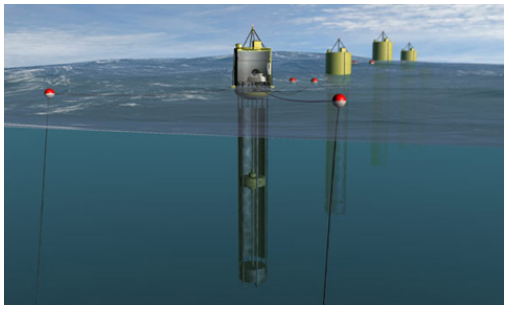

(b) Aquabuoy

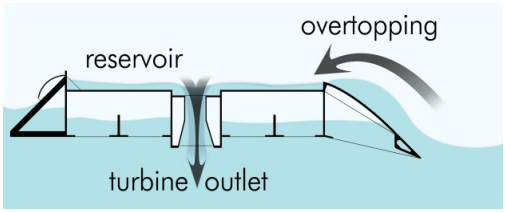


(c) Wave Dragon

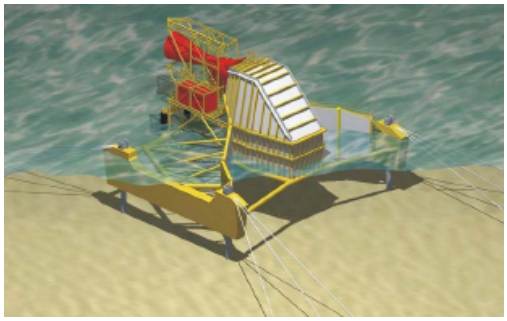

(d) Oceanlinx

Figure 3: The four major wave energy conversion devices

The Pelamis, seen in Figure 3(a), has cylindrical sections partially filled with air that pitch and yaw relative to each other. The joints resist this motion with hydraulic rams by pumping high-pressure fluid through hydraulic motors that drive electrical generators to produce electricity. A typical Pelamis model is approximately 140 m long and 3.5 m in diameter and is rated at approximately 750 kW [8]. The Aquabuoy, shown in Figure 3(b), is categorized as a point absorber that consists of four components 1) Buoy, 2) Acceleration tube, 3) Piston, and 4) Hose Pump. A small cluster of Aquabuoys is said to be able to produce power of a few hundred kilowatts while an array could supply several hundred megawatts [24]. It is unclear how many devices would be considered a small cluster and how many devices would be considered an array. The Wave Dragon system, seen in Figure 3(c),

is an overtopping device that raises waves above sea level into a reservoir where the water is then let out through turbines [10]. Depending on the location (depth of the ocean) and size of the specific the device, a Wave Dragon has a rated power production per unit from approximately 20 kW up to 11 MW [10]. The Oceanlinx, shown in Figure 3(d), is a device that utilizes air as the fluid that rotates the turbine. Water inside a chamber that is open underneath the waterline rises and falls, compressing and displacing the air inside. A single Oceanlinx unit is said to be able to generate peak power outputs between 100 kW and 1.5 MW, depending on the wave climate [46].

### 1.2.2 In-Stream Devices

An in-stream device is considered to be a device that harnesses energy from a current. Referring to Figure 2 ocean, tidal, and river are three distinct types of currents from which a hydrokinetic device can harness energy. Some existing turbine devices operate in ocean and tidal currents that can change direction. One way to accommodate the change in current direction is to allow a turbine to yaw or rotate to allow the turbine blades to always be positioned downstream. Figure 4 shows this type of device.

Figure 4: 35 kW turbine with downstream 3-bladed rotor, 5 m diameter that has the ability to yaw to accommodate reversing flow [28].

Another way to accommodate this change in direction is to reverse the rotation direction of the turbine blades. This model can be seen in Figure 5 which is the Open-Centre turbine that has a 6 m diameter and is rated at a 250 kW capacity [55].

Figure 5: The Open-Centre Turbine

Although very similar in application, the yawing turbine is not the type of device that would be utilized in river current flow. In the text of this thesis an in-stream hydrokinetic system will be defined as a device that utilizes current flow that is unidirectional at *all times* and refers to the extruded piece titled river current in Figure 2 for energy production. Roger Bedard, EPRI Ocean Energy leader, classifies four major types of in-stream kinetic energy conversion devices [15]:

1. Horizontal Axis Turbines
2. Vertical Axis Turbines
3. Hydro Venturi
4. Oscillatory

As reported by Bedard some of the many benefits of these types of devices are [15]:

- One of the most environmentally friendly of the known electricity generation technologies
- Predictable and therefore dispatchable
- Minimizes the 'Not In My Back Yard' mentality
- Creates jobs and develops local economies

There are also some cons that come along with these pros. For example, at first glance it does appear that in-stream devices are extremely environmentally friendly on a macro-scale because there is no requirement for diversion or impoundment. But as Miller states, "The field of hydrokinetic energy extraction is immature. Little is known about their performance in the river environment, and their risk of impingement, fouling, and suspension of sediments", Miller then adds, "It is clear that more research is required in hydrokinetic energy extraction with emphasis towards lower environmental and ecological impact" [44].

Along with the general pros and cons of in-stream devices, there are also many pros and cons that exist between the specific devices. A few examples would be that a rotating device could potentially be more harmful to nearby fish as compared to an oscillatory device, or an oscillatory device may be more sensitive to flow rates than rotational devices. An in depth look at some of these devices provides a more detailed look at how they behave.

#### 1.2.2.1 Rotating Devices and The Hydro Venturi

Horizontal Axis Turbine

There are two main types of rotating devices, they are the horizontal and vertical axis turbines. Probably the most recognizable and mature hydrokinetic device is the horizontal axis turbine because it closely resembles a modern wind turbine. This device was considered in 2005 to be the most economical overall solution for first generation devices [4]. The horizontal axis turbine is oriented to allow the rotor blades to rotate in a plane perpendicular to the axis, which is oriented into the direction of the fluid flow [5]. One of the more popular horizontal axis turbines is the Verdant Power model shown in Figure 6(a). A six turbine array, rated at a 200 kW capacity, was installed in the east canal of the East River in New York City [9].

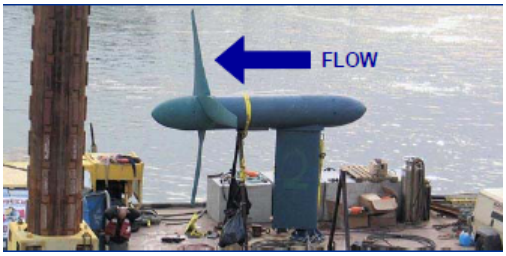


(a) Verdant Power

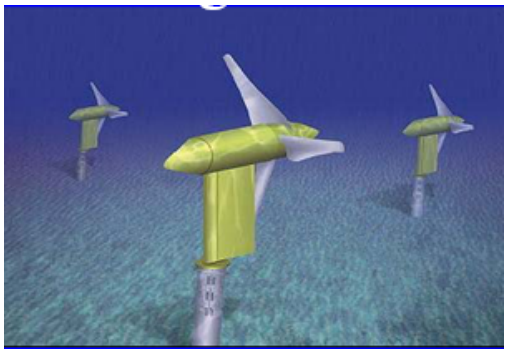

(b) Array

Figure 6: The Horizontal Axis Turbine a) Verdant Power design b) Array of horizontal axis turbines.

Vertical Axis Turbine

Vertical axis turbines have their blades oriented in line with the axis instead of perpendicular to it [5]. Figure 7 shows two different models of a vertical axis turbine [27].

The Darrieus turbine, Figure 7(a), is one of the earliest types of cross-flow wind turbines developed and was modified using straight blades for hydro applications [5]. As with many first generation devices the Darrieus turbine has many disadvantages. The main flaw in the design was that it experienced instabilities causing the device to rupture due to vibrations [17]. The other flaw with the Darrieus turbine is that it is not self starting [5].

Around 1990 Alexander Gorlov developed the Gorlov Helical Turbine (GHT), shown in Figure 7(b), it can be considered a second generation Darrieus turbine. This turbine orients its blades in a helical arrangement which not only suppresses the vibration problem but it is also self starting. Because the original intent of the GHT was meant for unidirectional flow it will be considered in this section of the thesis. It actually turns out that the design allows the turbine to continue to rotate without yawing or reversal of rotation regardless of the direction of current, therefore the GHT can be installed in any tidal, ocean, or river currents. Another major contribution of the GHT is it increased efficiency of the Darrieus turbine, which was 23 % to 35 % [17]. On March 19, 2002, a six blade, 2 m GHT was installed in the Uldolmok Strait which is a tidal channel that runs between the western coast

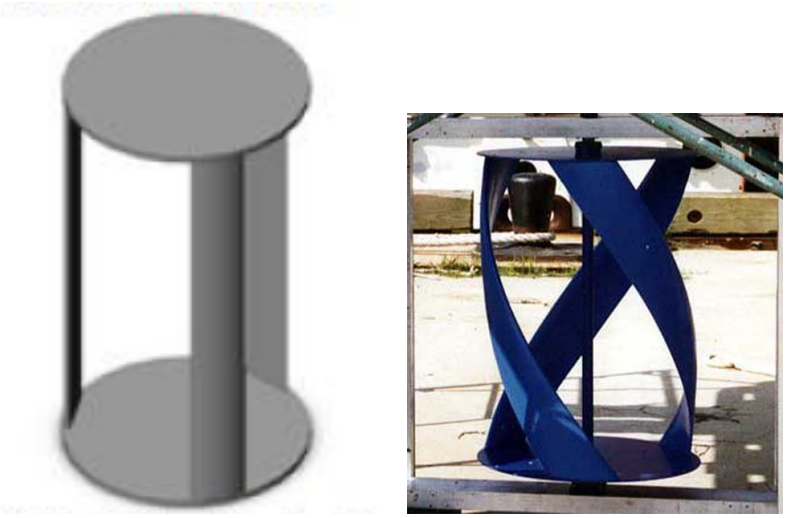

(a) Darrieus (b) Gorlov

Figure 7: Vertical axis turbine model a) The Darrieus Turbine b) The Triple Blade Gorlov Helical Turbine

of the Korea Peninsula and Jindo Island. The device was reported to produce 210 kW with currents up to 6.17 m/s [26].

Hydro Venturi Device

The Hydro Venturi device (HVD), originally invented by Dr. Geoff Rochester, is a completely different type of system than the rotating devices. According to Rochester, the disadvantage of the conventional underwater systems is that in order to access the energy of the fluid flow the moving parts are placed underwater in a hostile environment. Rochester proposed a solution to this deficiency by extracting energy from the fluid by pumping it away from the flow so that it can be led to a turbine which is positioned remotely from the underwater fluid flow in hopes of preventing high maintenance costs because of the absence of moving parts underwater [47]. Meison describes this device the following way, "This system consists of an open venturi tube, which uses the venturi effect to accelerate the water flow. While the water is accelerated, a pressure reduction is generated in the most constricted

point, under atmospheric pressure. Subsequently, the pressure gradient force (from high to low pressure) is used to move conventional turbine inside the tube which is connected with the constricted point" [42]. More information on this device can be found at the company website www.hydroventuri.com. The HVD can be seen in Figure 8.

Figure 8: The Rochester Hydro Venturi system

#### 1.2.2.2 Oscillating Devices

The Stingray

There are very few oscillatory devices currently being used today. One of the more well known oscillatory devices is the Stingray designed by Engineering Business Ltd., shown in Figure 9.

Engineering Business claims that the Stingray can not operate in uni-directional flow, but the description of the devices operation makes it seem as if it could. The key component of the Stingray is the wing-like hydroplane supported on a perpindicular pivotal arm. As tidal currents pass over the hydroplane, lift and drag forces cause it to ascend or descend

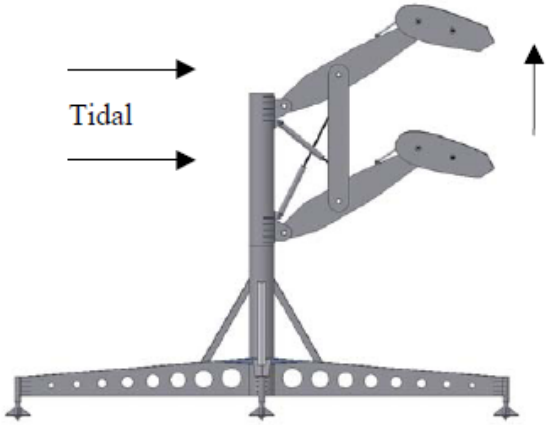


Figure 9: The Stingray system by Engineering Business

according to the angle of the hydroplane. Hydraulically powered cylinders are used to alter the hydroplane's angle such that the apparent angle of attack, relative to the oncoming current, is maintained at its optimum angle; and as the angle of attack is altered so too is the direction of the force from the flow on the hydroplane, thus allowing the device to oscillate relative to its stationary base [56, 14]. The resulting motion is slow and oscillating with constant amplitude and varying speed relative the fluid flow velocity. The first Stingray was submerged in 2002 and was able to generate 150 kW on average for a whole year [58].

Vortex Induced Vibration for Aquatic Clean Energy

Probably the second most well known oscillatory device is the Vortex Induced Vibration for Aquatic Clean Energy, a.k.a. VIVACE, system. This is probably the most mature oscillatory hydrokinetic system for use in unidirectional flow although it has not yet been tested in practice. The VIVACE utilizes vortex induced vibrations (VIVs), a highly non-linear phenomenon in which a fluid interacts with a solid structure. VIVs are the underlying effect in collapsing the Tacoma Narrows Bridge in 1940. Figure 10 shows the VIVACE in its simplest form, which consists of a rigid cylinder mounted to elastic supports [25].

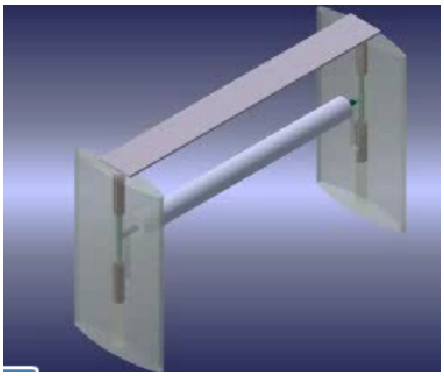

Figure 10: The VIVACE system

The VIVACE system has been tested in the LTFS Water Channel at the MHLab of the University of Michigan and has been reported to generate energy at 22 % efficiency at a fluid flow velocity of approximately 0.8 m/s [16]. No reports on the amount of power the VIVACE can produce have been found.

The Wingmill

Wing flutter is a phenomenon known most famously to occur in aeroplane wings. When a wing is able to oscillate in both the pitch and plunge degrees of freedom then power may be transferred from the fluid to the interacting wing, hence a wing can produce power [21]. This was the basis for the invention of the wingmill invented in 1981 by McKinney and Delaurier [40], which was intended for use in air. McKinney and Delaurier described the device as a windmill that consists of a rigid horizontal wing oscillating in plunge (vertical translation) and pitch. The model is shown in Figure 11.

None of the previously described devices can be classified as an in-stream device that has oscillatory dynamics that do not arise from VIVs except for the wingmill. The wingmill does operate in unidirectional flow, it is oscillatory and not rotational, and it does oscillate not because of VIVs but because of the coupling of pitching and plunging. Therefore, the

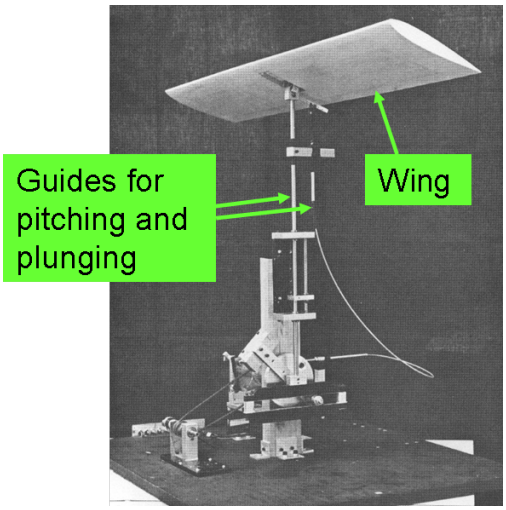


Figure 11: Original Wingmill System by McKinney and Delaurier

wingmill will become one of the primary focuses of this thesis because almost twenty years later it was redesigned to be tested in water thus categorizing it as in-stream hydrokinetic device. The redesigned wingmill is shown in Figure 12 and its mechanics of operation are shown in Figure 13 [35].

The design and operation of the wingmill designed by Jones et al. [35] is described as follows:

- The mechanism has two rails that extend vertically which have grooves cut in them
- Bearings attached to the wing slide up and down in these grooves guiding the plunge motion
- As the wing plunges the thin, airfoiled pushrods attached to the bearings couple to the swing-arms via ball-joints and the swing-arm is forced to rock
- Through a series of linkages, the rocking swing-arm rotates a phasing gear which rotates a shaft driving the pitch-arm
- A linkage from the pitch-arm drives the bell-crank back and forth, which in turn pitches the foil

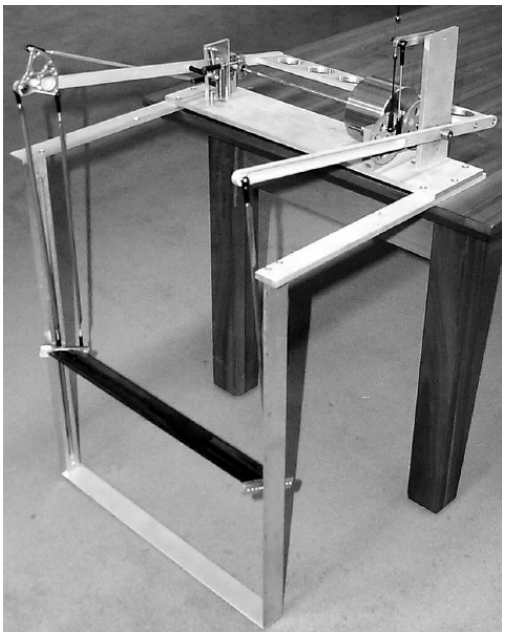

Figure 12: Redesigned Wingmill System to be used as a hydrokinetic device

Jones also modeled a different type of underwater wingmill shown in Figure 14. This model of the wingmill shows its ability to be connected in some form of an array for higher levels of power production. More information on this design can be found in reference [39].

With respect to the wingmill a power coefficient, $C_p$, is defined as the area swept out by a wing divided by the wing area itself. Lindsey [39] claims that one single oscillating-wing generator operating at a power coefficient, $C_p$, of 0.25, and wings with a total area of 0.5 $m^2$ placed in a free stream velocity of 3.7 m/s could produce approximately 3.4 kW, which was enough to power the average household in 1997. The same generator with a $C_p$ of 0.4 could provide the same energy with a free stream velocity of 3.2 m/s. If less energy is needed than the approximate 3.4 kW then either a slower free stream velocity or a smaller generator would suffice.

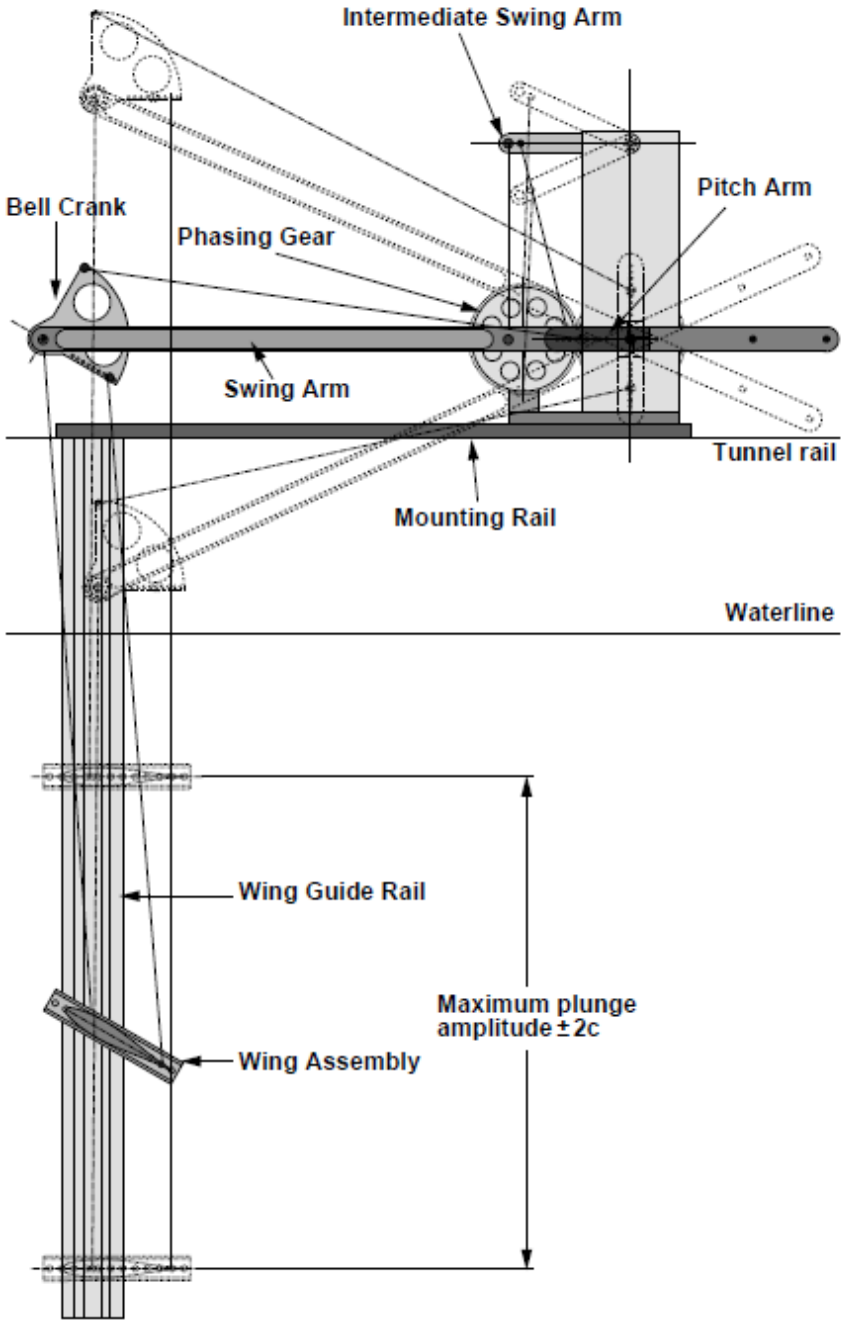


Figure 13: Wingmill System

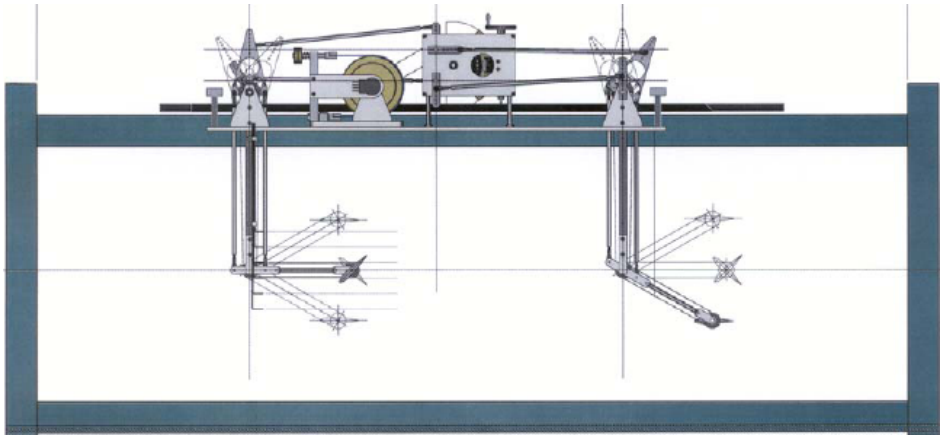

Figure 14: Second Wingmill System

The Fluttering Flag and Piezo-bimorph

All of the devices previously mentioned create electrical energy via electromagnetic induction. There is another type of in-stream oscillatory device that is considered completely unconventional. This device, designed by Pobering and Schwesinger [48], has no rotating or relative motion parts that need maintenance and only consists of elastically deformable membranes. This device is based on the idea of smart materials that consist of electrodes on their surface to collect generated charges. Pobering and Schwesinger designed two similar devices, including the fluttering flag shown in Figure 15(a) and a microstructured piezo-bimorph shown in Figure 15(b).

It is obvious from Figures 15(a) and 15(b) that both of these devices are highly dependent on flow velocities just like the VIVACE system. Pobering and Schwesinger claim that, "Power ratings of 71 $\mu$W per element could be achieved resulting in a power density of 70 W/m$^3$ using the common mechanical theory". Although it has been shown that large quantities of smart materials would be required to develop a considerable amount of energy, it may be possible to couple these materials to a new or existing device that harnesses energy through electromagnetics. In doing this the smart material may be able to add to the sytems power

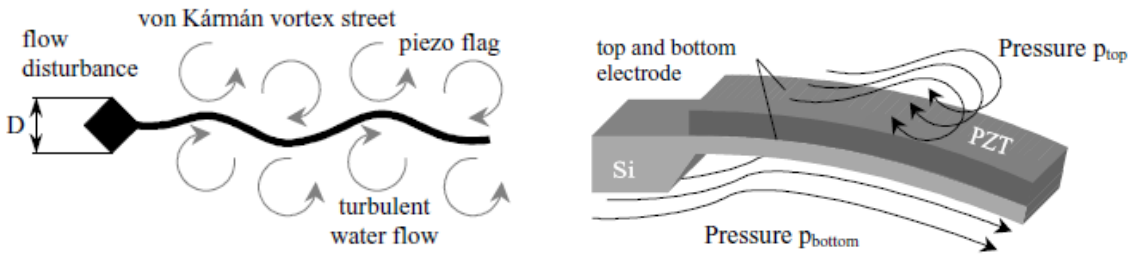


(a) Fluttering Flag

(b) Microstructured Piezo-Bimorph

Figure 15: Novel hydropower harvesting devices a) Fluttering flag in Von Karman's vortex street b) Piezo Bimorph Generator

rating, for example, in 2005 Priya et al. [50] utilized twelve piezoelectric bimorph actuators (each having a volume of $60\times20\times0.5$ $m^3$) arranged along the circumference of a windmill and generated an extra 10.2 mW of power. Although the device Priya et al. created is a wind energy transducer, this same concept could be transposed into a hydrokinetic device, which will be addressed in chapters 3 and 4.

Most applications for piezoelectric generators have been for micro up to millimeter scales, and are low power devices. Some examples of these applications are to power wireless devices such as temperature sensors [53], or to power either a front or rear lamp on a bicycle for lighting [45]. There has been some focus on possibly utilizing these piezoelectric materials on a macro scale, but it seems from literature that most of the attention has been concentrated on using piezoelectric generators for wave energy conversion devices [54, 18, 22, 19] with only limited interest in using the piezoelectric generator in a river current [37].

## 1.3 THE PROS AND CONS OF THE VIVACE AND WINGMILL

The wingmill and VIVACE systems are similar because they both harness energy from unidirectional flow, they are oscillatory in nature, and they are both environmentally friendly. The main difference between the two devices is the underlying effect that excites each par-

ticular system. As mentioned before the VIVACE uses vortex induced vibrations and the wingmill utilizes the coupling of pitching and plunging. The effects of this difference can easily be seen when considering the response of the two systems to a varying free stream velocity input. The response of the wingmill is analogous to a high pass filter because once a specific free stream velocity is achieved there will be an oscillation which in turn will produce a certain level of power. There is a threshold for the velocity because the force of the water on the foil must overcome mass and friction forces. In theory as the free stream velocity is increased the device will simply oscillate faster and faster thus producing higher and higher levels of power. The VIVACE on the other hand does not have this characteristic because of the nature of vortex induced vibrations. The response of the VIVACE is analogous to a band-pass filter when compared to an increasing free stream velocity. As shown in Figure 16 the response of the VIVACE system, for a specific cylinder length and diameter, has a significant response between approximately 0.5 m/s and 1 m/s which is about a 0.5 m/s 'bandwidth'. The effective 'cut-off' velocities of the VIVACE response shown in Figure 16 could be translated along the free stream velocity axis for a different length and diameter cylinder.

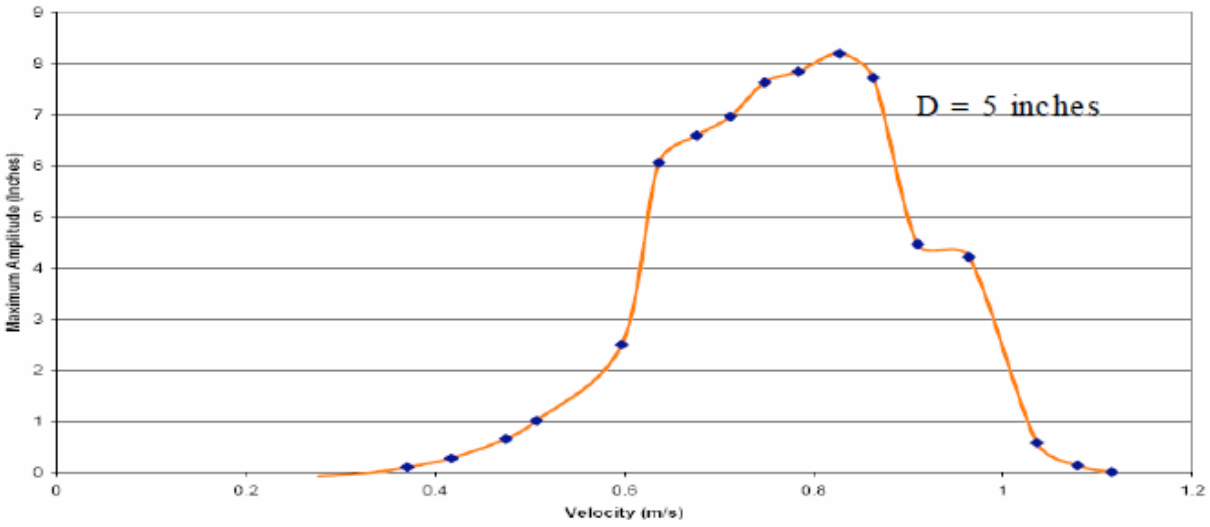


Figure 16: VIVACE response for a specific cylinder

The reason why this difference is significant is because when the variation in natural river velocities are taken into consideration, the VIVACE system does not seem to be such a feasible source of energy. Previsic and Bedard [49] conducted a feasibility assessment to determine the potential of RISEC devices in specific sites in Alaska. During their study of the several different sites taken into consideration, they determined monthly averages of river velocities. For example, one of the sites they examined was the Tanana River at Big Delta (Station ID: 15478000 according to USGS) which gave the data shown in Figure 17 for monthly averages of river velocity.

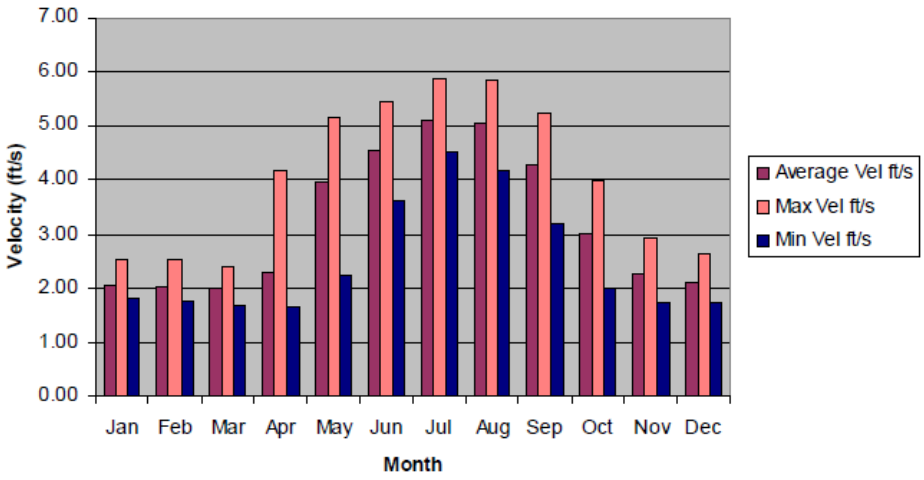


Figure 17: Average flow velocity data for the Tanana River

According to Figure 17 the 'bandwidth' of velocities is about 2.5 ft/s to about 5.9 ft/s which is about 0.76 m/s to 1.8 m/s giving an effective 'bandwidth' of approximately 1.04 m/sṪhis is about twice the 'bandwidth' of the response given by Figure 16 meaning unless the dimensions of the cylinder were changed when needed, this device would not produce energy for some extended times of the year in this river. Another river taken into consideration for the sake of this argument is the Kiskimenitas River at Vandergrift (The Kiski). Discrete data measurements from the USGS [59] was given for only a few specific times of the year, but the significance of the data is to show how much variation there is in river flow velocity where high amounts of rainfall is known to occur. Table 1 illustrates these variations and as can be

seen there is a wide range of variation throughout the year for flow rates. Any device that is bandlimited due to flow rates would not be the most efficient system for hydrokinetic energy extraction in this river as well. These two rivers were taken into consideration because the EIA deemed them as possible candidate sites for future hydrokinetic projects.

Table 1: Average flow velocities of the Kiski

| Date | Flow Velocity (m/s) |
|---|---|
| 10/01/07 | 0.26 |
| 12/18/07 | 1.51 |
| 01/24/08 | 0.53 |
| 03/11/08 | 1.64 |
| 04/28/08 | 1.15 |
| 06/26/08 | 0.32 |
| 08/07/08 | 0.30 |

Because of the previous argument the wingmill may seem like a superior system to the VIVACE, but when comparing Figure 10 with Figures 12 and 14 the wingmill system is considered a highly mechanically complex system in comparison to the VIVACE. This in itself may cause maintenance problems that are unsatisfactory.

# 2.0 DESIGN CONCEPTS AND FABRICATION PROCESS OF THE FLAPPING METHOD

Several different hydrokinetic device concepts were taken into consideration and one was chosen to become a physical prototype and to be tested. The concepts considered can be categorized into two major classes with the first being acknowledged as a *pressure build up/release* method and the second a *flapping* method. In all of the design concepts that will be described is an inherent cyclic nature. The reason for the cyclic nature is because when a force is applied to the piezoelectric material resulting in a mechanical stress a voltage is generated. The voltage increases with applied force but drops to zero when the force remains constant due to charge dissipation [30]. Conversely, when the stresses are removed a voltage is again generated, with a magnitude opposite to when the stress is applied, and decays to zero. One full cycle of applying and removing a stress to a piezoelectric material and the resulting generated voltage is shown in Figure 18. This is why piezoelectric materials must be used in a cyclic nature (or dynamic process) and not a static process. For maximum energy harvesting, the charge should be collected when the voltage reaches the peaks shown in Figure 18.

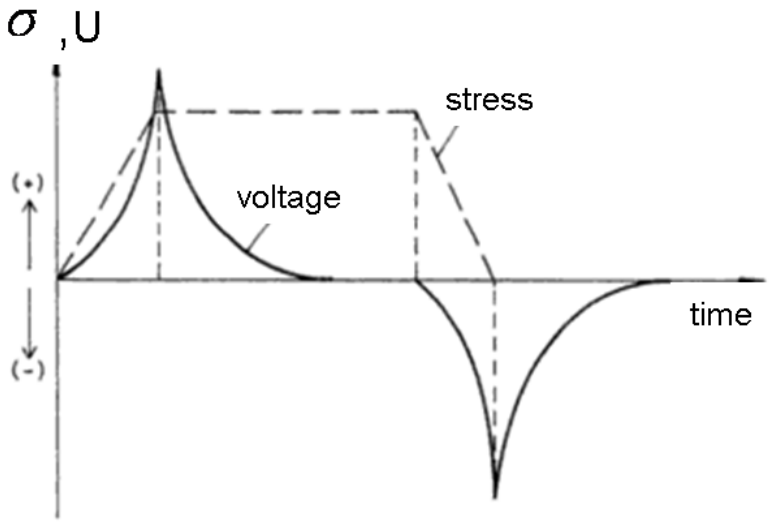


Figure 18: Typical output signal of piezoelectric materials

## 2.1 PRESSURE BUILD UP/RELEASE CONCEPT

A *pressure build up/release* method that was considered can be labeled as the 'saloon door' method. This device would resemble a saloon door, again made of an elastically deformable piezoelectric material, that is initially held closed by some type of latch as shown in Figure 19(a). When a certain pressure level is achieved the latch is released and the doors swing completely open, as shown in Figure 19(b), relieving the stresses in the piezoelectric material. Therefore, in the closed state the piezoelectric material would be under stress and in the open state it would be relaxed. The saloon door method was experimentally tested but a viable method which allowed the doors to go from the open to closed state could not be determined. Because of this the fabrication process of the saloon door is not discussed. The prototype used in experimentation is shown in Figure 20. The door is made of 110 μm thick PVDF and after coated with M-coat A polyurethane (reasons for the coating are discussed in the fabrication process of the flapping method) it has a total thickness of 381 μmṪhe dimensions of the door are approximately 20.5 mm by 18 mm.

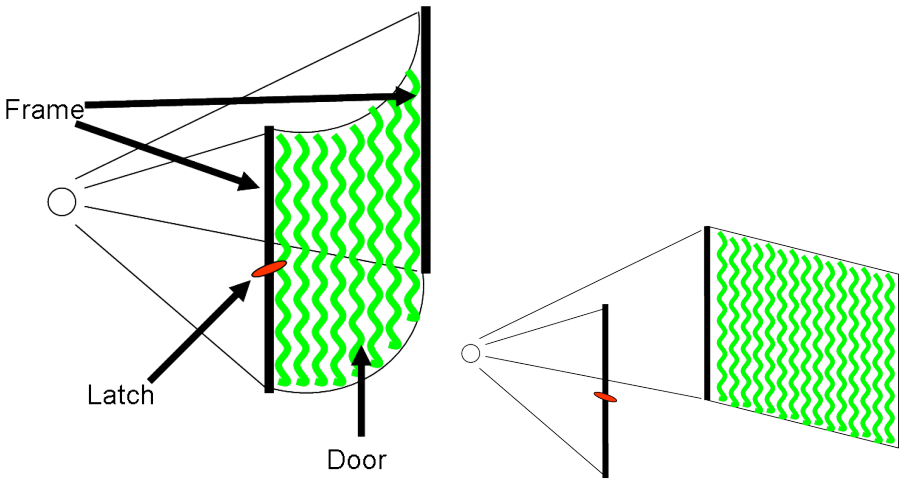


(a) Pressure build up (b) Pressure release

Figure 19: Schematic of the saloon door pressure build up/release concept a) Smart material stressed (pressure build up) b) Smart material relaxed (pressure release)

The functions of the labels in Figures 20(a) and 20(b) are explained as follows:

- Door - Part of the device that generates the voltage
- Frame - Part of the device where the strings are attached, the door moves relative to the frame
- String - The link between the flume walls and the frame to hold the device in place
- Latch - Made of duct tape in prototype and used to hold the door shut until the water pressure causes it to open
- Silicone - A thick coating was needed to protect the leads from becoming short circuited

Figure 21 is representative of the average open circuit voltage signal of the saloon door method from experimentation after ten trials. Only one full cycle can be seen because as already mentioned a viable method of relatching the door could not be determined. Therefore, power produced by the saloon door method can only be determined if a frequency is chosen for the cycle period and a load resistance is determined. This will be discussed in Chapter 3.

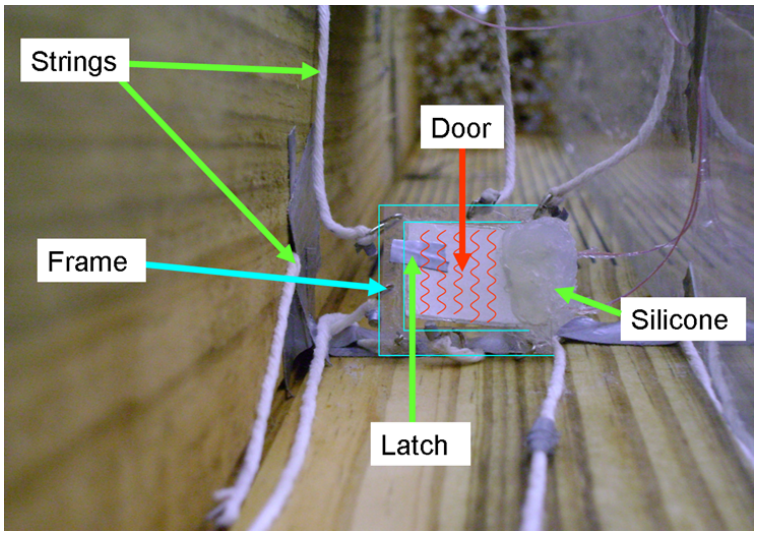


(a) Closed front view

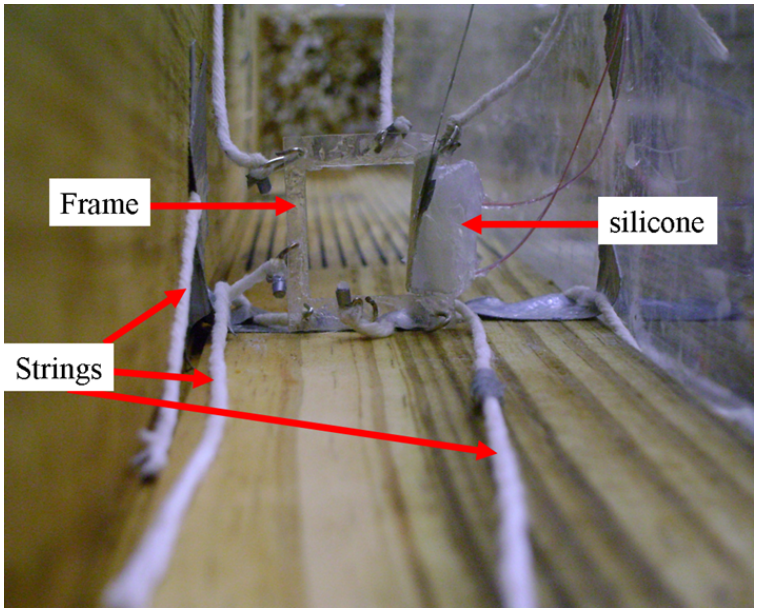


(b) Open front view

Figure 20: Saloon door prototype a) Top view b) Front view with the door closed and latch locked c) Front view with door open and latch released

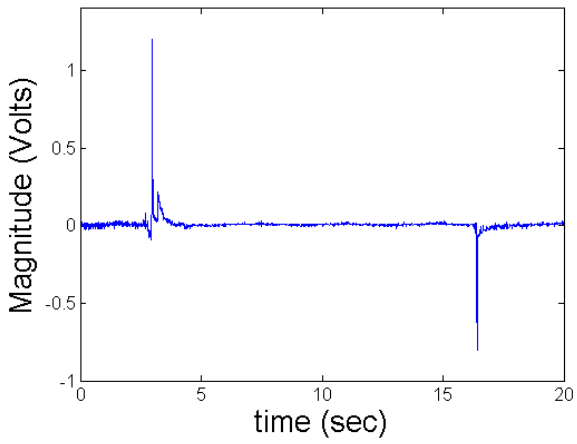


Figure 21: Experimental results of the saloon door method

The *flapping* and *pressure build up/release* methods each have their own advantages and disadvantages, but ultimately it was one of the *flapping* technique methods that was chosen to become the prototype because of its simplicity.

## 2.2 THE FLAPPING CONCEPT

The flapping technique can be described as a conical kite attached to the free end of a cantilevered beam, which oscillates it back and forth. A schematic of the flapping concept can be seen in Figure 22. Although it has not been proven, the oscillation is thought to arise from the beam itself disrupting the flow patterns into the cone, therefore the flow will continuously arrive at different angles with respect to the plane of the cone entrance. If all of the flow arrived perpendicular to the plane of the cone entrance, this would create the highest possible force on the beam. The restoring force is generated from the elastic energy in the beam itself. A theoretical model of this device was not explored because the power generated by it was approximately 77 µm, which with the size of its footprint is too low to

be feasible. The results will be further discussed in chapter 3, 'Experimental Results of the Flapping Method'.

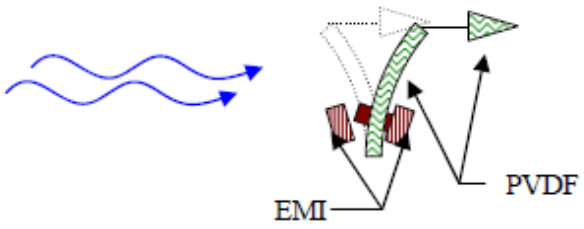


Figure 22: Schematic of the flapping concept

## 2.3 THE FABRICATION PROCESS OF THE FLAPPING DEVICE

The fabrication process has four main steps (assuming the induction solenoids have already been constructed):

1. Cut and etch the PVDF
2. Attach the leads to the PVDF
3. Create the cantilevered beam
4. Construct and attach the conical kite to the free end of the beam

In the subsequent sections a discussion of the fabrication process that was followed in this thesis to construct a flapping device is presented.

### 2.3.1 Fabrication Process Part 1 - Cut and Etch the PVDF

The first step of the fabrication process consisted of patterning the PVDF by simply cutting the desired shape from the fully metalized sheet of PVDF shown in Figure 23(a). The sheet of PVDF was recieved pre-electroded with a compliant silver ink from Measurement Specialties [3]. For the creation of the beam a rectangular shape was cut, Figure 23(b) shows this type of patterning. The sheet of PVDF shown in Figures 23(a) and 23(b) is a total of 40 μm thick. The PVDF itself is 28 μm thick with a 6 μm silver ink layer on each of its sides as shown in Figure 24 [41]. The silver ink metal is utilized as an electrode that allows conduction.

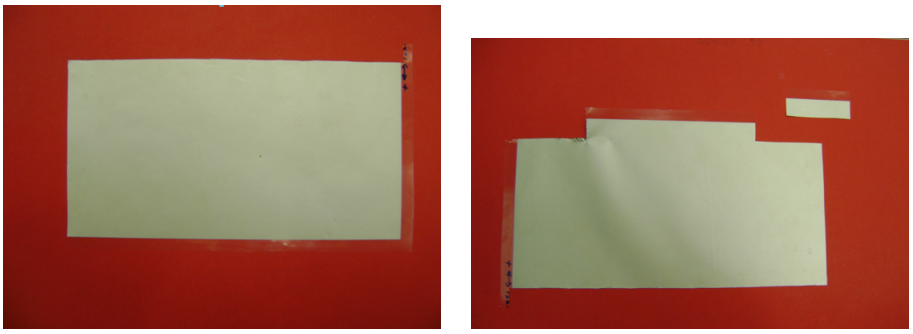

(a) Metalized sheet of PVDF (b) Patterned cut

Figure 23: Part of the first step of the fabrication process - patterning the PVDF a) Metalized sheet of PVDF b) Beam cut out of sheet

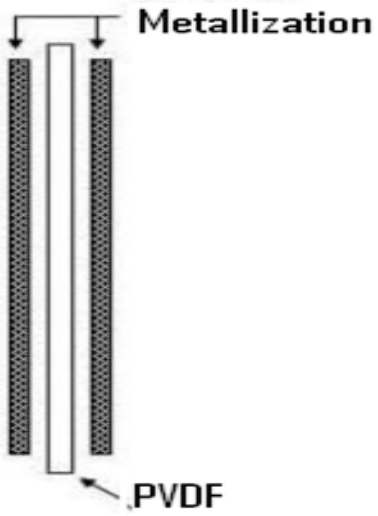


Figure 24: Schematic of a sheet of PVDF

After the PVDF was patterned, an extremely important step to be taken was to etch the PVDF sample to prevent the top and bottom electrodes from shorting each other out. If they are short circuited there will be zero voltage between the two electrodes thus no power can be produced. The goal in etching a sample is to remove the silver ink metal around the perimeter of the sample as shown in Figure 25. The depth of the etch in this sample is approximately 1 mm around the perimeter. For every sample prepared in this work, the etchant applied to remove an area of silver ink was acetone. A cotton swab (Q-tip) was utilized to apply the acetone to the desired region and a precision knife was used to scrape off the remaining silver ink.

### 2.3.2 Fabrication Process Part 2 - Attach the Leads

The 'leads' are the wires that are connected to the PVDF for conduction. The wire utilized for conduction is a 40 gauge copper wire, originally a thermocouple wire. The metallic substance bonding the wire to the electrode is a silver/silver conductive epoxy. A lead attached to an electrode is shown in Figures 26(a) and 26(b). It is important to note in Figure 26(b) that the conductive epoxy does not protrude out into the etched region of the PVDF. If it does protrude on both sides of the PVDF it is possible that the electrodes could

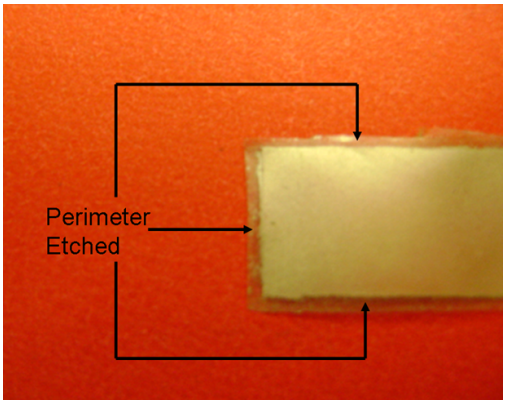


Figure 25: Etched piece of PVDF

be short circuited and thus no power could be generated. Proper connections were checked by a multimeter to ensure that the resistance from the free end of a wire to its connected electrode was approximately zero.

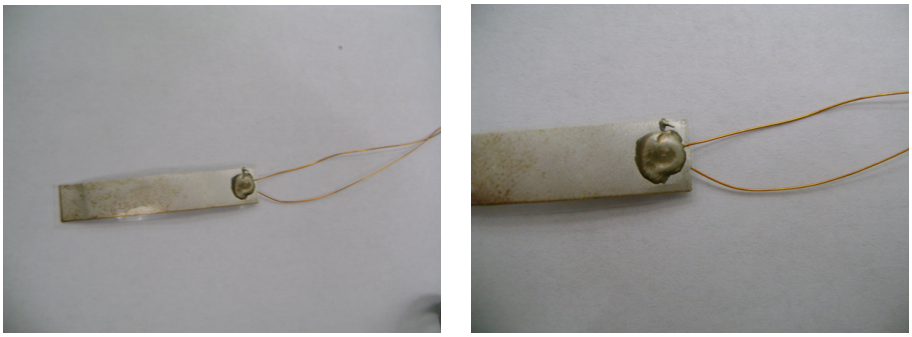

(a) Lead attached to electrode (b) Lead attached to electrode close up

Figure 26: Leads attached to PVDF a) Entire beam view b) Close up of lead

### 2.3.3 Fabrication Process Part 3 - Construct the Cantilever Beam

The substrate of the beam was made of shim stock plastic and it was cut to the same dimensions as the PVDF. A slot, shown in Figure 27(a), was cut in the substrate for the lead to sit in so that the rest of the PVDF sample can lay flush on the substrate for a better

bond. The bonding process was completed by applying M-coat A polyurethane as thin as possible onto one side of the substrate. The reason the M-coat A polyurethane was chosen is because it is the same bonding substance used to attach strain gauges to structures, thus most of the stress should be carried throughout the structure. The PVDF was then placed onto the substrate as shown in Figure 27

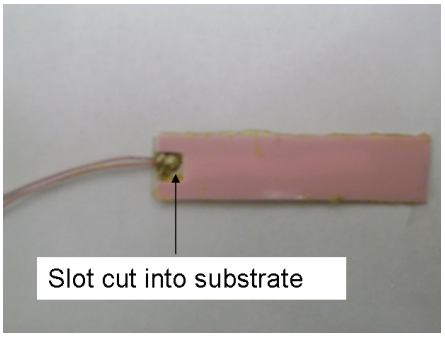


(a) Bottom view

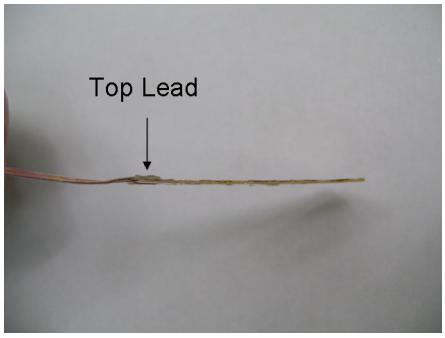


(b) Side view

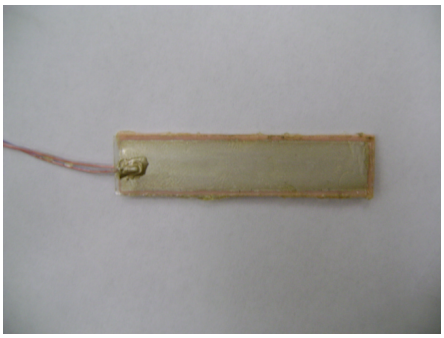

(c) Top view

Figure 27: PVDF bonded to plastic beam a) Bottom view showing slit in beam b) Side view c) Top view

After the PVDF was bonded to the substrate, a thin layer of M-coat A polyurethane was applied to the exposed side of the PVDF's electrode. This coating is critical in the fabrication process for two reasons 1) since the device is exposed to water, if the coating is not applied there is a possibility the device will short itself out because water can conduct electricity and 2) water is corrosive, therefore a coating helps protect the PVDF and the silver ink electrodes.

Once the bonding and coating were completed, the composite beam was fixed at the end where the leads are located to produce a cantilever beam. To construct the clamp for the composite beam two half inch pieces of acrylic were cut into the shapes shown in the schematic of Figure 28. The orientation of the beam relative to the flow direction is shown in Figure 29(d), and in reference to this orientation Figures 28(1A) and 28(1B) are right piece (the piece that is situated upstream) and Figures 28(2A) and 28(2B) represent the left piece (the piece which is downstream). Therefore, Figure 28(1A) shows the same exact view as Figure 29(a) of the upstream (right) piece. The volume removed for the beam allows it to sit flush in the right piece. The red surfaces are the two surfaces that are butted together with the beam placed in between. The substance used to bond the right and left pieces was 100 % silicone rubber sealant because of its insulating characteristics. The only function of the protruded piece of acrylic on the left side of the upstream (right) and downstream (left) pieces was used to hold the flapping device in the flume for experimentation. This clamp also serves another purpose that is not obvious. Shown in Figure 29(a) the acrylic clamp protects the end of the beam where the leads are attached. When a multimeter was attached to the free end of the leads and the resistance between the electrodes was measured, without the acrylic clamp when this portion of the beam was submerged into water the impedance between the electrodes would significantly decrease. With the acrylic clamp the impedance would remain constant. Therefore, the acrylic clamp adds resistance to this section of the beam preventing a short circuit between the electrodes. An observational hypothesis on why the electrodes short circuit when the portion of the beam where the leads are attached is submerged without the acylic clamp is because the silver/silver conductive epoxy used to bond the leads to the elctrodes is applied at a thickness of about 500 μm and the M-coat coating is only about 100 μm thick. Therefore, it is believed that because the M-coat coating layer's thickness is much less than the thckness of the epoxy it does not supply a high enough resistance.

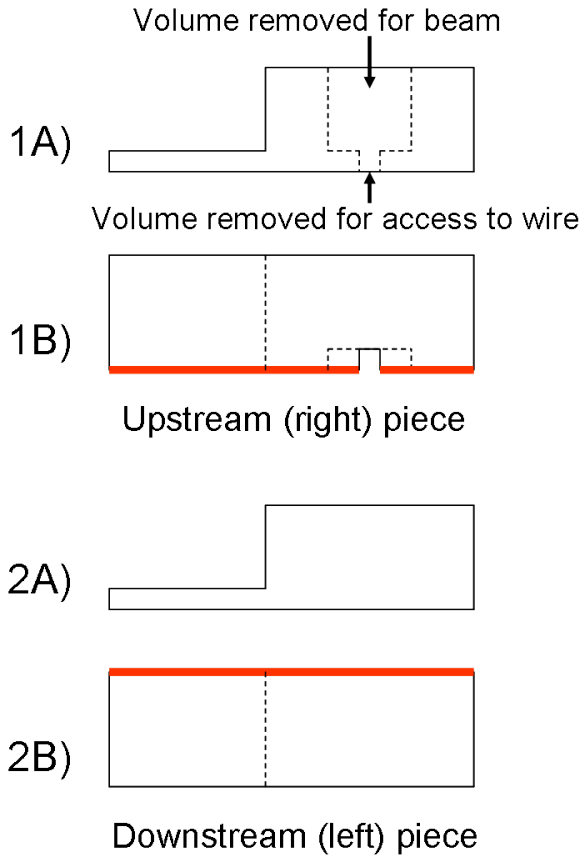


Figure 28: Schematic of the chosen shapes to fix one end of the beam

Figure 29 shows four different views of the fully assembled cantilever, composite beam. Figures 29(a) and 29(b) show photos of the clamp in the same orientation of Figure 28. The device is oriented in such a way that the side of the beam with the PVDF is upstream as shown in Figure 29(d), therefore placing the bare side of the beam downstream. This type of orientation will allow the PVDF to be stressed in tension.

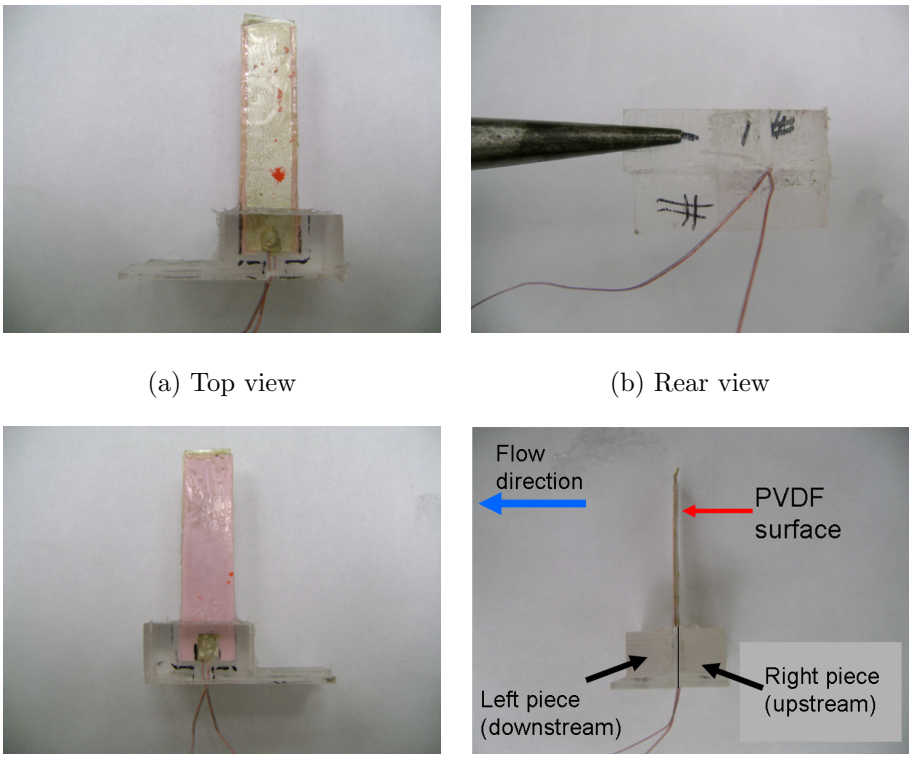


(a) Top view

(b) Rear view

(c) Bottom view

(d) Side view

Figure 29: The Flapping Method Cantilever Beam Device a) Top view b) Rear view c) Bottom view d) Side view

### 2.3.4 Fabrication Process Part 4 - Attach the Conical Kite

The conical kite was created with polyethylene terephthalate (a.k.a transperency film) and duct tape and was connected to the free end of the cantilever beam with 0.381 mm (0.015 in) diameter fishing line. The first step taken to construct the conical kite was to cut a quarter circle out of a piece of transparency paper as shown in Figure 30(a). The paper was then folded to form the cone shown in Figure 30(b) and the crease was sealed with duct tape. *Note:* The cone in Figure 30(b) is made with white paper for visual purposes only.

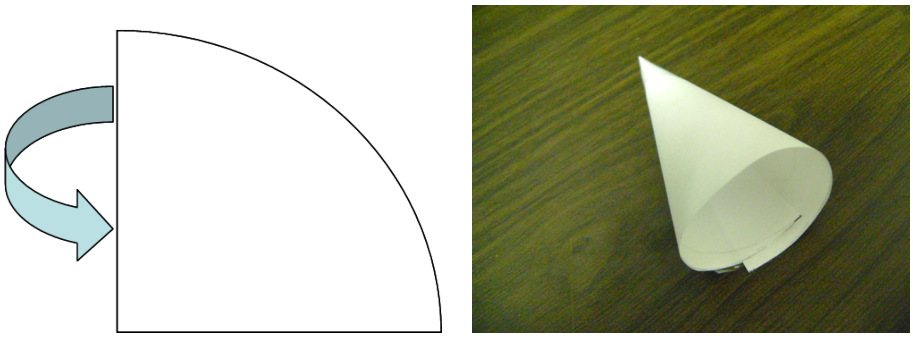

(a) quarter Circle (b) Cone

Figure 30: Cone construction a) Quarter circle shape b) Cone

The cone was connected to the free end of the beam with fishing line. Two small holes by the opening of the cone were created and the fishing line was pulled through the holes and knotted to keep it in place as shown in Figure 31(a). Figure 31(b) shows how the fishing line was attached to the beam with tape, thus creating a conical kite.

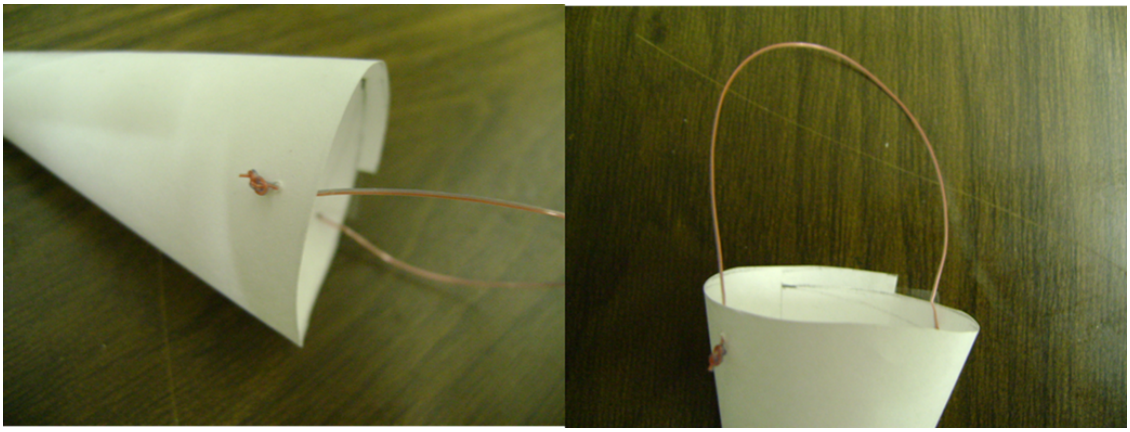

(a) quarter Circle

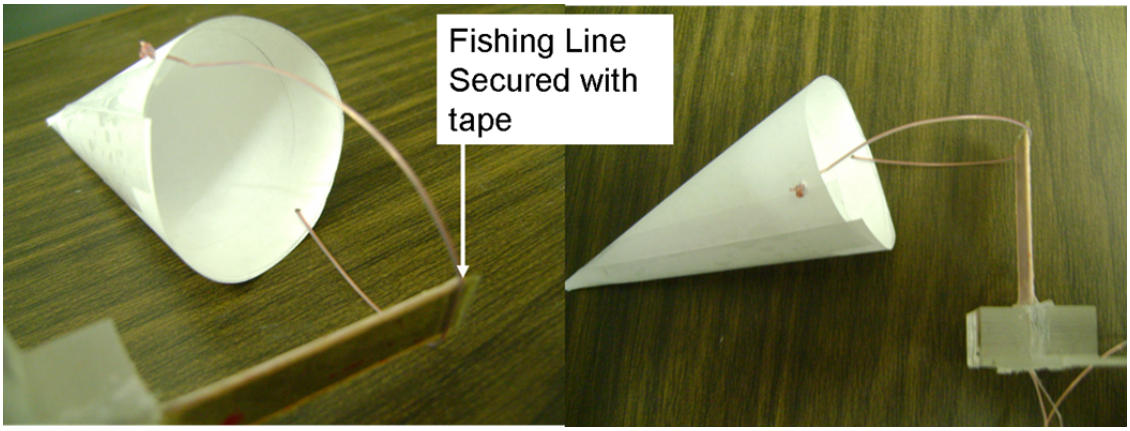


(b) Cone

Figure 31: Attaching the cone to the beam a) Fishing line in cone b) Connecting cone to beam

# 3.0 PRELIMINARY ANALYSIS OF THE PIEZOELECTRIC MATERIAL PVDF AND EXPERIMENTATION OF THE FLAPPING METHOD

Prior to experimentation, preliminary analysis on the possible power production of PVDF was examined. For analysis purposes the next section focuses on the behavior of piezoelectric materials.

## 3.1 SMART MATERIALS

As previously mentioned there is a subclass of smart materials that when stressed produces a voltage potential. This subclass of smart materials consists of ionic polymer transducers, piezoelectric materials, and electrostrictive materials. The piezoelectric material used in experimentation and analysis of this thesis is polyvinylidene fluoride (PVDF), but all piezoelectric materials have three main uses:

1. They can be utilized as sensors to measure pressure, acceleration, force, or strain.
2. They can be used as actuators by exploiting the reverse piezoelectric effect, which is the production of stress/strain when an electric field is applied.
3. They can be used as electrical energy generators, which is the focus in this thesis.

### 3.1.1 Common Generator Modes of Piezoelectric Materials

When a piezoelectric material is used as a generator there are two main generator modes of operation of the piezoelectric element that are shown in Figure 32. These two common

generator modes play a particularly important role when defining the electromechanical coupling coefficients $d_{ij}$ and $g_{ij}$. These coupling coefficients are referred to as the strain and voltage constants, respectively. The first subscript in the electromechanical coupling coefficients describes the poling direction (shown as P in Figure 32) and the second subscript shows the direction of applied force [31, 33]. The 3-axis is conventionally taken to be parallel to the direction of polarization of the material. Therefore, if the piezoelectric material is stressed in the 31-mode, shown in Figure 32b, this implies that the force is applied along the 1-axis and charge is collected on the surface that is perpendicular to the 3-axis. Also, when calculating the energy produced by a piezoelectric material stressed in a specific mode it is critical to use the correct coupling coefficient because, for example, in PVDF the $d_{33}$ coefficient is about 1.5 times as large as the $d_{31}$ coefficient [36]. Table 2 shows typical values for the material constants [3, 2].

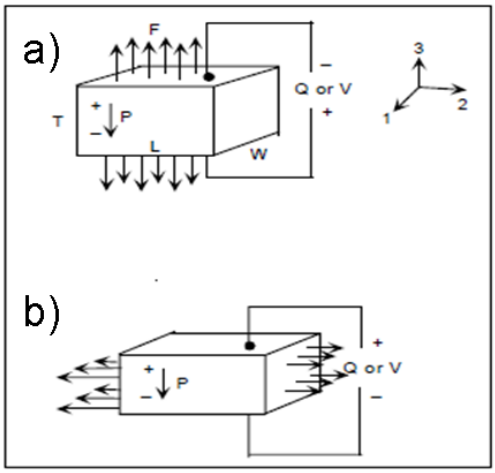


Figure 32: Schematic of force per charge relationship on a piezo generator element; a) element in 33 mode, b) element in 31 mode

It may be tempting to assume that since the $d_{33}$ coefficient is larger than the $d_{31}$ coefficient it is always better to harness energy by stressing the material in the 33-mode. But, according to Kim [36] the 33-mode of operation is difficult to realize in a real structure and in many cases it is easier to obtain higher stresses in the 31-mode because these stresses can include

Table 2: Typical constants for PVDF

| Constants | $d_{31}$ | $d_{33}$ | $g_{31}$ | $g_{33}$ | Young's Modulus, E |
|---|---|---|---|---|---|
| | $23 \times 10^{-12}$ | $33 \times 10^{-12}$ | $216 \times 10^{-3}$ | $330 \times 10^{-3}$ | $3 \times 10^{9}$ |
| Units | $\frac{C}{m^2}/\frac{N}{m^2}$ | $\frac{C}{m^2}/\frac{N}{m^2}$ | $\frac{v}{m}/\frac{N}{m^2}$ | $\frac{v}{m}/\frac{N}{m^2}$ | $N/m^2$ |

axial and bending stresses. This is important because it will be shown that the energy, and therefore power, is proportional to stress squared. In this thesis the 31-mode of operation is the only mode of energy generation used for the piezoelectric material in analysis and experimentation.

### 3.1.2 Energy and Power Production of a Piezoelectric Element

The electrical energy produced by a piezoelectric element for an applied force is

$$Energy = VQ \tag{3.1}$$

where $V$ is the voltage and $Q$ is the charge on the element [31, 3]. For a piezoelectric element in the 31-mode the charge and voltage can be expressed the following ways [31, 3]:

$$V = \frac{Fg_{31}}{W} \tag{3.2}$$

$$Q = \frac{Fd_{31}L}{T} \tag{3.3}$$

where $F$ is the applied force along the 1-axis and $L$, $T$, and $W$ are the length, thickness, and width of the given piezoelectric element, respectively. Assuming the applied force is repeatedly applied to the piezoelectric element for some period of time, an average power

produced by a piezoelectric element can be obtained by simply multiplying equation 3.1 by the frequency of the applied force, $f$, in units of Hertz to obtain equation 3.4.

$$P = VQf = \frac{Fg_{31}}{W} * \frac{Fd_{31}L}{T} * f * \frac{WT}{WT} \tag{3.4}$$

Equation 3.4 has been multiplied and divided by the width and thickness of the material to obtain Equation 3.5 so that power can be rewritten in terms of applied stress, element dimensions, material properties, and frequency of applied force. This equation is useful because it shows how each of these characteristics effect the power output.

$$P = \sigma^2 g_{31} d_{31} LWTf \tag{3.5}$$

## 3.2 PRELIMINARY ANALYSIS

The analysis that follows examines the theoretical power PVDF can create in order to ascertain the feasibility of the material for use in hydrokinetic harvesting. According to equation 3.5 the key to generating significant power is to cause high stress to be developed in a reasonable volume of PVDF at a high frequency without plastically deforming the PVDF. Initially, a significant amount of power will be defined as 1 kW and a realistic frequency will be normalized at 1 Hz. Since power is directly proportional to the frequency of applied force, one can multiply the preliminary results by the desired frequency to obtain the adjusted power. Since there are several ways to mechanically stress a structure the stress will be preserved as a variable where the allowable range of stresses needs to be determined. In the 31-mode of operation Vinogradov et al. [57] shows that the stress-strain curve of PVDF can have characteristics of either a brittle or ductile material depending on the orientation of its aligned molecular chains relative to the direction of the stresses with in the material. When PVDF is stressed in the 31-mode in the direction of the molecular chains, which will be referred to as direction 1, it acts as a brittle material and has a yield stress, $\sigma_{Y1}$, of 45 MPa. Vinogradov et al. have shown that PVDF shows no signs of plastic deformation as long as the stresses in the material stay below $0.57(\sigma_{Y1})$ or about 26 MPa. When PVDF

is stressed in the 31-mode normal to the orientation of the aligned molecular chains, which will be referred to as direction 2, PVDF acts as a ductile material and has a yield stress, $\sigma_{Y2}$, of 39 MPa. In this direction if the PVDF is constrained to $0.76(\sigma_{Y2})$ or about 30 MPa then it will not show any signs of plastic deformation. Therefore, in this preliminary study it will be assumed that PVDF is stressed in the 31-mode in direction 2 which will allow the stress to be varied from 0 to 30 MPa. This will also be referred to PVDF's maximum stress. Knowing the range of permissible stress allows the use of equation 3.5 to be rewritten as equation 3.6 to determine the amount of volume of PVDF that is needed to produce 1 kW of power.

$$Volume = \frac{P}{\sigma^2 g_{31} d_{31} f} \tag{3.6}$$

Figure 33 shows the volume of PVDF needed to produce kW of power as a function of applied stress at frequencies of 1 Hz, 2 Hz, 5 Hz, and 10 Hz. Nothing above 10 Hz has been considered because the medium is water which is a high density fluid and oscillating a structure above 10 Hz in a high density fluid is difficult.

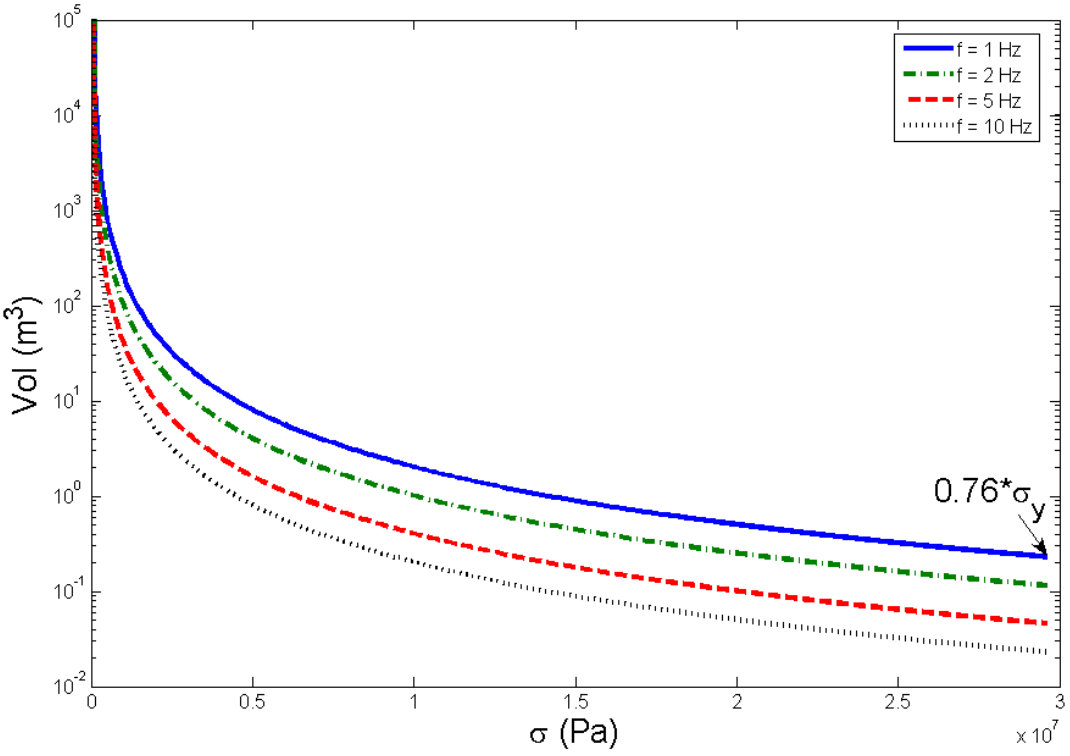


Figure 33: Required volume of PVDF to produce 1 kW of power as a function of stress where the frequency is held constant at 1 Hz, 2 Hz, 5 Hz, and 10 Hz

Figure 33 shows that if PVDF is stressed to its maximum allowable stress, located at the far right of the plot, at 1 Hz then 0.23 $m^3$ of material is needed to produce 1 kW. This volume is accepted as a reasonable amount because a Gorlov helical turbine can produce up to 200 kW at a free stream velocity of about 6.1 m/s with a volume of 9.5 $m^3$ [26] and is comparable to PVDF. The turbine's power is based on velocity and the PVDF's is based on frequency, and based off of the experimental results (shown later) a frequency of 1 Hz is definitely obtainable at 6.1 m/s. Table 3 summarizes the volume of PVDF required to produce 1 kW of power when stressed at its maximum as the frequency increases.

To link the following analysis with hydrokinetics one could imagine a riverbed lined with a grid of undulating strips made of PVDF that resemble a natural environment. The fluid flow could be used to induce stresses in the PVDF and hence, power is generated. Since

Table 3: Volume of PVDF needed to produce 1 kW when stressed at its maximum at the given frequencies

| Frequency [Hz] | Volume [$m^3$] |
|---|---|
| 1 | 0.23 |
| 2 | 0.12 |
| 5 | 0.046 |
| 10 | 0.023 |

this generated power is linearly related to the volume of material, if one 0.23 $m^3$ element of PVDF stressed to its maximum at 1 Hz creates 1 kW then two 0.23 $m^3$ elements of PVDF stressed to their maximum at 1 Hz would create 2 kW. Therefore, if 1 $m^3$ of PVDF was stressed to its maximum at 1 Hz the theoretical power output would be approximately 4.3 kW. To physically represent 1 $m^3$ of PVDF, the material will be divided into more than several strands that resemble synthetic turf. For comparison, consider artificial turf or "Astroturf". The Astroturf company [13] produces 0.0508 X 0.0001 X 0.001 $m^3$ sized strands of synthetic turf and they claim that there are on average about 360,000 strands of Astroturf in 1 $m^2$ of surface area. This size and number of strands in 1 $m^2$ of surface area corresponds to a volume of approximately 0.0018 $m^3$ of material. Therefore, it takes approximately 555.6 $m^2$ of surface area to fit 1 $m^3$ of Astroturf material. For comparison purposes, one American football field contains 4,456 $m^2$ of surface area, which corresponds to a volume of approximately 8 $m^3$ or 1.6 billion strands of Astroturf material. Figure 34 shows the amount of power that can be generated by increasing the surface area from 0 $m^2$ up to approximately one American football (that is from 0 to 1.6 billion strands) if the strands of synthetic turf were made of the piezoelectric material PVDF and operated in the 31 generator mode in direction 2 at different peak stresses up to the maximum allowable stress at 1 Hz.

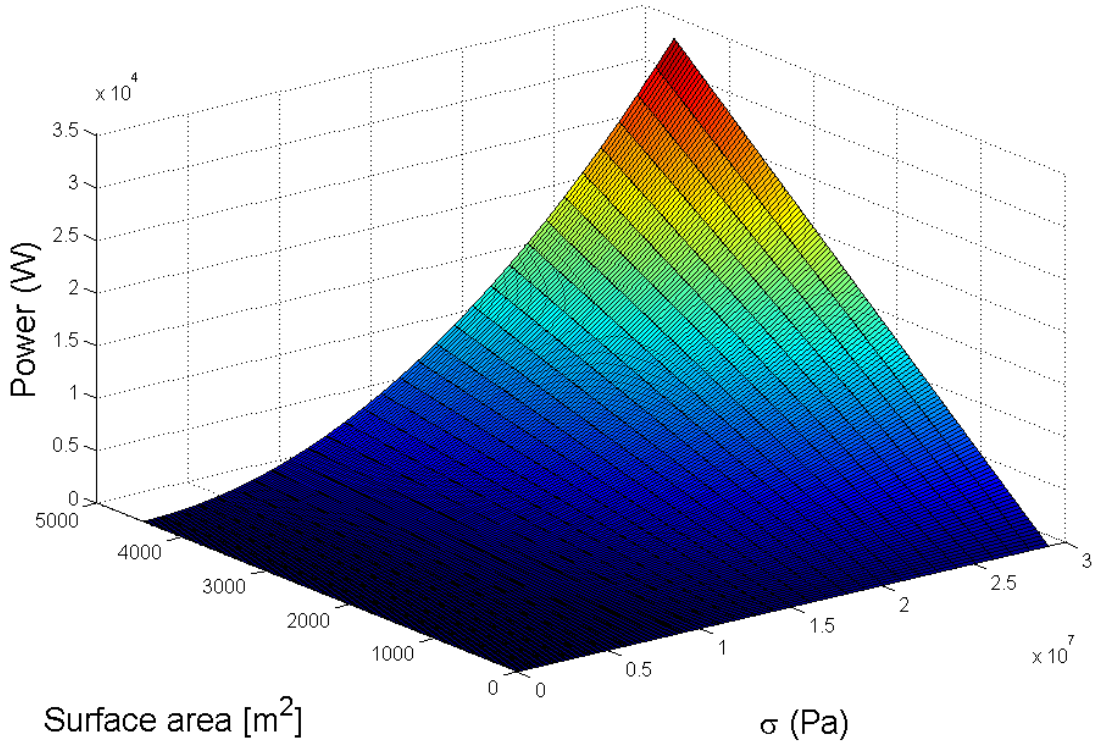


Figure 34: Stress and Volume VS Power produced by PVDF at 1 Hz in a given surface area up to 4,450 $m^2$

According to Figure 34 if the Astroturf sized pieces of PVDF can be stressed to $0.76(\sigma_{Y2})$ at 1 Hz, then covering around 4,450 $m^2$ (or about 1 American football field) of a riverbed theoretically produces approximately 34 kW. Although this result is promising, it is a theoretical upper limit to the power PVDF could reasonably produce and there are three major drawbacks to this method of analysis. The first is it has been assumed that all of the material is stressed to $0.76(\sigma_{Y2})$, which is the maximum allowable stress in PVDF without plastic deformation. A means to repeatably reach this stress every cycle without exceeding it is a concern. The second drawback is that *all* of the material must be stressed to this value. There is a certain difficulty in this because stressing all of the material cancels the use of bending stresses which introduce a stress distribution throughout the thickness of the material. Because of this stress distribution only the material furthest from the neutral axis

can be stressed to $0.76(\sigma_{Y2})$. It is also important to note that the PVDF has electrodes made of silver, which has a Young's Modulus that is about 27 times greater than PVDF. As a consequence, the electrodes will bear some of the induced stress and higher forces would be required to reach the maximum allowable stress in the PVDF. Also, there was no consideration for a coating layer which is necessary if the PVDF is to be utilized under water. The effect on the power output due to considering the electrodes and coating layer will be addressed later through experimentation. The third drawback is it has been assumed that there is a 100 % efficiency in the mechanical to electrical energy conversion and in reality there will be a load resistance which will not allow this efficiency. In light of these drawbacks there is an upside to this result which is the normalization of the frequency at 1 Hz. It may be possible to apply the stresses at a higher frequency thus increasing the maximum theoretical limit. For example, stressing the PVDF to $0.76(\sigma_{Y2})$ at 2 Hz, one American football field would theoretically produce approximately 68 kW, at 3 Hz 102 kW, etc.

Applying a stress on a strand of PVDF in a riverbed as in the previous theoretical analysis proves to be problematic. To illustrate this, a theoretical analysis in which the strand of PVDF is stressed in a more realistic manner in a river environment, such as the flapping device revealed in Chapter 2, is called upon. The flapping device is a cantilever, bimorph beam and, therefore, will not allow all of the PVDF material to be stressed to the maximum allowable stress without plastic deformation. This is due to a stress distribution through the thickness of the material. In order to refine the previous analysis to account for the stress gradient results by Smith [52], who utilized energy methods to determine the stresses in a bimorph cantilever beam, were built upon by Kim [36] to determine the energy a bimorph cantilever beam can produce if a piezoelectric element is taken into consideration. Kim's result for the electrical energy produced by a bimorph, cantilever due to an end load is

$$U_{gen} = \frac{9d_{31}^2 s_{11}^{E^2} s_m^2 h_p h_m^2 (h_m + h_p)^2 L^3}{\epsilon_{33}^T W B_{11}^2 \left\{1 + \left(\frac{3s_{11}^{E^2} s_m h_p h_m^2 (h_m+h_p)^2}{S_h B_{11}} - 1\right) K_{31}^2\right\}} F_o^2 \tag{3.7}$$

The variables $B_{11}$, $K_{31}$, and $S_h$ can be expressed as

$$B_{11} = s_m^2 h_p^4 + 4 s_{11}^E s_m h_m h_p^3 + 6 s_m s_{11}^E h_p^2 h_m^2 + 4 s_{11}^E s_m h_p h_m^3 + s_{11}^{E^2} h_m^4 \tag{3.8}$$

$$K_{31} = \frac{d_{31}}{\sqrt{\epsilon_{33}^T s_{11}^E}} \tag{3.9}$$

$$S_h = s_{11}^E h_m + s_m h_p \tag{3.10}$$

The other variables are defined as follows:

- $s_{11}^E$ is the elastic compliance of PVDF at constant electric field [$m^2$/N]
- $s_m$ is the elastic compliance of the substrate [$m^2$/N]
- $h_p$ is the thickness of the PVDF [m]
- $h_m$ is the thickness of the substrate [m]
- $\epsilon_{33}^T$ is the permittivity constant of PVDF [F/m]
- $d_{31}$ is the strain constant of PVDF in the 31-mode of operation
- W is the width of the beam [m]
- $F_o$ is the applied force [N]

The configuration of the beam is shown in Figure 35 and it is well known that the maximum longitudinal stress in a cantilever beam is given by

$$\sigma_{max} = \frac{Mc}{I} \tag{3.11}$$

if the variable $c$ is the furthest distance from the neutral axis to the location of maximum stress.

If the force is applied at the free end of the beam the moment, $M$, can be expressed as the length of the beam multiplied by the magnitude of the force. Also, $I$ is the second moment of inertia in units of $m^4$. For given beam dimensions the maximum allowable input force on the beam, without plastically deforming the PVDF, can be determined by

$$F_{max} = \frac{I \sigma_{max}}{Lc} \tag{3.12}$$

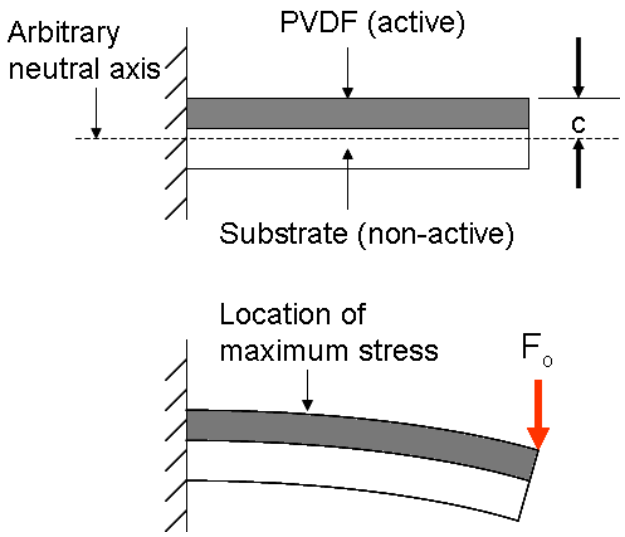


Figure 35: Configuration of bimorph beam showing the distance $c$ and location of maximum stress according to $c$

Assuming the maximum force can be applied to the beams, equation 3.7 will be utilized to account for the stress gradients in the PVDF in calculating the power that can be generated (as opposed to the previous analysis, using equation 3.5, that assumed maximum stress throughout the material).

Now that the maximum allowable input force on the beam is known equation 3.7 can be utilized to equate the power per area (of riverbed) generated with bimorph, cantilever beams by multiplying it by the frequency of the applied force. The frequency will again be normalized to 1 Hz. It will be assumed that 1 $m^2$ contains 360,000 beams to be consistent with the previous analysis. The substrate of the beam is chosen to be plastic shim with an elastic modulus, $E_m$, of approximately 3 GPa, which is equivalent to the elastic modulus of PVDF. The size of the beam is chosen to have the following dimensions so that the PVDF has the same dimensions as the previous analysis:

- L = 50.8 mm (length of PVDF and substrate are equivalent)
- W = 1 mm (width of PVDF and substrate are equivalent)
- $h_p$ = 0.1 mm

- $h_m = 1$ mm

Notice that a bonding layer and the electrodes of the PVDF have not been taken into consideration. From these dimensions it can be determined that 1 $m^2$ contains approximately 0.0018 $m^3$ of smart material, which corresponds to approximately 8 $m^3$ in about 4,450 $m^2$ of surface area. This is equivalent to the surface area and volume of material as in the previous analysis. Figure 36 shows the power generated within 4,450 $m^2$ of surface area (or approximately one American football field) full of cantilever, bimorph beams as the applied force is increased from zero to the force that stresses the PVDF to $0.76(\sigma_{Y2})$ at 1 Hz.

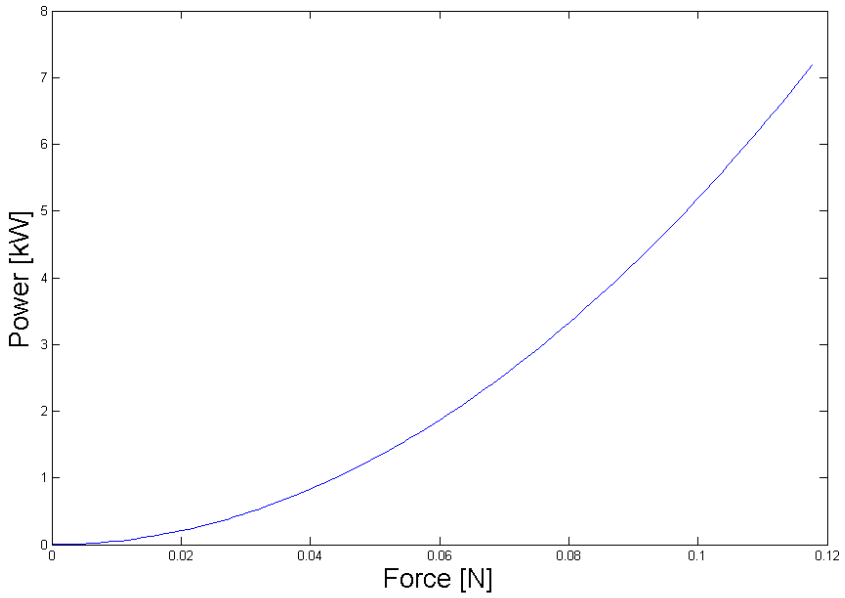


Figure 36: Generated power within 4,450 $m^2$ of surface area full of bimorph beams each with a layer of PVDF with dimensions of 0.0508 X 0.001 X 0.0001 $m^3$

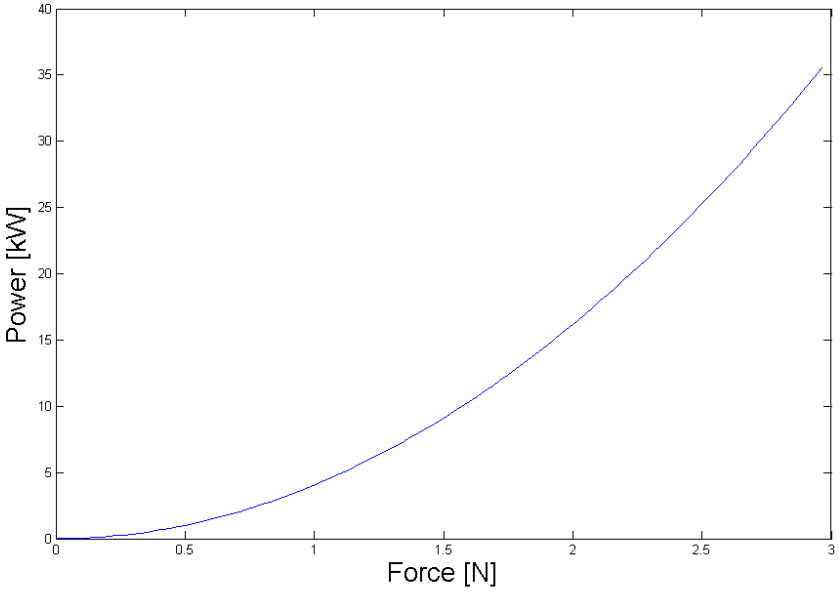


Figure 37: Generated power within 4,450 $m^2$ of surface area full of strands of PVDF with dimensions of 0.0508 X 0.001 X 0.0001 $m^3$ stressed to the maximum stress with no stress gradient

According to Figure 36 if the bimorph beams are stressed such that the maximum allowable input force puts a longitudinal stress of $0.76(\sigma_{Y2})$ on the PVDF material that is furthest away from the neutral axis at 1 Hz, then one American football field could theoretically produce an upper limit of 7.2 kW of power. This is approximately 21% of the power output of the Astroturf pieces of PVDF that assumed all of the PVDF stressed to the maximum allowable stress as shown in Figure 37. The difference here is that more force is needed to stress the material to the maximum stress. The major drawback in the cantilever method of analysis is there was no consideration for a bonding layer, the electrodes, and a coating layer, which are necessary. The next section will demonstrate a means to determine the effects of the electrodes and coating layer.

## 3.3 EFFECTS ON THE THEORETICAL RESULTS WHEN CONSIDERING THE M-COAT A POLYURETHANE COATING AND THE ELECTRODE LAYERS

To experimentally determine the effect of the electrode layers, which are necessary for conduction, and the M-coat A polyurethane coating layers, which are necessary for maintaining high impedance between the two electrodes while in use under water, on the theoretical results; a repeatable method to supply a known load is crucial. This will be done by comparing the generated power of a theoretical result with experimental results of a coated and non-coated piece of PVDF. Because the effects of the electrode and coating layers must be determined experimentally, the voltage produced by the PVDF will be measured and it will be shown that this voltage can be related to the energy generated by the PVDF. Therefore, to be able to compare a sample of PVDF without coating layers to one with coating layers the same load must be applied to both samples. Also, the applied load must be known so that the experimental results can be compared to the theoretical result. This will be done by applying a known uniform transverse pressure to a piece of PVDF oriented as a thin plate with clamped boundary conditions as shown in Figure 38, which according to Clark and Ramsey [20] when this is the case the stress in equation 3.5 can be expressed as

$$\sigma = \frac{E}{1-\nu} 0.309 \left( \sqrt[3]{\frac{p_o L}{2ET}} \right)^2 \tag{3.13}$$

E is the Young's Modulus of the plate, $\nu$ is the Poisson ratio, $p_o$ is the applied uniform pressure, L is the length of the square plate, and T is the thickness of the plate. This relationship between stress and pressure is the theoretical result that the experimental results will be compared to.

To simulate the loading in Figure 38, two similar square plate PVDF transducers were constructed, one with M-coat A polyurethane applied and the other with the electrodes ex-

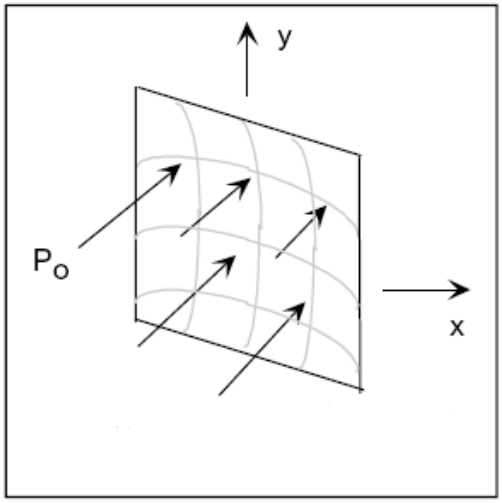


Figure 38: Schematic of thin plate under uniform pressure

posed to the environment. The transducers were attached to a square cross-sectional PVC pipe with silicone sealant. The coated transducer is shown in Figure 39(a). Each pipe was then attached to the platform shown in Figure 39(d), covering the pressure transducer and rubber hose inlet, shown in Figure 39(c), with silicone sealant for an air tight fit. Figure 39(b) shows the opposite side of the platform shown in Figure 39(c) and displays the rubber hose and the attachments to the pressure transducer. The square plate, PVDF transducer and platform were assembled so that the pressure rig shown in Figure 40 could be utilized because of its ability to supply a precise and repeatable pressure.

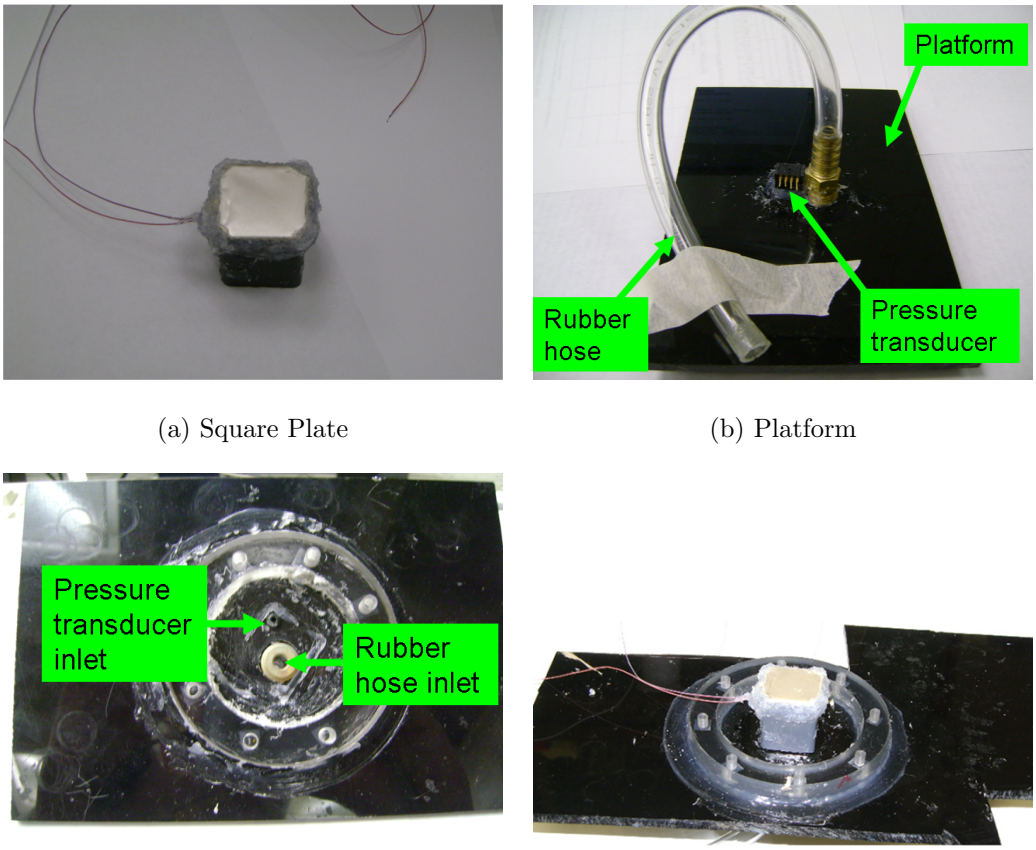


(a) Square Plate

(b) Platform

(c) Inlets

(d) Seal

Figure 39: Pressure test device

The apparatus shown if Figure 40 operates by allowing pressurized air at a known value through the precision pressure regulator. When solenoid valve 1 is opened (both solenoid valves are controlled manually through the toggle switches) the system becomes pressurized by the air flowing through the passage and continuing through the rubber hose. The square plate, PVDF transducer becomes stressed and produces a voltage across the electrodes. To depressurize the system and relieve the stresses in the PVDF, solenoid valve 2 is opened and exhausts the air.

Two different experiments were conducted. The first was with the coated PVDF transducer, which will be called the *coated trials* and the other was with no coating on the PVDF transducer, which will be referred to as the *non-coated trials*. The thickness of the PVDF film for each of the transducers is 28 µm with both having two 6 µm thick electrodes.

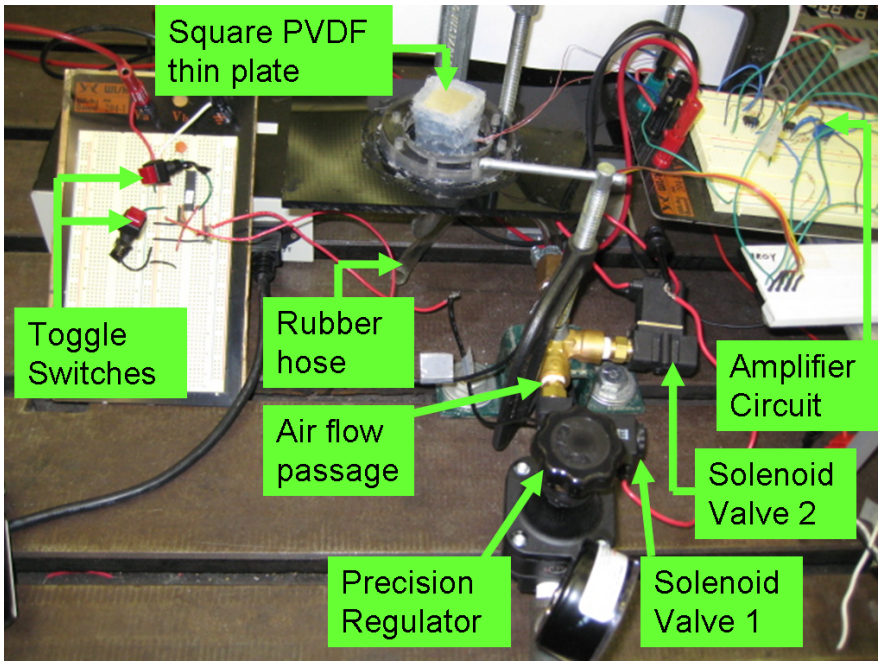


Figure 40: Pressure Rig

The coated transducer has an M-coat A polyurethane layer applied to both electrodes at a thickness of approximately 100 µm, which according to Measurements Group, Inc. is the thinnest possible thickness that can be applied to a substrate when the M-coat is applied with a brush. Both transducers have a 1 X 1 $in^2$ area. For the system described in Figure 40 two measurements are simultaneously taken, one from the PVDF and the other from the pressure transducer. The output voltage from the PVDF is measured directly and the output voltage from the pressure transducer is amplified so that after amplification a 1.5 V increase corresponds to 2.758 kPa. Figure 41 shows the response for one of the *coated trials* and for one of the *non-coated trials*. A -0.5 V offset was applied to the plot of the pressure transducer for the coated trials and a -5 V offset for the non-coated trials to set the two lines apart. This offset for the coated and non-coated trials can be seen in Figures 41(a) and 41(b), respectively. Therefore, when the output voltage of the pressure transducer reaches 1.0 V for the coated trials and -3.5 V for the non-coated trials a pressure of 2.758 kPa has been achieved.

For the coated transducer ten trials were recorded and the average maximum output voltage (positive spike) was found to be 1.34 V with a standard deviation of 0.13 V, and the average minimum output voltage (negative spike) was found to be -2.12 V with a standard deviation of 0.06 V. For the non-coated transducer ten trials were recorded and the average maximum output voltage was found to be 15.7 V with a standard deviation of 1.03 V, and the average minimum output voltage was found to be -20.1 V with a standard deviation of 0.32 V. The difference in the magnitudes of the positive and negative spikes is because it takes more time for the pressure to increase from 0 to 2.758 kPa than it does for the pressure to decrease from 2.758 to 0 kPa. When the pressure takes more time to increase to its maximum value so do the stresses in the PVDF and since the electrical time constant of PVDF is so small charge is dissipating very rapidly. Thus, this does not allow the output voltage to reach as high a magnitude as when the pressure does not take as much time to build to its maximum value. Also another reason for the difference in the magnitudes is because when the pressure builds up the response of the PVDF resembles a second order response causing the plate to act as a spring and absorbing some of the energy. This response is present in both the coated and non-coated trials but is exaggerated in the coated trial shown in Figure 41(a). It is odd that the spring-like behavior is seen only on the load half-cycle but not when pressure is released. This may be a consequence of the silicone sealant and PVDF interacting together because the sealant bonds non-electroded PVDF to the square pipe, there is no other material. When the pressure is quickly applied it acts as a step input and the silicone is stretched followed by a transient response and when this response dies out the steady state position of the stretched silicone remains. This steady state position may be so small that when the pressure is released the transient response of the spring-like silicone dissipates so abruptly that it can not be seen. It has not been proven that this is what is causing this spring-like action, but it is the authors hypothesis.

Equation 3.1 can be written as equation 3.14 utilizing equations 3.2 and 3.3 so that the electrical energy produced by a piezoelectric element can be written in terms of the voltage it produces.

$$Energy = \frac{V^2 W d_{31} L}{T g_{31}} \tag{3.14}$$

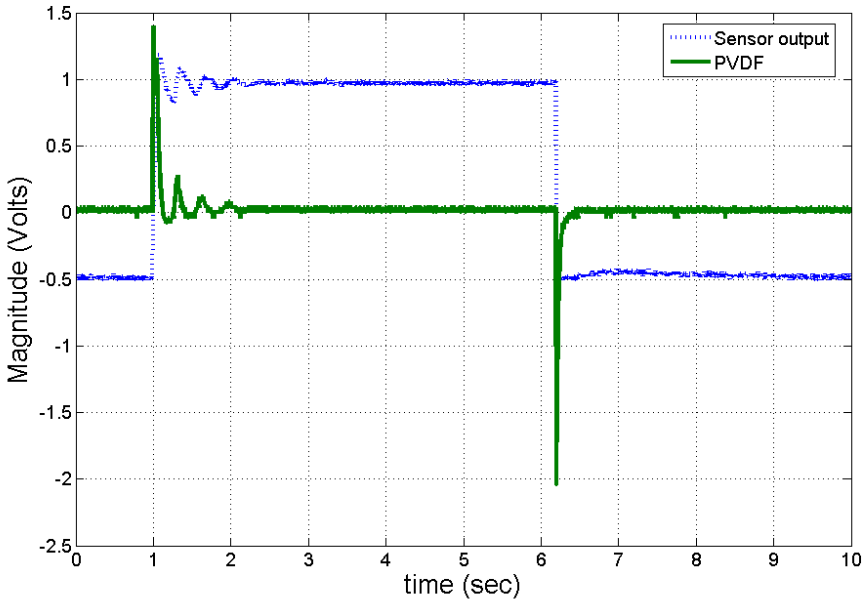


(a) coated

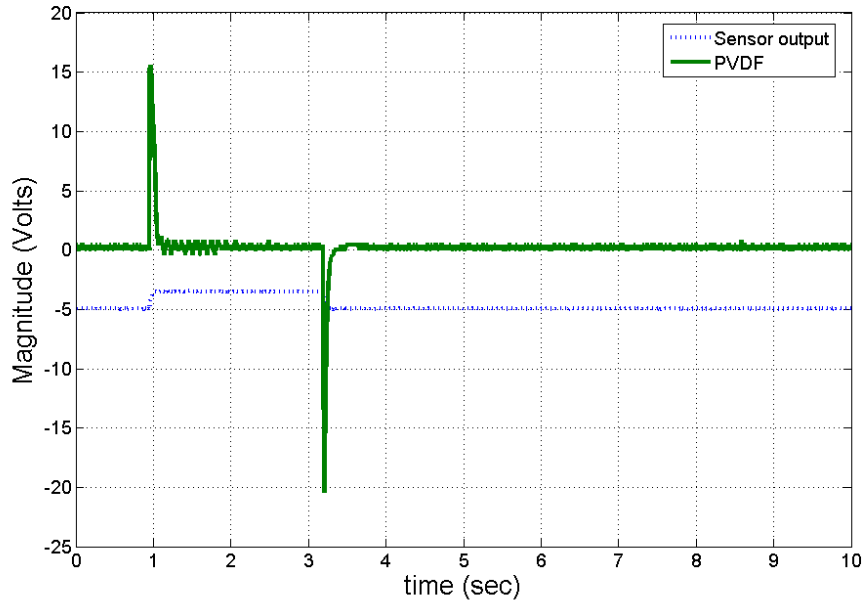


(b) non-coated

Figure 41: Voltage output of the square, PVDF transducer A) with coating B) no coating

Consequently, the maximum power produced is simply equation 3.14 multiplied by the frequency at which energy is harvested or the frequency at which a voltage spike occurs. Therefore, the average power produced by the coated, square, PVDF transducer at the positive voltage spike is 4.4 $(f)$ nW and at the negative voltage spike 11.0 $(f)$ nW, where $f$ is the frequency at which the spikes occur. The average power produced by the non-coated trials at the positive voltage spike is 604.8 $(f)$ nW and at the negative spike it is 991.2 $(f)$ nW.

Utilizing equation 3.13 to represent the stress in equation 3.5, Figure 42 shows the theoretical electrical energy produced by a square plate PVDF transducer with the previously given dimensions as a function of the transverse uniform pressure applied. The frequency of applied pressure has been preserved as a variable, therefore multiplying the results by a desired frequency will provide the adjusted power output.

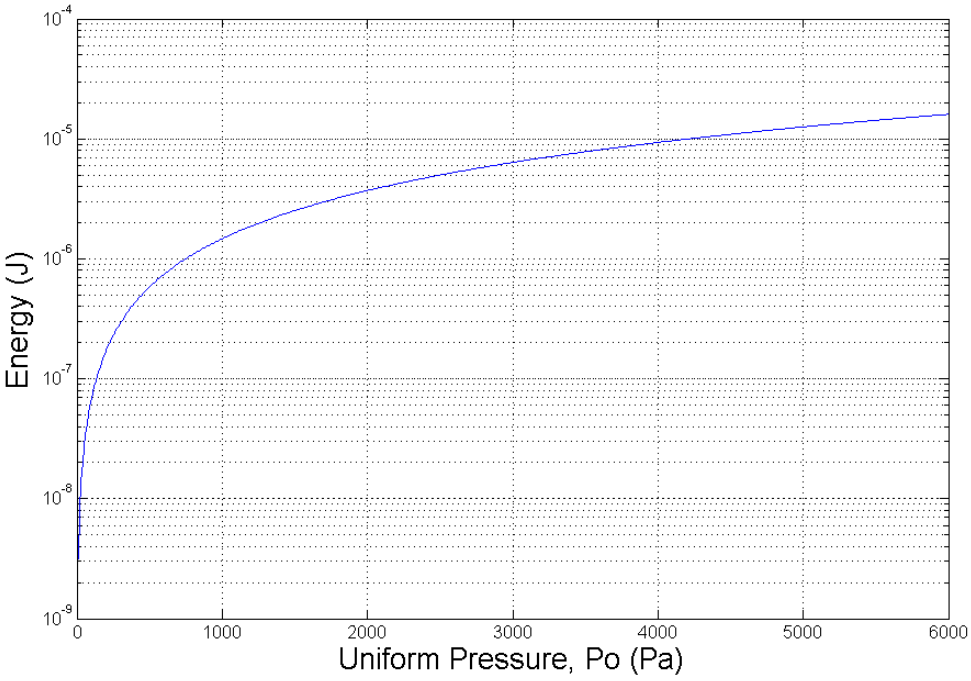


Figure 42: Electrical energy produced as a function of transverse uniform pressure

According to Figure 42 a pressure of 2.758 kPa corresponds to a theoretical power output of 5.7 $(f)$ µW. According to this result the coated transducer is producing approximately 0.1%

of the theoretical power when the pressure is applied and around 0.2% when the pressure is relieved. The non-coated transducer is producing about 10.6% of the theoretical power when the pressure is applied and approximately 17.4% when the pressure is released. Therefore, the electrodes and M-coat A polyurethane coating have a significant adverse effect on the power production of PVDF.

## 3.4 EXPERIMENTATION

Experimentation of the flapping device was performed in the Mechanics of Active Materials Laboratory at the University of Pittsburgh. The flow velocity in the flume utilized for experimentation was calculated to be approximately 1.6 m/s based on the cross-sectional area of fluid flow, which was measured to be approximately 2113 $mm^2$ (55.9 mm X 37.8 mm), and the 8-CIM model sump pump from Little Giant Pump Company that can pump fluid at about 54 gallons per minute. An experiment to verify the fluid flow calculation was performed by placing a small piece of foam in the flow and measuring the time it took for the foam to travel a known distance. The average flow velocity from this experiment was calculated to be approximately 1.5 m/s. It is believed that the discrepancy in these two numbers arises from the build up of residue in the pump. The composite, cantilever beam used for experimentation has a free length of 39.2 mm, a width of 8.76 mm and a thickness of 0.76 mm. This thickness includes the M-coat A polyurethane coating, the electroded PVDF, the M-coat A polyurethane bonding the PVDF to the beam, and the substrate made of 0.381 mm plastic shim.

As shown in Figure 44, this composite beam system is only part of the entire energy generating system. The entire system is a hybrid system coupling the energy generated by the PVDF with the energy generated by the electromagnetic system. The electromagnetic system's spool (the object that the conducting wire is wrapped around) has a 12 mm inner diameter, 30 mm outside diameter, and width of 8 mm where the wire is wrapped. There are approximately 500 turns of wire wrapped around the spool. The wire utilized in the electromagnetic system is a 32 AWG (American Wire Gauge) copper wire. The magnets

utilized are neodymium disc magnets with a diameter of 10 mm and a thickness of 3 mm and are rated as N50 strength according to supermagnetman.net [6]. The experimental configuration is shown in Figures 43 and 44.

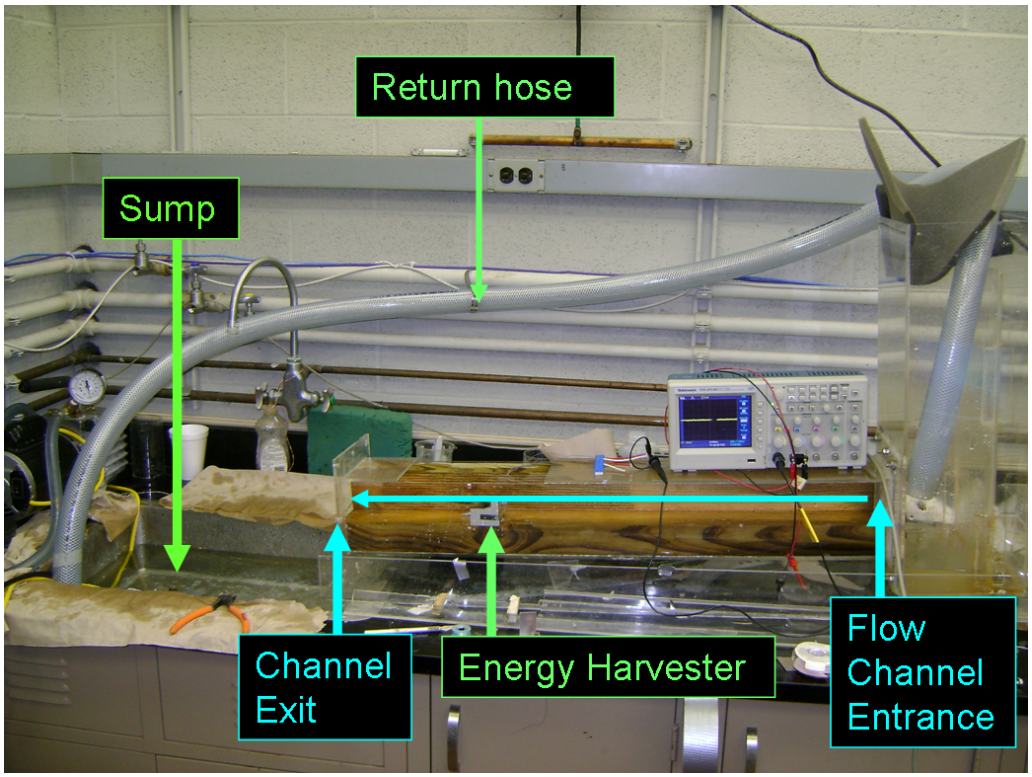


Figure 43: Mechanics of Active Materials Laboratory flume

Figure 43 shows the flume in which the experiments were performed. The flow channel inlet and outlet display the direction of flow from right to left. The flume is a closed system which is shown by the return hose. Figure 44 shows a close up view of the entire coupled energy harvester system. It was chosen to attach the magnets to the cantilever beam and hold the coils stationary because the magnet mass is much less than that of the coils. The leading cone was introduced to the system to reduce the wake effect at the inlet of the conical kite allowing higher input forces. Duct tape was utilized to fix the system to the floor and wall of the flume.

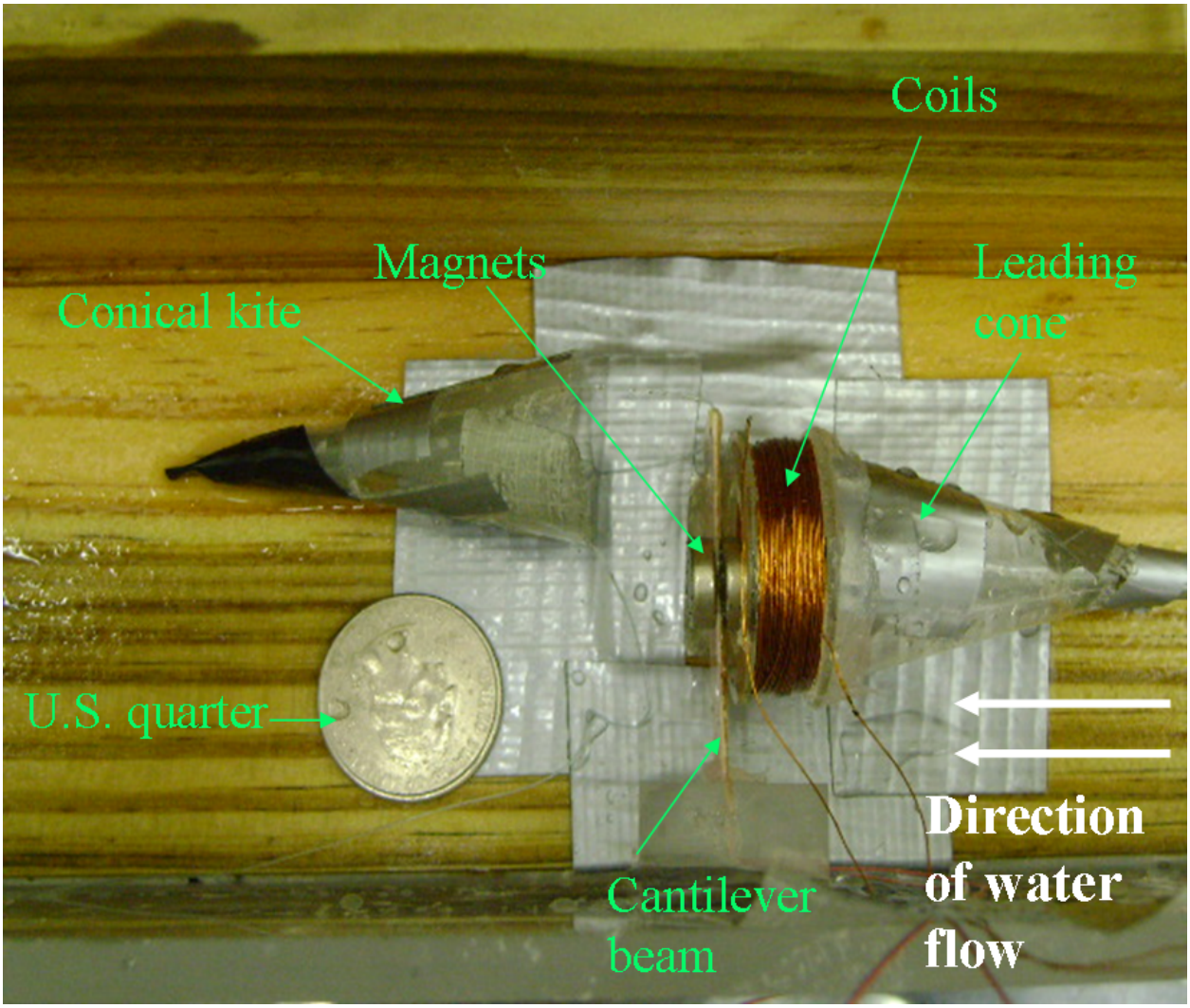


Figure 44: Close up of coupled system

## 3.5 EXPERIMENTAL RESULTS OF THE FLAPPING METHOD

The impedance matched load resistor for both the PVDF and electromagnetic systems were found experimentally with a resistance-capacitance circuit box. The impedance matched load resistance was found to be approximately 4.7 MΩ for the PVDF and approximately 33 Ω for the electromagnetic inductor. A typical voltage response with these load resistances is shown in Figure 45. The data was collected with a Tektronix digital oscilloscope.

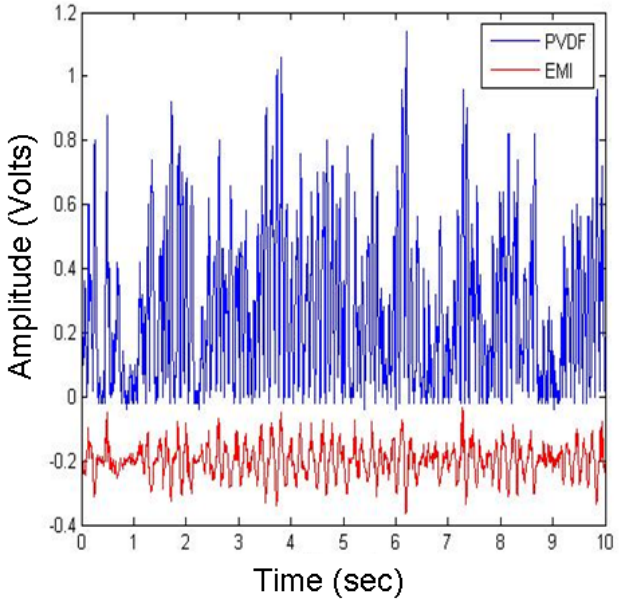


Figure 45: Time response of rectified PVDF voltage signal with a 4.7 MΩ load resistor and electromagnetic inductor voltage response with a 33 Ω load resistor and a -0.2 V bias

The electromagnetic induction voltage signal has a zero mean but a -0.2 V offset has been applied to set the lines apart. The electromagnetic induction output voltage was not rectified because the absolute value of the signal's magnitude was less than 200 mV at all times. The full wave rectifier circuit that was used was composed of diodes that needed a potential greater than 200 mV to allow current to flow. To rectify the signal an amplifier would be needed which turns the passive circuit made of strictly diodes into an active circuit that needs power which is undesirable. A coil with more turns or a smaller diameter wire

would remedy this problem, but the impedance matched load resistance would increase and would need to be experimentally found for this adjustment.

The following equation was used to calculate the average electrical power produced by the PVDF and electromagnetic inductor transducers;

$$P_{avg} = \frac{1}{T} \int_{t_o}^{t_o+T} \frac{V^2(t)}{R_{load}} \, dt \tag{3.15}$$

where P is the average power in watts, T is the total length of time that data was recorded in seconds, V(t) is the voltage signal, and $R_{load}$ is the load resistance. After twenty trials it was determined that the power produced by the PVDF was on average 25.2 nW with a standard deviation of 2.3 nW and the electromagnetic inductor produced on average 76.6 μW with a standard deviation of 3.0 μW.

Upon observation the beam deflects about 3 mmbetween 4-5 Hz. The predicted results for a beam of this size with this deflection and frequency of 5 Hz is 642 nW. If 642 nW is scaled to account for the coating layer (by multiplying 642 nW by 0.2 %) the expected reult becomes 13 nW , which is approximately one half the experimental result.

This system was also tested at a flow velocity of approximately 0.9 m/s and generated about 12 nW with the PVDF transducer and 40 μW with the inducor. Therefore, this proves that system is not senstive to the flow (at least not as sensitive as the VIVACE).

The current design has approximately 0.096 × 0.05 $m^2$ of surface area when viewed from the viewpoint shown in Figure 44. Therefore, about 200 devices can fit into 1 $m^2$ of surface area, which corresponds to a power rating of approximately 15 $mW/m^2$. This would correspond to about 68 W per 4456 $m^2$ of surface area, which is equivalent to the surface area of one American football field. Therefore, the flapping method does not generate a significant amount of electrical power and another device has been taken into consideration, which is discussed in the next chapter.

# 4.0 WINGMILL SIMULATION AND ANALYSIS

The flapping method proved not to be a feasible technique to produce a significant amount of electrical power. As a result, it was chosen to explore the effects of the power production of an existing device by adding a smart material energy harvester to it. The Wingmill device discussed in Chapter 1 and shown in Figure 12 has been considered for converting hydrokinetic energy to electrical energy via coupling electromagnetic induction and smart material transducers. This system has been considered because it satisfies the three primary requirements for the desired device in this work, which are:

1. The device must be considered an in-stream device, meaning that it can harness energy from currents.
2. The dynamics of the device must not be rotational.
3. The dynamics of the system are not velocity dependent/sensitive.

This chapter develops a model of the underwater Wingmill system shown in Figure 12 and determines its potential power production through a simulation in Matlab.

## 4.1 DEVELOPMENT OF THEORETICAL MODEL

The assumptions made in the model are as follows:

1. The fluid is water with a density, $\rho$, of 1000 kg/m$^3$
2. The fluid flow around the wing is one-dimensional, steady state, incompressible flow
3. The flow is uni-directional and perpendicular to the plunge motion of the wing

4. There is a linear spring force that acts on the wing where the geometry of the spring will be determined later. It is known that this spring will be made of PVDF, therefore, it will be able to generate power.
5. The wing is constrained to vertical motion (shown as the $y$ direction in Figure 54)
6. The wing pitches around its center of mass
7. There is a 90 degree phase difference between the pitch and plunge motion

A front view oriented such that the fluid flow is into the page and a side view schematic of the Wingmill system is shown in Figure 46.

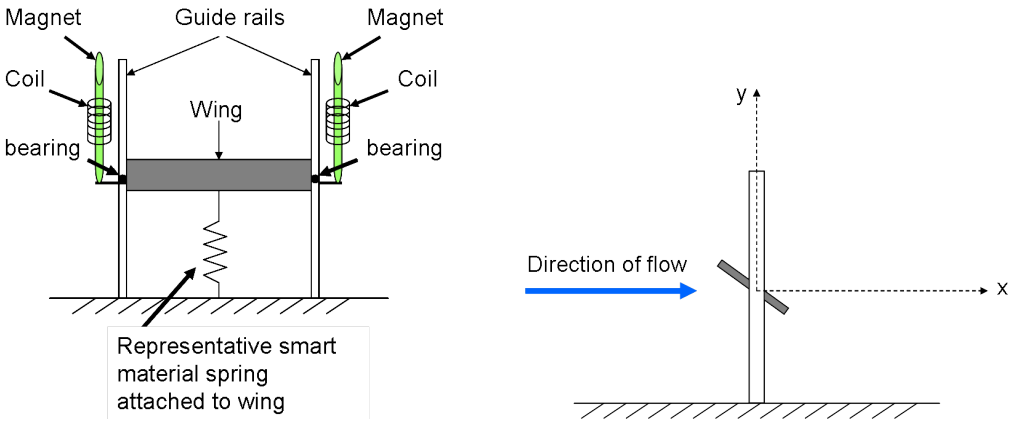


(a) Front view

(b) Side view

Figure 46: Schematic of the Wingmill system A) Front view B) Side view

The bearings in Figure 46(a) slide in a groove in the stationary guide rails, which constrain the wing to vertical motion. Magnet(s) attached to the wing pass through the core of the stationary coils positioned as shown in Figure 46(a), and the representative spring, made of smart material, is stressed allowing both of these transducers to produce electrical energy. Another important note is the placement of the coordinate system in Figure 46(b). When the wing is at the origin of the coordinate system the pitch (rotation of the wing) is at a maximum angle and the plunge (vertical wing displacement) is considered to be zero. When the wing's position is at the top extreme of the guide rail above the x-coordinate the pitch is zero and the plunge's amplitude will be considered a maximum and will be labeled $y_{max}$.

Conversely, when the wing's position is below the y-coordinate at the bottom extreme of the guide rail the pitch is zero and the plunge's amplitude will be considered a minimum and will be labeled $y_{min}$. The magnitudes of $y_{max}$ and $y_{min}$ are equivalent. This relationship between the plunge amplitude and pitch angle describes the 90 degree phase difference between the two and can be seen in Figure 47. In Figure 47, time moves from right to left.

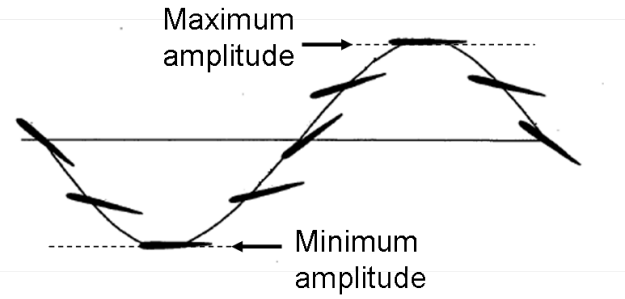


Figure 47: One cycle of a wing demonstrating the 90 degree phase difference between pitch and plunge

McKinney and Delaurier [40] and Jones et al. [35] both have shown that a phase angle of 90 degrees between the pitch and plunge allows a maximum possible efficiency of approximately 20 - 25% in the Wingmill system. The efficiency is defined as the ratio of the mechanical power extracted from the flow to the ideal power flowing through the control volume. The ideal power is 59 % of the total power flowing through the area swept out by the wing, where 59 % is referred to as the Betz coefficient [34].

The 90 degree phase difference must be enforced through the kinematics of the system. The next section explains in detail how this phase difference can be enforced and also provides a mathematical description of the kinematics.

### 4.1.1 Kinematics of the Wingmill System Assuming a 90 Degree Phase Difference Between the Pitch and Plunge

There are different methods in which to enforce the 90 degree phase difference. One was given in Chapter 1 and shown in Figure 13. Another possible design that may be able to

enforce a 90 degree phase difference between the pitch and plunge amplitude would utilize a bell crank, series of linkages, and a cam. This design is similar to the design given by Jones et al. [35] and is roughly described through the schematic of Figure 48.

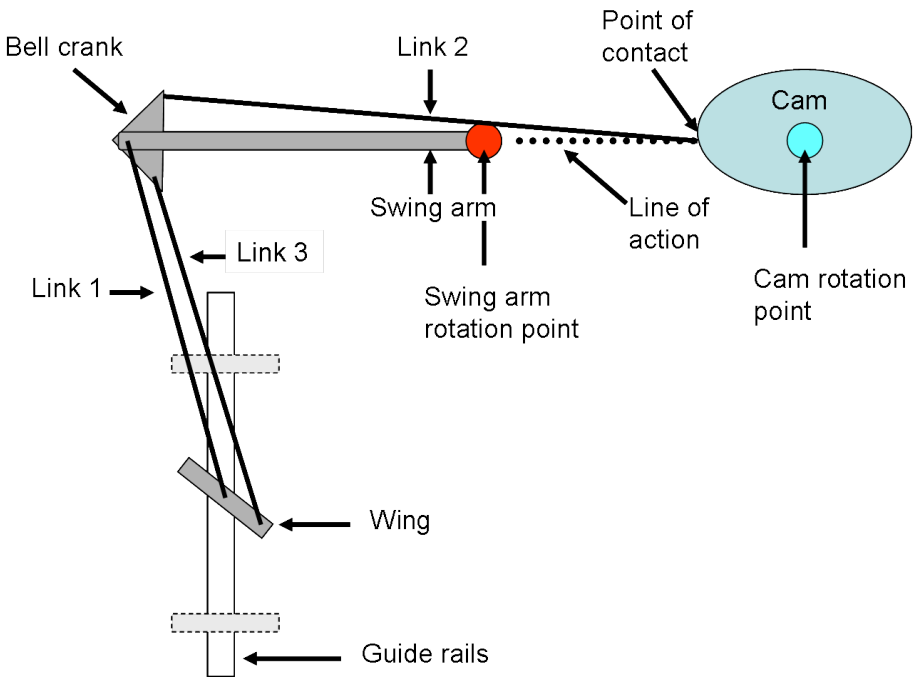


Figure 48: Schematic of Wingmill system with a cam design to enforce the 90 degree phase difference

In Figure 48 the circles labeled as rotation points of the cam and swing arm are the fixed points of the two apparatus. It will be assumed that the cam's rotation is generated by the motion of the swing arm and, therefore, is coupled to the plunge position because link 1 is attached to the pivot point of the wing and the bell crank and swing arm. Link 2 is the connection between the cam and the bell crank and the point of contact of link 2 to the cam always rides along the dotted line labeled as the line of action. The line of action is a telescoping device, shown in Figure 49, where link 2 is attached to the protruded piece so there is no interference between the link and the telescoping or stationary pieces. A wheel at the end of the telescoping device is the actual contact between the cam and link 2.

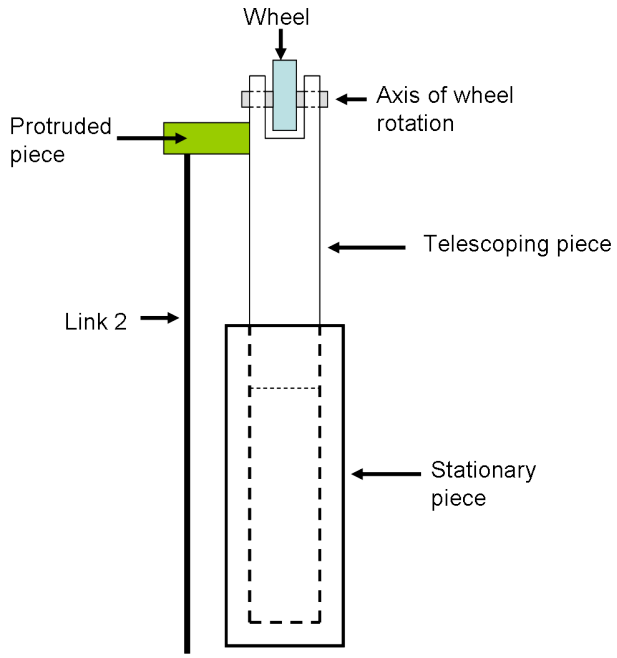


(a) Top view

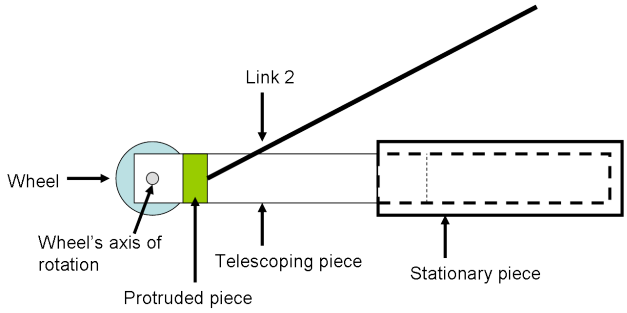


(b) Side view

Figure 49: Schematic of the telescoping device A) Front view B) Side view

As the wing plunges the cam will rotate and link 2 positions the bell crank such that link 3 pitches the wing to be 90 degrees out of phase with the plunge amplitude. Figure 50 represents a rough idea of how the cam could be designed.

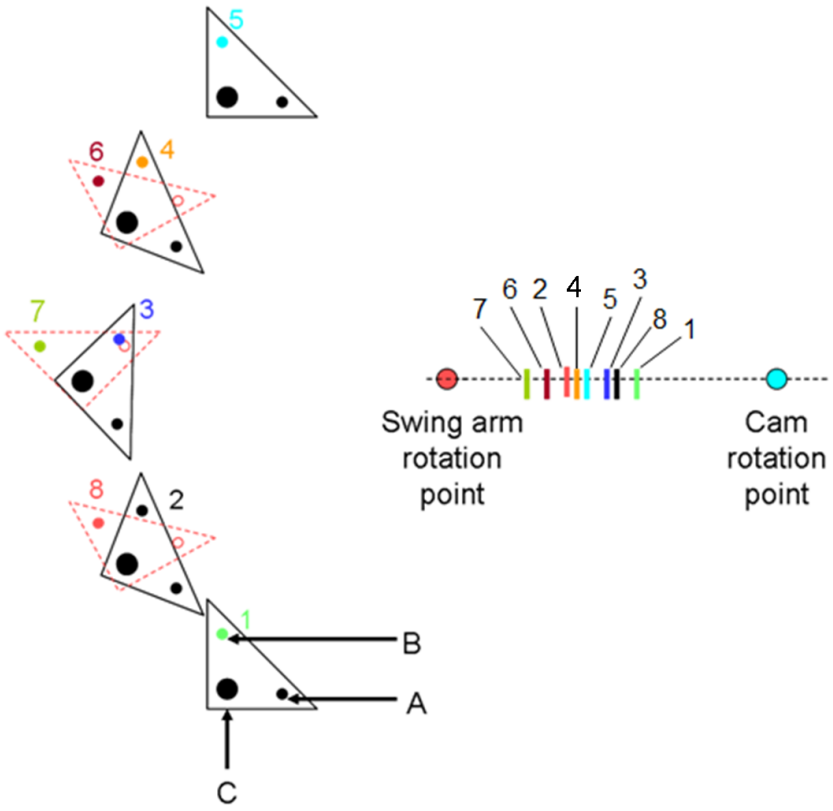


Figure 50: Design of the cam

Figure 50 shows different positions of the bell crank where position 1 represents the wing at the minimum plunge amplitude, positions 3 and 7 represent the wing at zero plunge where 3 is ascending and 7 is descending, and position 5 represents the wing at maximum plunge. The colored dots labeled B are where link 2 is attached to the bell crank, dot A is where link 3 is attached, and dot C is where link 1 is attached. The color-coded lines along the line of action correspond with the colored dots on the bell crank and they represent where the point of contact of link 2 with the cam needs to be positioned for a given plunge amplitude. This type of design would assume that the cam rotates 180 degrees from position 1,2,3,4 to position 5 (this represents the wing ascending) and then another 180 degrees from position 5,6,7,8 and back to position 1 (this would represent the wing descending).

The nature of the kinematics of the wingmill allows the pitch angle (angular position), $\theta$, to be represented as a function of the plunge (vertical position), $y$. Therefore,

$$\theta = f(y) \tag{4.1}$$

According to the imposed 90 degree phase difference between $\theta$ and $y$, when the wing ascends $\theta$ is at its maximum (or if the wing descends $\theta$ is at the negative of its maximum) when $y$ is zero, and $\theta$ is zero when $y$ is at the maximum (or at the minimum, which is equal but opposite to the maximum). Everywhere in between the maximum and minimum plunge amplitude $\theta$ can be expressed as equation 4.1. In the physical system the wing's plunge amplitude can never be greater than the maximum plunge amplitude, $y_{max}$, and can never be less than the minimum plunge amplitude, $y_{min}$. This can be seen in Figure 51.

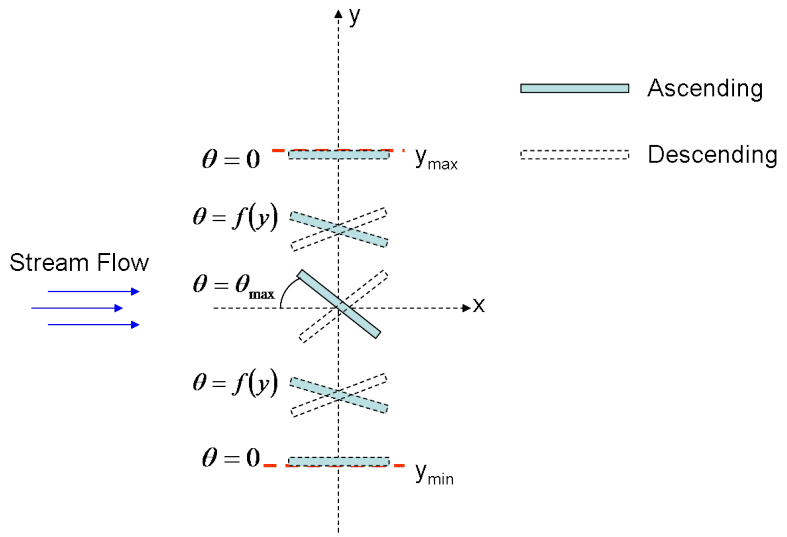


Figure 51: Motion of the wing showing relation between $\theta$ and $y$ when they are 90 degrees out of phase.

Therefore, $\theta$ can be written in terms of a cosine function, where the signum function takes into consideration if the wing is ascending or descending, as

$$\theta = \theta_{max} \cos\left(\frac{\pi}{2}\frac{y}{y_{max}}\right) \operatorname{sgn}(\dot{y}) \tag{4.2}$$

Because it is desired to generate energy utilizing a PVDF transducer in the form of a spring that will be attached to the wing, the previous problem is modified in simulation to accomodate an artificial constraint. The artificial constraint allows a convenient method for modelling the system by letting the wing travel beyond the maximum and minimum plunge limts if the spring constant is too low. When the is wing beyond these limits $\theta$ remains zero. This can be seen in Figure 52.

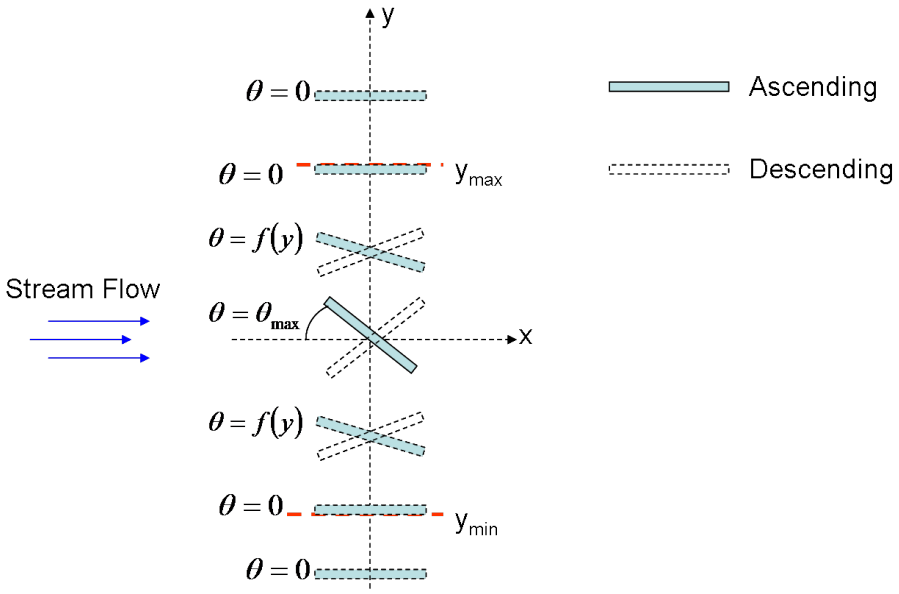


Figure 52: Motion of the wing showing the simulation kinematics.

Because of this artificial constraint, the function describing $\theta$ in terms of $y$ must be altered because equation 4.2 no longer accurately describes the kinematics of the system. The graph of Figure 53 shows how $\theta$ must be windowed with respect to $y$.

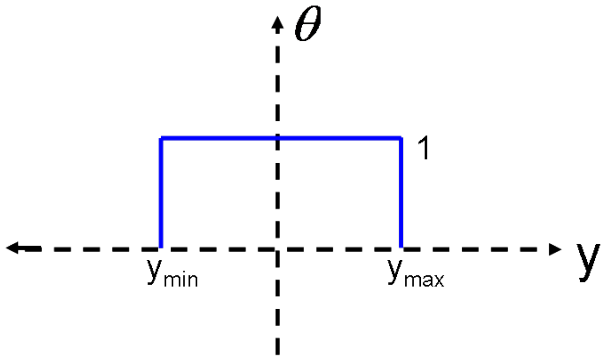


Figure 53: $\theta$ windowed with respect to $y$.

Therefore, if the unit-step is defined as a function of $y$ by

$$u_s(y) = \begin{cases} 1 & y_{min} < y < y_{max} \\ 0 & \text{otherwise} \end{cases} \tag{4.3}$$

in the simulation $\theta$ can be represented as

$$\theta = \theta_{max} \cos\left(\frac{\pi}{2}\frac{y}{y_{max}}\right) \operatorname{sgn}(\dot{y})\, u_s(y) \tag{4.4}$$

Note that in between $y_{min}$ and $y_{max}$, $\theta$ and $y$ are directly related so that they are 90 degrees out of phase, and outside of this range $\theta$ is forced to zero.

Using this model with the artificial constraint, the spring returns the wing's plunge amplitude back to zero if the response of the wing goes outside of the plunge limits. It is important to note that because a response of this nature is possible in the simulation, this method requires a spring whereas the model that is described by equation 4.2 does not. As a result, the objective is to determine the spring constant, for a given flow condition (free stream velocity), that results in amplitude of the maximum plunge limit, $y_{max}$. Thus, we can consider both the stiffness and generated power to be functions of $y_{max}$ and $U_\infty$. By doing this, for given flow conditions and design amplitude, the resulting response of the wing will resemble the physical system.

### 4.1.2 Derivation of Forces in Terms of the Model Parameters

Now that the assumptions and kinematics have been established, the development of a theoretical model for the Wingmill begins with determining the forces that act on the wing due to a constant fluid flow. The free body diagram (FBD) of the forces that act on the wing during ascension is shown in Figure 54. This figure displays a side view of the wing.

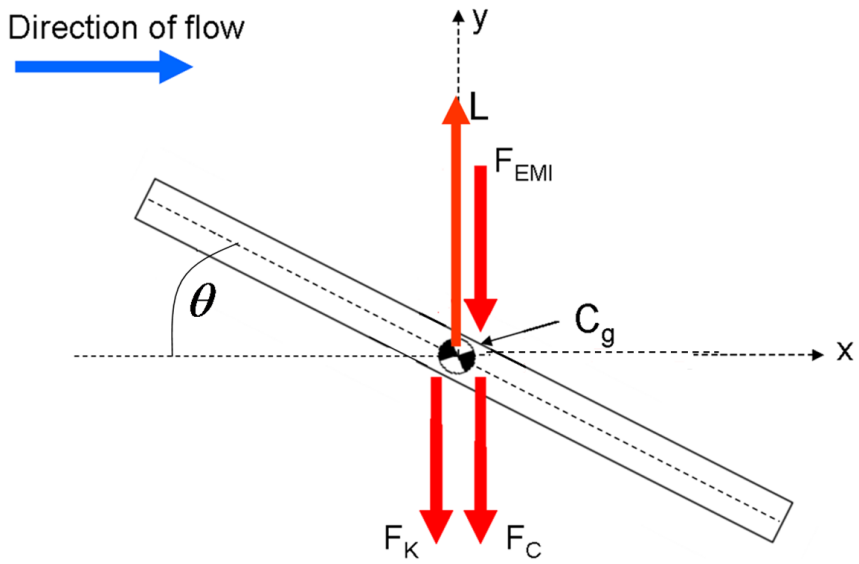


Figure 54: Free body diagram of the wing

In Figure 54 $\theta$ is the pitch angle, which is defined as the angle between the horizontal x-axis (along the direction of fluid flow) and position of the wing. The gravitational force is balanced against the static deflection of the spring and hence is not shown. All of the forces in Figure 54 are defined as follows:

- $L$ - Lift force (input)
- $F_K$ - Reaction force from spring
- $F_C$ - Damping force from friction and any other unpredicted damping force that acts on the system.
- $F_{EMI}$ - Electromagnetic induction damping force

A derivation of these forces in terms of their physical parameters is provided in following couple of pages.

Lift Force, $L$

For an airfoil in flow, if the interaction between the aerodynamic forces acting on the wing, elastic reactions, and inertia of the wing fall under certain conditions the wing will absorb energy and begin to flutter. The aerodynamic forces can be decomposed into a lift, drag, and moment. The lift force pulls the wing upward, the drag force pulls it aft (parallel to the free stream), and the moment causes it to pitch. In the wingmill system these same aerodynamic forces cause motion except that the pitch and plunge motions are coupled mechanically, therefore, the only force of interest is the lift force. For a thin airfoil the lift force can be described by

$$L = qSC_L(\alpha) \tag{4.5}$$

where $q = \frac{1}{2}\rho U_\infty^2$ is the dynamic pressure ($U_\infty$ is the free stream velocity and $\rho$ is the density of the fluid), $S$ is the platform area, and $\alpha$ is the angle of attack. If the wing velocity is zero $\alpha$ is equivalent to $\theta$, but the relative motion between the free stream velocity and the wing must be accounted for by considering the induced angle of attack, $\alpha_i$. Figure 55 represents this consideration and to simplify the problem assumes $\theta$ to be zero.

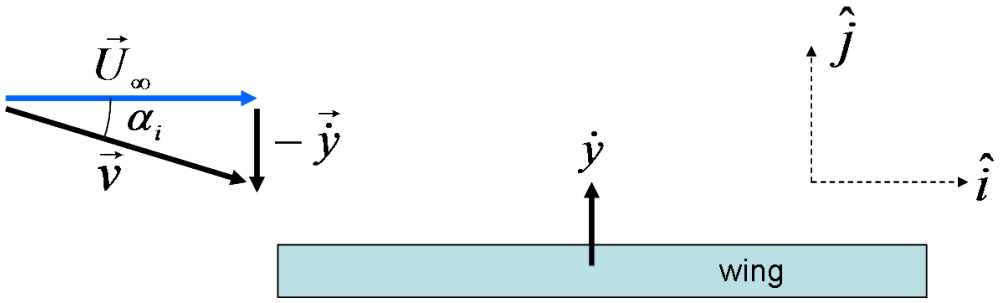


Figure 55: Representation of the induced angle of attack, $\alpha_i$.

The horizontal velocity of the flow with respect to wing is $\vec{U}_\infty$, and the vertical velocity of the flow with respect to the wing is -$\dot{\vec{y}}$; that is, opposite of the velocity of the wing with

respect to the flow. As shown in Figure 55, $\vec{v}$ is the total velocity of the flow with respect to the wing giving

$$\vec{v} = U_\infty \hat{i} - \dot{y}\hat{j} \tag{4.6}$$

From this it can be seen that the induced angle of attack can be represented by

$$\alpha_i = \tan^{-1}\left(-\frac{\dot{y}}{U_\infty}\right) \simeq -\frac{\dot{y}}{U_\infty} \tag{4.7}$$

where the approximation is legitimate for small angles. The total angle of attack is then given by

$$\alpha = \theta + \alpha_i = \theta - \frac{\dot{y}}{U_\infty} \tag{4.8}$$

For small angles the component in the vertical direction is the lift, and for a symmetric airfoil the lift coefficient can be approximated as

$$C_L(\alpha) = C_{L\alpha}\left(\theta - \frac{\dot{y}}{U_\infty}\right) \tag{4.9}$$

where $C_{L\alpha} = \partial C_L/\partial\alpha$ is the stability derivative. The value of the stability derivative depends upon the airfoil, for example, for flat plates Theodorsen theory shows that $C_{L\alpha} = 2\pi$. Therefore, the lift force can be written as

$$L = \frac{1}{2}\rho S U_\infty^2 C_{L\alpha}\left(\theta - \frac{\dot{y}}{U_\infty}\right) \tag{4.10}$$

Spring Force, $F_K$

The spring attached to the wing is the section of the Wingmill that is utilized to produce electrical energy through a smart material transducer. Initially, adequate information about the spring force is absent and must be empirically determined because if the spring force is too high for the input force then the wing structure will not oscillate and will reach a steady

state position. It has been assumed that there is a linear spring force acting on the wing, as a result this spring force, $F_K$, is represented by

$$F_K = ky \tag{4.11}$$

In equation 4.11 k is the effective stiffness of the spring and y is the distance the spring is stretched from its equilibrium position. Since the spring is attached to the wing and the plunge amplitudes are chosen the stiffness of the spring is the variable that needs to be determined. From the simulation the greatest spring stiffness that allows oscillation has been empirically found for a range of free stream velocities and plunge amplitudes. Once these stiffnesses have been determined the physical spring can be designed. For example, shown in Figure 56(a) is a slender prismatic bar with a longitudinal vibration that has a certain associated stiffness, or shown in Figure 56(b) is a cantilevered beam with a transverse vibration that has a different associated stiffness [32].

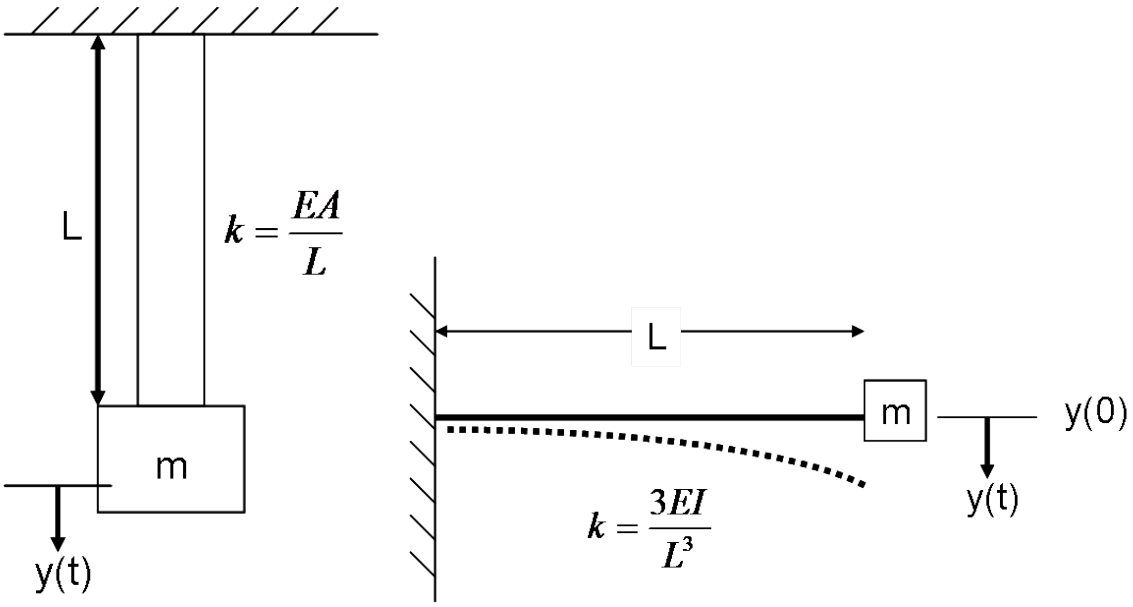


(a) Bar

(b) Beam

Figure 56: Stiffness associated with A) Prismatic bar B) Cantilever beam

In Figures 56(a) and 56(b) $E$ is the elastic modulus, $L$ is the length of the bar and beam, respectively, and $y(t)$ is the deflection of each from equilibrium. The variable $A$ is the cross-sectional area of the bar and $I$ is the second moment of inertia of the beam for the stiffness relationships. It would be assumed that if the beam were to be utilized to generate power, it would be a composited beam that has a substrate layer and at least one layer of smart material that is stressed when the beam is deflected. If the bar is to be utilized to generate power, the bar itself will be made of PVDF and will be stressed axially. There are many other spring designs, but the optimal spring is considered to be the spring that has the smallest footprint with the highest power output.

Damping Force from Kinematics, $F_C$

The damping force, $F_C$, represents frictional damping from the bearings and any other moving parts as described in the explanation of the operation of the Wingmill in the Oscillating Devices section of Chapter 1. This force is represented by equation 4.12 and is the product of a damping coefficient and the plunge velocity of the wing.

$$F_C = c\dot{y} \tag{4.12}$$

The damping coefficient has been chosen such that if there were no other retarding forces acting on the wing other than friction, the system's damping ratio $\zeta$ (zeta), is 0.01. Therefore, it is assumed that the friction in the system will not affect the dynamics to a significant degree.

Electromagnetic Induction Damping Force, $F_{EMI}$

Agutu [11] gives an in depth derivation of the damping force on a conducting loop in a flaring magnetic field, as shown in Figure 57. This derivation is based on Saslow's method [51] and the result is described by equation 4.13.

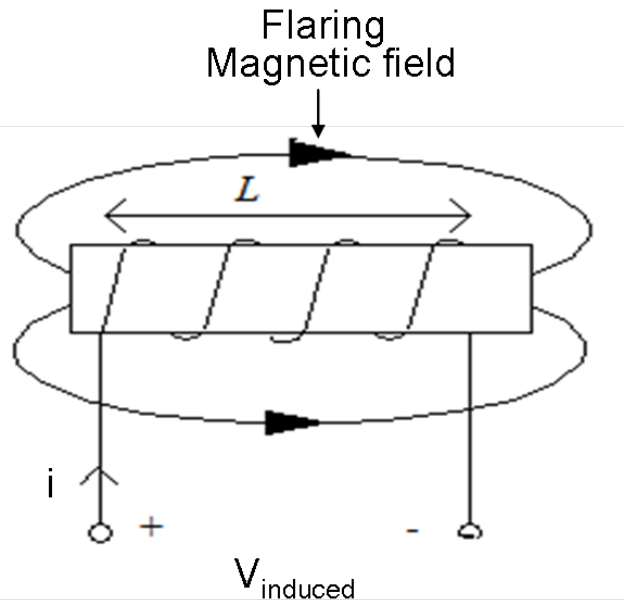


Figure 57: Conductor shaped into loops forming coils

$$F_{EMI} = 2\pi aNB\frac{V}{R_{wire}} \tag{4.13}$$

In equation 4.13 a is the coil radius, $N$ is the number of turns of the coil, $B$ is the magnitude of the magnetic field, $V$ is the induced voltage across the leads of the conductor, and $R_{wire}$ is the resistance of the wire given by

$$R_{wire} = \rho\frac{l}{A_{wire}} \tag{4.14}$$

where $\rho$ is the resistivity, $l$ is the length, and $A_{wire}$ is the cross-sectional area all of the wire.

The induced voltage, $V_{induced}$, in a coil with N turns according to Faraday's Law of electromagnetic induction [29] is expressed as

$$V_{induced} = N\frac{d\phi}{dt} \tag{4.15}$$

where $\phi = |B|\,|A|\cos(\alpha)$ and is the magnetic flux. B is the magnetic field strength, $\alpha$ is the angle between B and the normal to the area of the element as shown in Figure 58, and A is the area of the element that the field passes through.

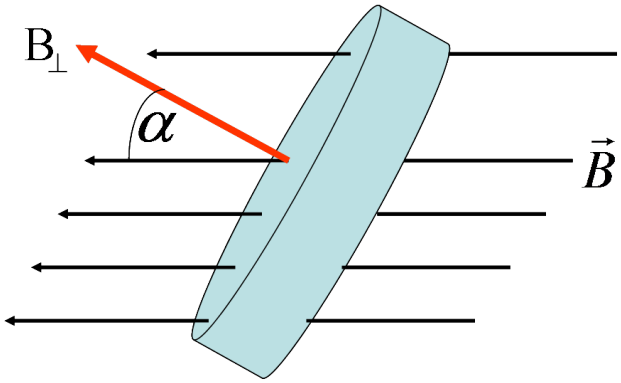


Figure 58: Visual representation of the angle $\alpha$ used to calculate the magnetic flux

When the coils move perpindicular to the magnetic field with a given velocity, $v$, the induced voltage is at a maximum and is described by

$$V_{induced} = NBlv \tag{4.16}$$

The length, $l$, of the wire is proportional to the circumference of the wire multiplied by the number of turns. For a coil $l = 2\pi rN$. Therefore, equation 4.13 can be rewritten as

$$F_{EMI} = 2\pi a \frac{N^2 B^2 l}{R_{wire}} v \tag{4.17}$$

## 4.2 EQUATION OF MOTION

Newton's second law of motion is applied to obtain the equation of motion. In Figure 54 $F_X$ is the reaction force from the guide rails in the Wingmill system, and the summation of forces in the x-direction is zero because they are balanced by this force. According to Figure 54, the sum of the forces in the y-direction are represented by

$$\sum F_y = L - F_K - F_C - 2F_{EMI} \tag{4.18}$$

$F_{EMI}$ has been multiplied by a factor of two because as shown in Figure 46(a) an inductor can be placed on both sides of the wing. When the forces in the y-direction are represented by their physical parameters, in standard form equation 4.18 can be expressed as

$$\ddot{y} = \frac{1}{2m}\rho S U_\infty^2 C_{L\alpha}\theta\left(y\right) - \left(\frac{c}{m} + \frac{1}{2m}\rho S U_\infty C_{L\alpha} + 2\pi a\frac{N^2B^2l}{mR_{wire}}\right)\dot{y} - \omega_N^2 y \tag{4.19}$$

Using the parameterization of $\theta$ in terms of $y$ from above gives

$$\ddot{y} = \frac{\theta_{max}}{2m}\rho S U_\infty^2 C_{L\alpha}\cos\left(\frac{\pi}{2}\frac{y}{y_{max}}\right)\mathrm{sgn}\left(\dot{y}\right)u_s\left(y\right) - \frac{c_{equ}}{m}\dot{y} - \omega_N^2 y \tag{4.20}$$

where $c_{equ}/m$ is represented as

$$\frac{c_{equ}}{m} = 2\zeta_{tot}\omega_N = \frac{c}{m} + \frac{1}{2m}\rho S U_\infty C_{L\alpha} + 2\pi a\frac{N^2B^2l}{mR_{wire}} \tag{4.21}$$

where $\zeta_{tot}$ is the total damping ratio for the whole system.

It can be seen from equation 4.20 that there is a non-linear term associated with the lift force. Because of this non-linear term the integrator chosen to numerically solve this equation was the fourth order Runge-Kutta method. The generated Matlab code can be seen in Appendix A and the results from the simulation are shown and discussed in the following section.

## 4.3 SIMULATION RESULTS

The Matlab simulation is used to determine the stiffest permissible spring that will allow oscillation for a range of free stream velocities and plunge amplitudes. This was done by creating a stiffness vector, $k_{vec}$, in which the first element is an extremely high stiffness value and the last element is a very low stiffness value. The simulation iterates through this vector decreasing the stiffness until a value that allows oscillation is found. If the stiffness value is too high the input force from the flow will not be able to overcome the increasing spring force and allow the wing to roll over. Therefore, the stiffness that is found for each free stream velocity will allow the wing to oscillate at the given maximum plunge. A typical simulation consists of plotting the plunge and pitch amplitudes along with the velocity of the wing. By plotting the plunge amplitude, it can be confirmed that the stiffness value found by the simulation for a given free stream velocity and plunge amplitude allowed the wing to oscillate. The velocity and pitch plots were used to verify the 90 degree phase difference by showing that the wing was at a maximum velocity and pitch at zero plunge and at zero pitch and velocity at the maximum and minimum plunge amplitudes. For every simulation the maximum pitch amplitude is 0.297 radians (17 degrees), which is assumed to be the stall angle of the wing, and the initial conditions of the wing are at maximum plunge and zero velocity.

There are three different types of responses that can arise. The first is if the spring is too stiff, the second is if the spring is not stiff enough, and the third is if the spring value is just stiff enough to allow oscillation. Figure 59 shows the response if a maximum plunge amplitude of 100 mm is desired and the stiffness value is too stiff.

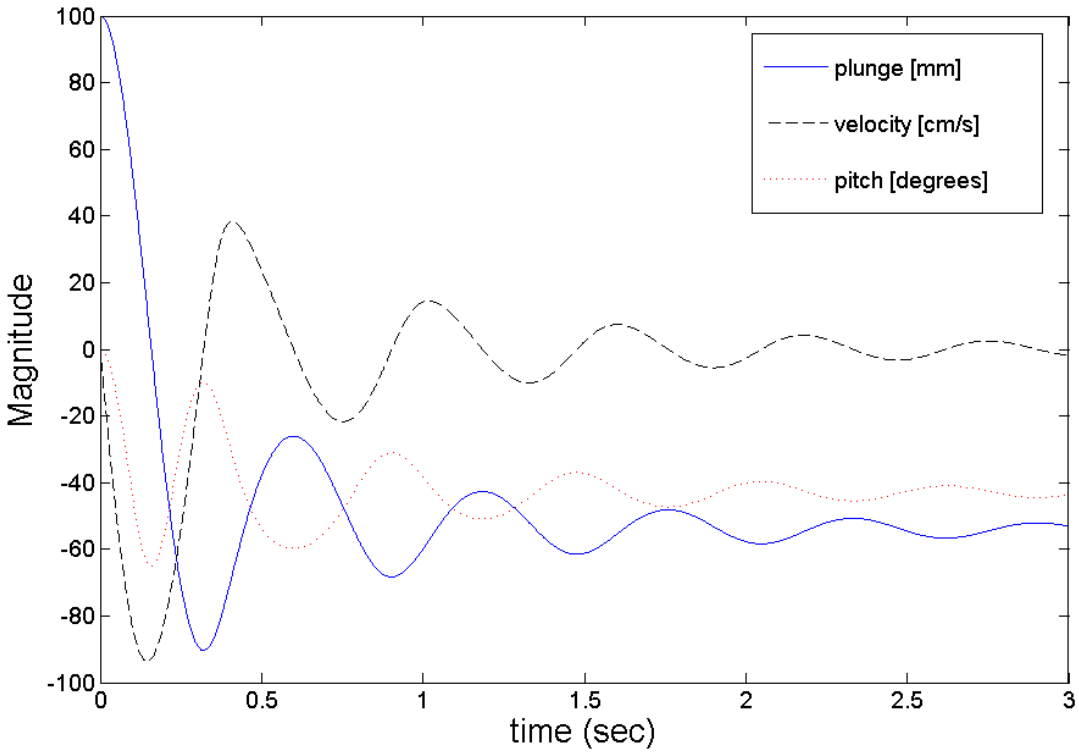


Figure 59: Simulation with spring too stiff for a maximum plunge amplitude of 100 mm and free stream velocity of 1 m/s

It can be seen by Figure 59 that the wing experiences a transient response and the pitch and plunge amplitudes begin to reach constant steady state values. In this case, the spring force becomes too high for the stream forces to overcome the spring force, therefore, the wing can not roll over and ascend to the max plunge.

Figure 60 shows the response if a maximum plunge amplitude of 100 mm is desired and the stiffness value is too low.

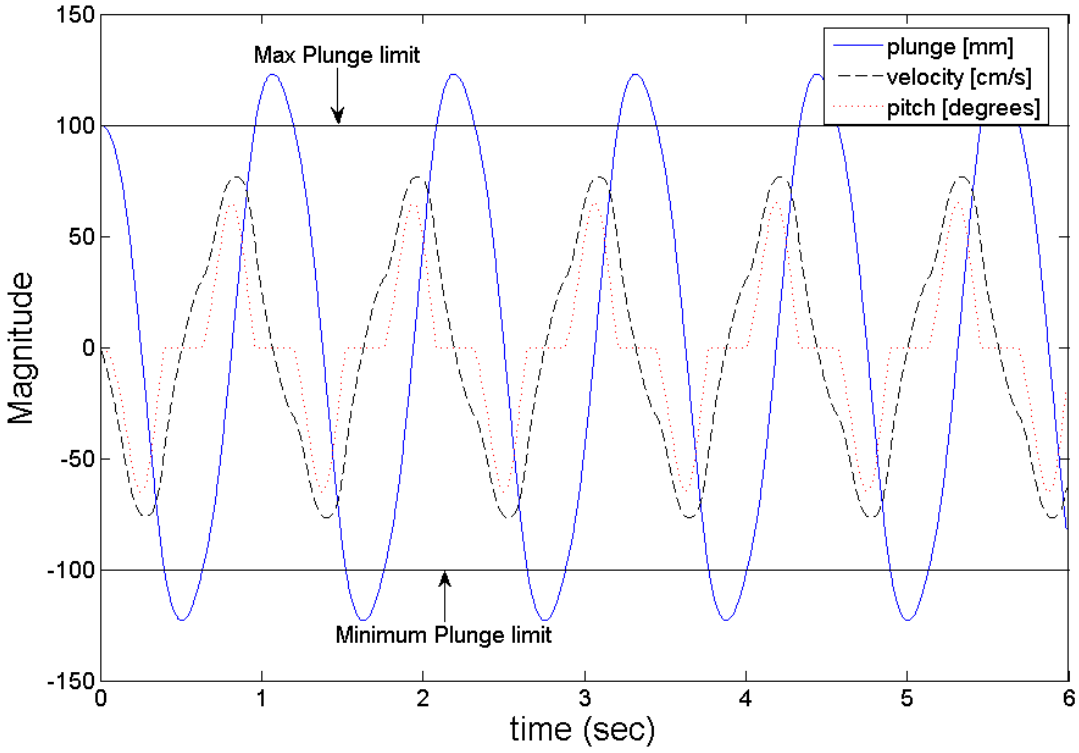


Figure 60: Simulation with spring not stiff enough for a maximum plunge amplitude of 100 mm and free stream velocity of 1 m/s

Figure 60 shows that the simulation predicts the wing will overshoot the desired maximum plunge amplitude of 100 mm, and when the restoring force in the spring becomes great enough the wing returns. This figure also shows that the pitch amplitude remains zero for any plunge amplitude greater than the desired maximum, which is preferred since the input force does not affect the dynamics in this region. This scenario is the reason for the artificial constraint explained in the kinematics section and would resemble Figure 52.

Figure 61 represents a typical simulation where the spring stiffness is just stiff enough to allow oscillation with no overshoot.

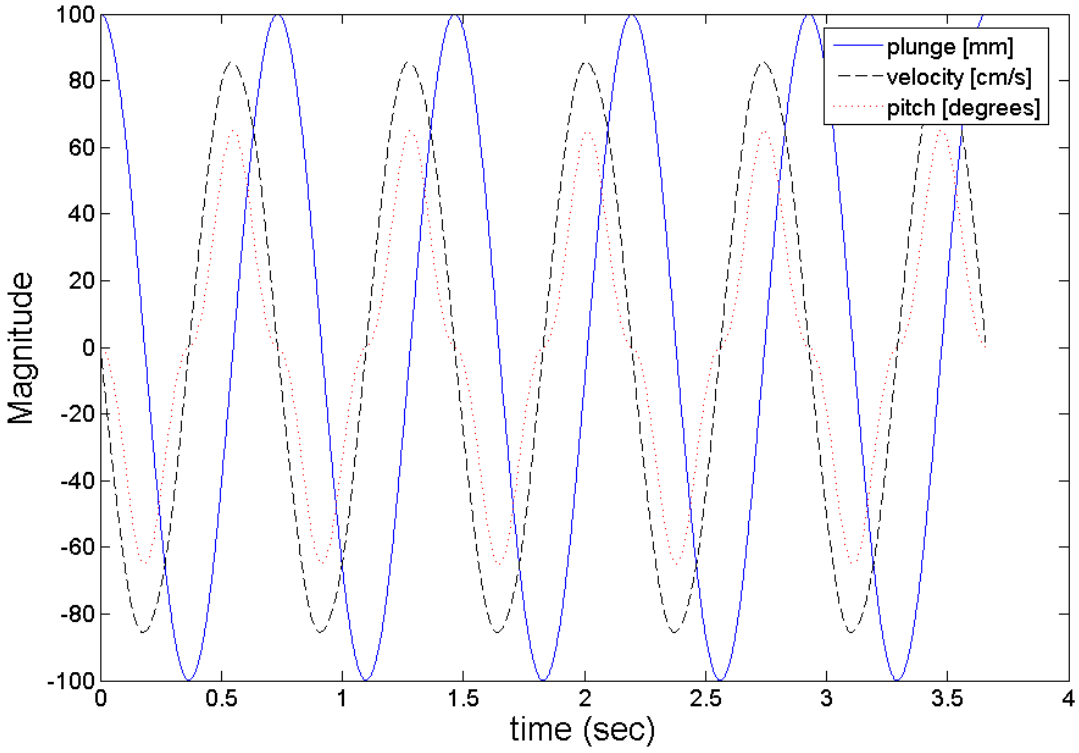


Figure 61: Simulation with spring just stiff enough to allow oscillation with zero overshoot for a maximum plunge amplitude of 100 mm and free stream velocity of 1 m/s

Shown in Figure 61 the plunge and pitch amplitudes are 90 degrees out of phase, and when the plunge amplitude reaches either a maximum or minimum the pitch amplitude rolls over smoothly. For this scenario, if the free stream velocity is increased and the spring stiffness is not adjusted the wing will stop oscillating and will reach steady state. If the free stream velocity is decreased and the spring stiffness is not adjusted the response will resemble that of Figure 60. Therefore, the scenario shown in Figure 61 is highly sensitive to flow rate, but the importance of this scenario is it discovers the spring that can produce the maximum power.

As a result of these three scenarios if a conceptual plot of the power of the Wingmill system, with a spring attached to it, is plotted against the velocity the trend would resemble the one shown in Figure 62. This figure shows that for a constant spring stiffness and plunge

limit if the stream velocity is too low in effect the spring is too stiff and the system will not oscillate, thus no power is generated. As explained in the kinematics section, the objective of the simulation is to find the $k$ value that allows a deflection to the plunge limit, which will allow oscillation. This $k$ value can be seen in the Figure 62 as $k_{opt}$. When the stream velocity is increased in effect the spring becomes too soft. In Figure 62, region 1 corresponds to the response of Figure 59, region 2 (which is a single point) corresponds to the response of Figure 61, and region 3 corresponds to the response of Figure 60.

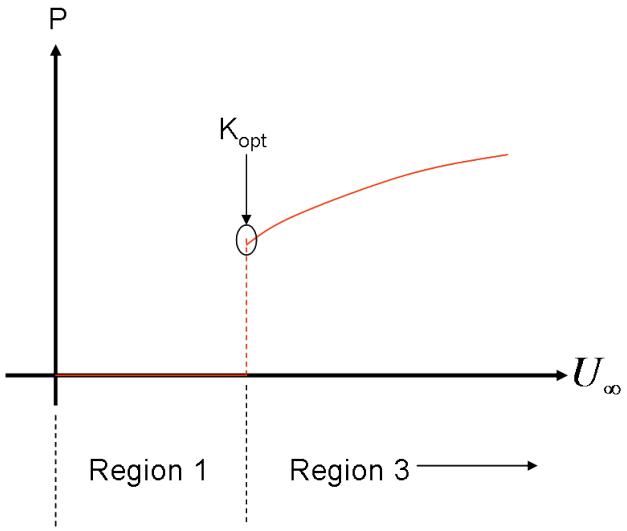


Figure 62: Conceptual plot of the generated power vs increasing velocity of the Wingmill system with a spring attached

For the simulation the following parameters were chosen to be constant for all free stream velocities and plunge amplitudes:

- The wing's mass, m, is set to 0.907 kg (This mass includes the mass of the magnets)
- The wing's area is set to 0.0217 $m^2$
- The maximum and minimum pitch amplitude is +/-17deg because this is approximately the stall angle

With these parameters set, Figure 63 shows the corresponding maximum stiffness values for each pair of chosen free stream velocity and plunge amplitude values.

For any given maximum stiffness value the frequency of oscillation can be determined because the wing oscillates at its natural frequency $\omega_N = \sqrt{k/m}$. Also, for each maximum $k$ a physical spring geometry was chosen and the footprint of the spring and the power produced by the smart material were determined. The two different spring geometries shown in Figure 56 were chosen to be analyzed and are discussed in the following two sections.

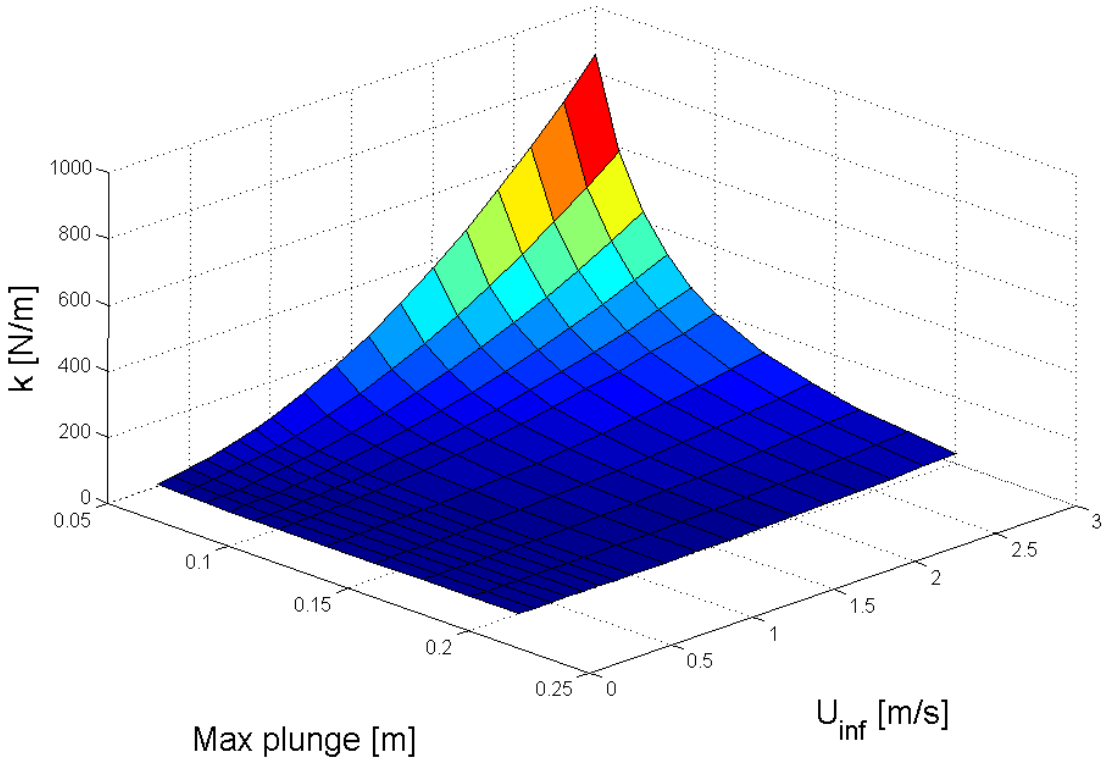


Figure 63: Maximum stiffness values that allow oscillation

### 4.3.1 Power Produced by a Longitudinal Vibrating Bar made of PVDF

Three assumptions were made in determining the power produced by longitudinal vibrating bar, the first is one end of the bar is attached to the wing and the other side is attached to a stationary object or ground. The other two assumptions made were there are no electrode or coating layers bonded to the PVDF and the bar has a rectangular cross section with its thickness chosen to be 110 µm. A thickness of 110 µm was chosen because this is a common

commercial thickness for PVDF. Choosing a thickness is arbitrary because the stresses in an axially loaded member depends on the applied force and cross-sectional area of the member. This stress is represented as

$$\sigma_{max} = \frac{F_{max}}{A} \tag{4.22}$$

where $F_{max}$ is the maximum force on the member that produces the maximum allowable stress and $A$ is the cross-sectional area of the member. If a specific stress is desired and the force is held constant then the area can be adjusted to obtain the desired stress. Since the bar's material is PVDF it is assumed that the desired stress in the bar is PVDF's maximum stress of 29.6 MPa because it was shown that the power produced by a piezoelectric element is heavily dependent on this variable. Since the member is assumed to be a rectangular cross-sectional bar, equation 4.22 can be rewritten as

$$\sigma_{max} = \frac{ky_{max}}{wt} \tag{4.23}$$

where $k$ is the stiffness found from the simulation, $y_{max}$ is the plunge amplitude, $w$ is the width of the PVDF bar, and t is its thickness. If the input force is represented as in equation 4.23, then there is a minimum length of the bar for each plunge amplitude that also needs to be determined. To find the minimum length of the bar the introduction of equation 4.24, which describes the stiffness of a prismatic bar, is necessary.

$$k_{bar} = \frac{E_{PVDF}A}{L} \tag{4.24}$$

In equation 4.24 $E_{PVDF}$ is the elastic modulus of PVDF, $A$ is the cross-sectional area of the bar, and $L$ is the length of the bar. Rewriting equation 4.24 in terms of the width, $w$, and thickness, $t$, of the rectangular cross-sectional bar and solving for the width gives

$$w = \frac{k_{bar}L}{tE_{PVDF}} \tag{4.25}$$

Substituting equation 4.25 into equation 4.23 gives the minimum allowable length of the bar when stressed to its maximum stress and is expressed as

$$L_{min} = \frac{y_{max} E_{PVDF}}{\sigma_{max}} \tag{4.26}$$

Equation 4.26 represents the minimum length of the bar because if it is any shorter the stiffness, $k$, will become too high and will prevent oscillation of the wing. Figure 64 shows the minimum length of the pure PVDF bar needed for each plunge amplitude so that the PVDF is stressed to its maximum stress. The trend in Figure 64 is expected because equation 4.26 shows that $L_{min}$ is linearly related to $y_{max}$.

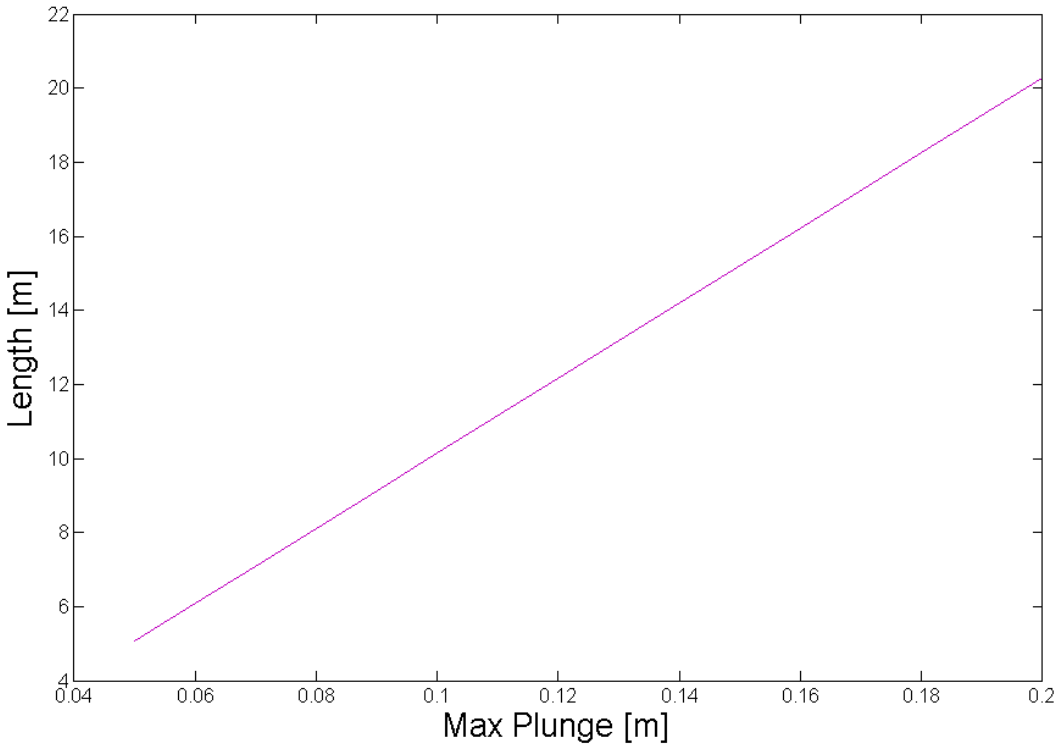


Figure 64: Minimum length of the pure PVDF bar needed to stress the PVDF to its maximum stress for each plunge amplitude

Once the minimum allowable length for each plunge amplitude has been established, it can be substituted into equation 4.25 to calculate the width needed to preserve the desired stiffness found from the simulation. After the width is determined for each $k$, all of the parameters needed to stress the PVDF to its maximum stress without plastic deformation have been found for every imposed plunge amplitude.

Figure 65 represents the power produced by an axially-stressed, pure PVDF, prismatic bar for every imposed plunge amplitude and free stream velocity according to equation 3.5.

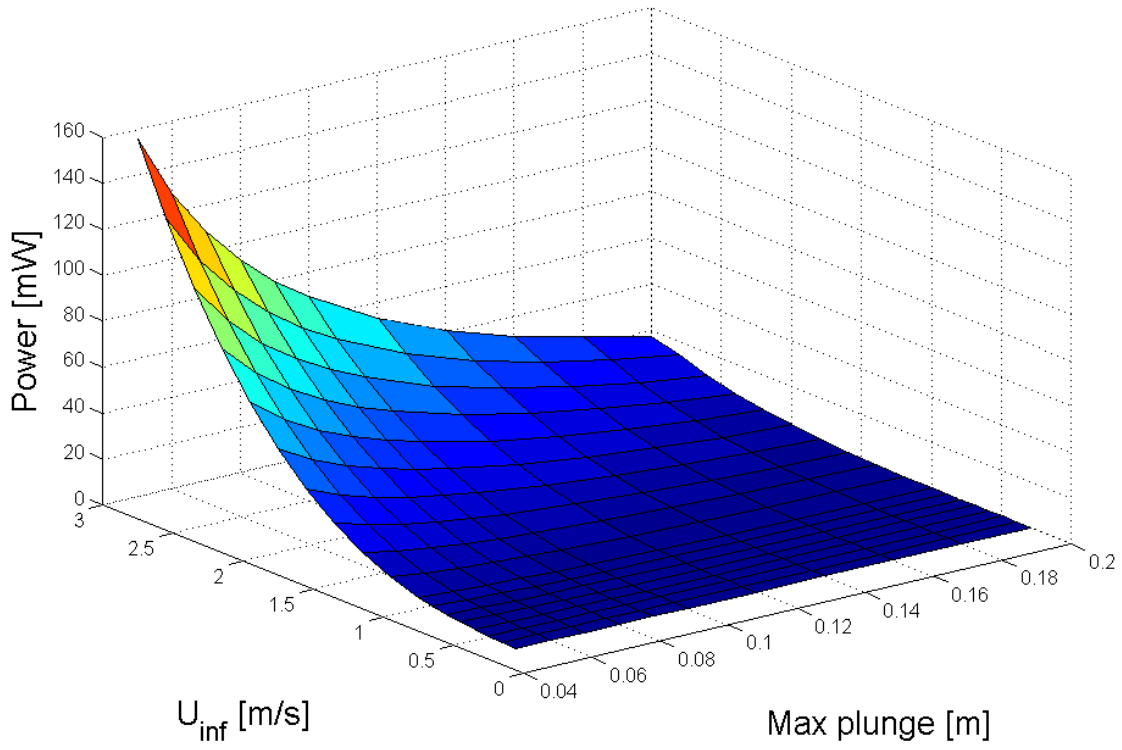


Figure 65: Power produced by a pure PVDF prismatic bar attached to the wing of the wingmill system for all free stream velocities and maximum plunge amplitudes considered

It can be seen that the theoretical maximum power output of the bar, which is approximately 160 mW, is at the maximum free stream velocity and the minimum plunge amplitude. The maximum volume of smart material is not found at this point but the maximum frequency of oscillation is found here because this is point of stiffest $k$ value found. The trend in Figure 65 makes sense because (as it will be shown in the Discussion of Results section) the

magnitude of the frequency of oscillation is much greater than the magnitude of the volume (about 4 orders of magnitude) making the volume of material insignificant in the generated power because the power is linearly related to both the frequency and volume according to equation 3.5. As a result it is the stiffness value that determines the maximum power output and not the volume of material. When the results of Figure 65 are scaled to include the effects of the electrode and coating layers the result is Figure 66, which shows the maximum generated power is approximately 0.3 mW.

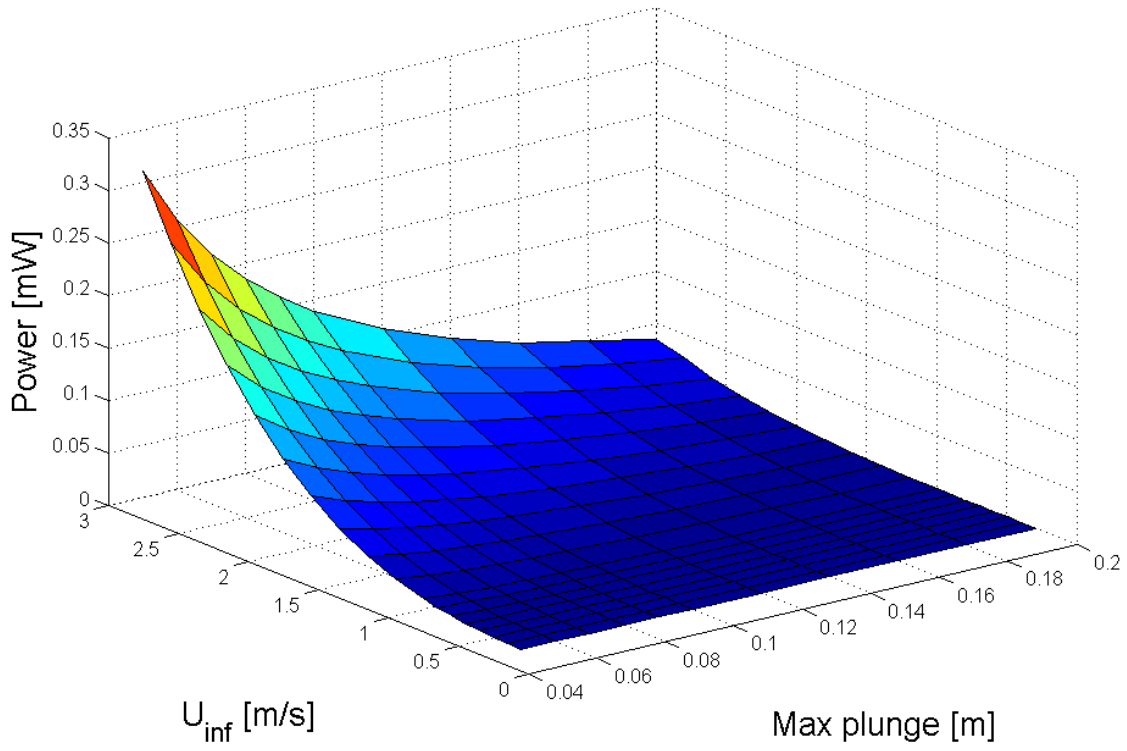


Figure 66: Adjusted generated power produced by a pure PVDF prismatic bar when considering the electrode and coating layers

The prismatic bar made of PVDF is not a feasible method to harness energy because the minimum length of the bar that is required to stress the PVDF to its maximum for every given scenario is too long. It is apparent that even at the shortest plunge amplitude, which is where the maximum power occurred for each free stream velocity as shown in Figure 66,

the minimum length of the pure PVDF bar is approximately 5 m. For this reason a triple-morph, cantilevered beam spring geometry was analyzed.

### 4.3.2 Power Production of a PVDF, Triple-morph, Cantilever Beam

The triple-morph, cantilever beam that was analyzed is assumed to have a substrate made of rubber metal because the stiffness of this material is much less than PVDF with a Young's modulus of 0.01 MPa. Therefore, more smart material will be able to be used in the beam. The thickness of the substrate is assumed to have a thickness of 6 μm. A triple-morph beam with PVDF as the smart material is shown in Figure 67.

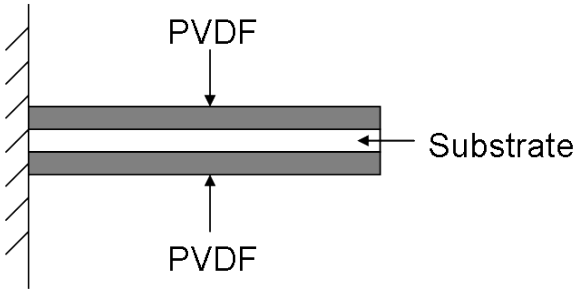


Figure 67: Schematic of a triple-morph beam

The beam's free end is attached to the wing and it is assumed to be oriented such that the PVDF has zero stress when the wing is at zero plunge and is at the maximum allowable stress at maximum and minimum plunge. As a result, energy can be harnessed two times every one full cycle. Figure 68 shows a schematic of the triple-morph beam attached to the Wingmill system.

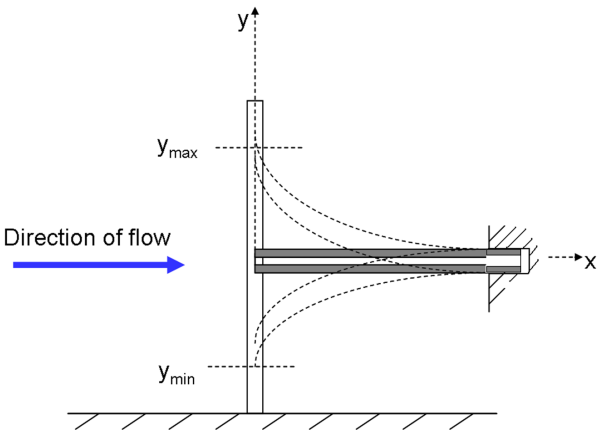


Figure 68: Schematic of a triple-morph beam attached to the Wingmill system

The beam is assumed to be attached to the pivot point of the wing. Therefore, the beam could be attached to the outside of the guide rails like the magnets or it could be attached to the wing itself. The motion of the tip of the beam in the x-direction could be accounted for by allowing the fixed part of the beam to have motion in the x-direction only as shown in the Figure 68. If the beam is to be attached to the wing directly a piece of the wing would have to be removed, as shown in Figure 69, so that the beam does not interfere with the pitching motion. Figure 69 is a top view of the wing where the red area is the removed section.

The parameters of the beam that need to be found are the length, thickness, and width, which are optimized to generate the maximum stress in the PVDF. The maximum longitudinal stress in a cantilever beam was given in equation 3.11 (Equation 11 Chap 3). If the transverse input force is at the free end of the beam the moment, $M$, can be expressed as

$$M = FL = ky_{max}L \tag{4.27}$$

where $k$ is the stiffness of the beam, $y_{max}$ is the maximum deflection of the free end of the beam, and $L$ is the length of the beam. The stiffness of a cantilever beam is represented by

$$k = \frac{3E_{PVDF}I}{L^3} \tag{4.28}$$

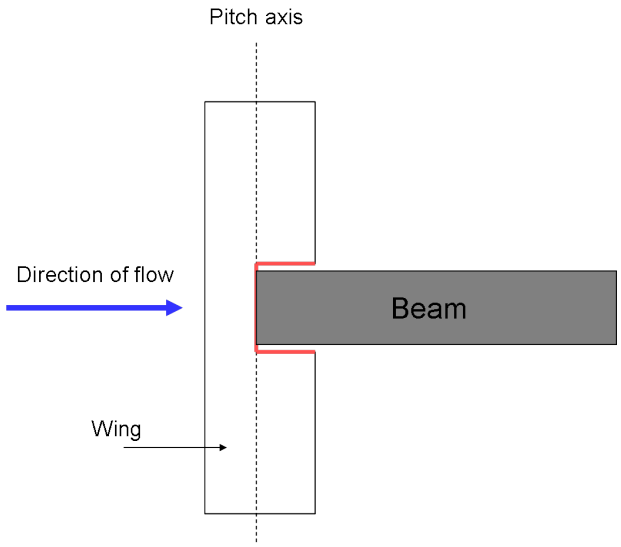


Figure 69: Top view of wing with removed section of the wing for accommodation of the beam

In Equation 4.28 $I$ is the second moment of inertia about the neutral axis, and $L$ is the length of the beam. Substituting equations 4.28 and 4.27 into equation 3.11 (Equation 11 Chap 3) gives

$$\sigma_{max} = \frac{3cy_{max}E_{PVDF}}{L^2} \tag{4.29}$$

Equation 4.29 shows that there are four different variables that determine the maximum longitudinal stress in a cantilever beam and $\sigma_{max}$, $E_{PVDF}$, and $y_{max}$ are known because $y_{max}$ represents the chosen maximum plunge amplitude. Therefore, there are two unknowns and one equation and as a result, the length of the beam has been chosen to always be five times the maximum plunge amplitude. Also, since the triple-morph beam is symmetrical $c = t_1/2 + t_2$ where $t_1$ is the substrate thickness and $t_2$ is the thickness of one of the PVDF layers. Therefore, equation 4.29 can be expressed as

$$\sigma_{max} = \frac{3}{25}\frac{E_{PVDF}\left(\frac{t_1}{2} + t_2\right)}{y_{max}} \tag{4.30}$$

Finally, solving for $t_2$ gives the required thickness of PVDF that will stress it to the maximum allowable stress without plastic deformation and is given as

$$t_2 = \frac{25}{3}\frac{\sigma_{max} y_{max}}{E_{PVDF}} - \frac{t_1}{2} \tag{4.31}$$

Now that the length and thickness of the beam have been determined the width will be calculated so that the stiffness values found by the simulation are preserved. This is accomplished by utilizing equation 4.28. The moment of inertia, $I$, of the triple-morph beam can be represented by applying the parallel axis theorem to give

$$I = \frac{1}{12} w_1 t_1^3 + 2\left[\frac{1}{12} w_2 t_2^3 + w_2 t_2 \left(\frac{t_1}{2} + h_2\right)^2\right] \tag{4.32}$$

where $w_1$ is the width of the substrate and $w_2$ is the width of the PVDF. Since the triple-morph beam is considered a composite beam, to accurately represent the moment of inertia the beam is transformed into a single material. This was done by transforming the substrate into PVDF by representing its width as

$$w_1 = w_2 \frac{E_1}{E_{PVDF}} \tag{4.33}$$

Therefore, equation 4.32 can be written as

$$I = w_2 \left\{\frac{E_1}{12 E_{PVDF}} t_1^3 + 2\left[\frac{1}{12} t_2^3 + t_2 \left(\frac{t_1}{2} + h_2\right)^2\right]\right\} \tag{4.34}$$

Substituting equation 4.34 into equation 4.28 and solving for $w_2$ gives the width needed to preserve the stiffness values found from the simulation. These widths also represent the maximum allowable width of the beam because if the beam is any wider it will be too stiff and will prevent oscillation of the wing.

Figures 70 and 71 show the results of calculating the thicknesses and widths in the described manner.

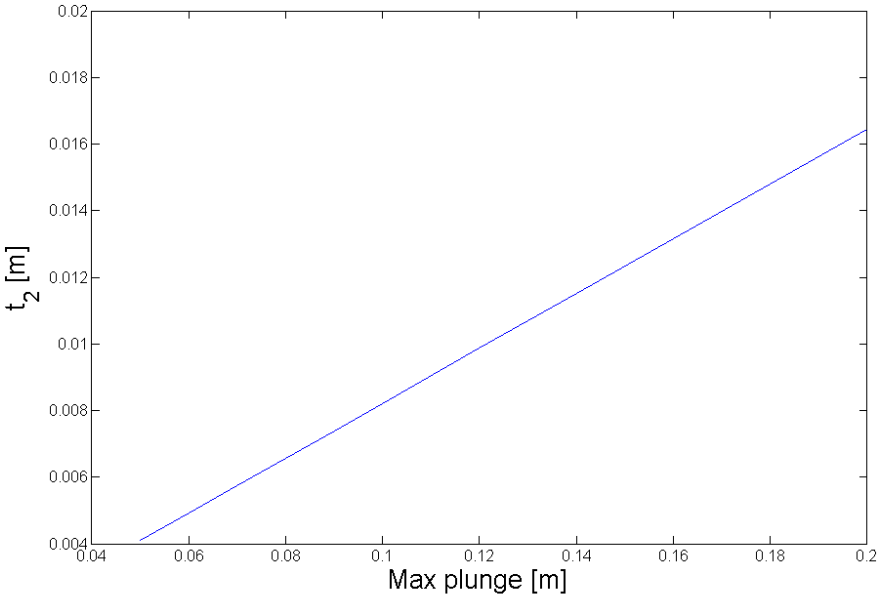


Figure 70: Thickness of one layer of PVDF to stress it to the maximum allowable stress when the length of the beam is constrained to five times the maximum plunge amplitude

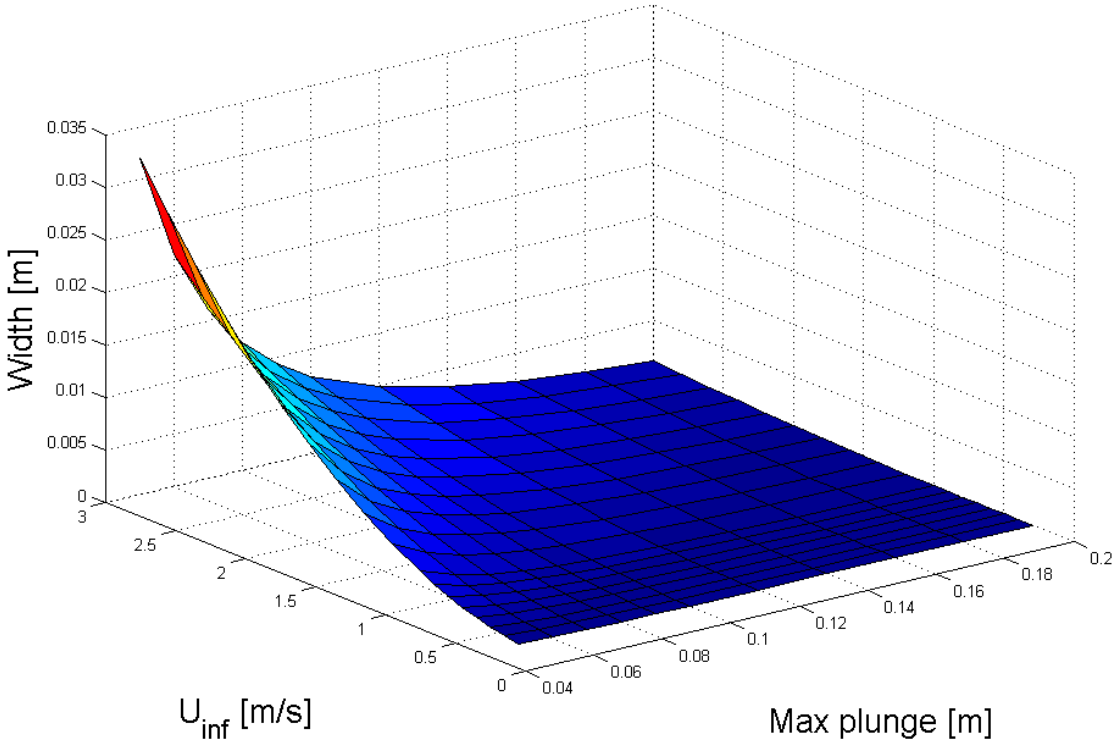


Figure 71: Width of beam needed to preserve the required stiffness for oscillation

The results of Figure 70 are expected because the thickness of the PVDF is determined by equation 4.31, which shows that the thickness of the PVDF is linearly proportional to $y_{max}$. The trend of Figure 71 makes sense because for a given plunge amplitude as the velocity increases the beam will need to become stiffer (or wider) to maintain oscillation. Also, for a given free stream velocity as the plunge amplitude increases the beam should becomes less stiff (or thinner) to maintain oscillation.

Kim [36] has derived a method to determine the electrical energy produced by a triple-morph beam for an applied tip force, $F_o$. The result is similar to the bimorph beam energy generation and can be expressed as

$$U_{gen} = \frac{18 d_{31}^2 s_m^2 t_2 (t_1 + t_2)^2 L^3}{\epsilon_{33}^T W X_{11}^2 \left\{ 1 + \left( \frac{6 s_m t_2 (t_1 + t_2)^2}{X_{11}} - 1 \right) K_{31}^2 \right\}} F_o^2 \tag{4.35}$$

The variable $X_{11}$ is given as

$$X_{11} = 12s_m t_2^2 t_1 + 8s_m t_2^3 + 6s_m t_2 t_1^2 + s_{11}^E t_1^3 \tag{4.36}$$

and $K_{31}$ is represented as equation 3.9.

To determine the power produced by a triple-morph beam, equation 4.35 is multiplied by the frequency of the applied force. Therefore, the power generated by a triple-morph for each free stream velocity and plunge amplitude considered is expressed as

$$P_3 = U_{gen}\left(\frac{\omega_N}{2\pi}\right) \tag{4.37}$$

The theoretical power generated by the triple-morph, cantilever beam as a result of equation 4.37 is shown in Figure 72.

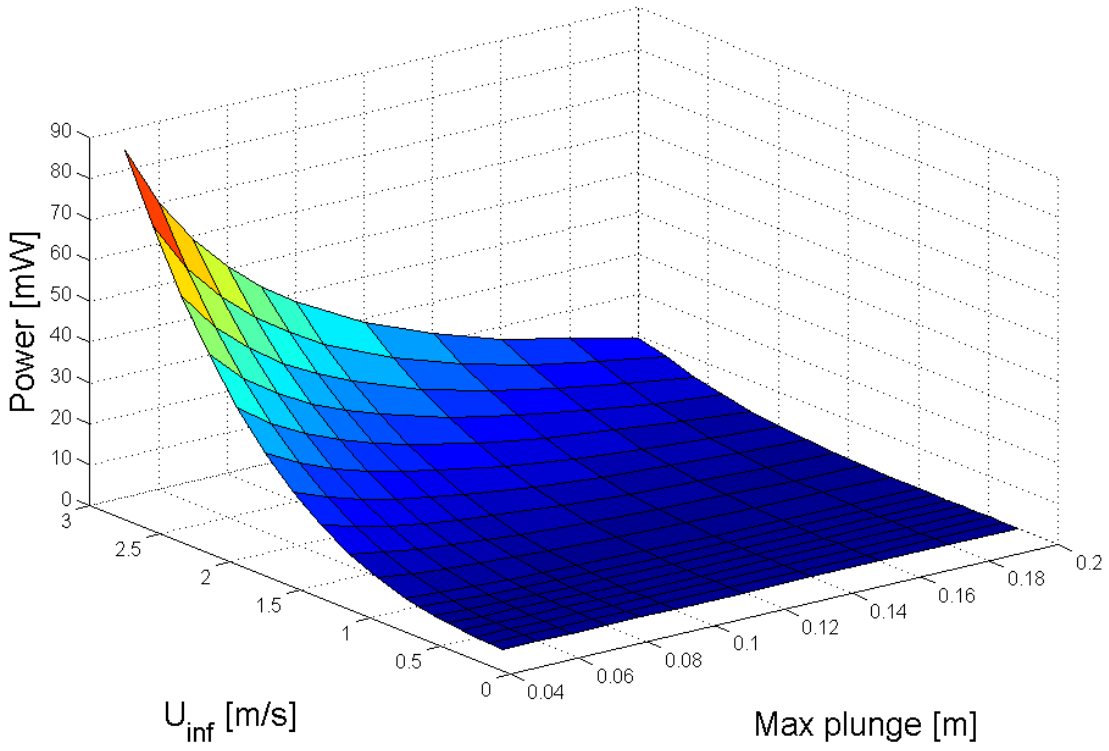


Figure 72: Power generated by a triple-morph beam attached to the wingmill wing when the beam is stressed to the maximum allowable stress of PVDF

The maximum power generated by the triple-morph beam is approximately 90 mW with $w = 36$ mm, $t = 4.1$ mm, and $L = 0.25$ m. The maximum generated power occurs at the greatest free stream velocity and smallest plunge amplitude considered not where the most volume of material but where the highest frequency of oscillation is (similar to the prismatic bar case). The power output of the triple-morph beam is dominated by the frequency of oscillation because, as explained in the Discussion of Results sections of this chapter, the magnitude of the frequency is much greater than the volume of material (again, similar to the prismatic bar case). Therefore, the power can be increased the same way as the prismatic bar case. If the results of Figure 72 are scaled to include the electrode and coating layers the result is Figure 73, which shows a maximum generated power of about 0.18 mW.

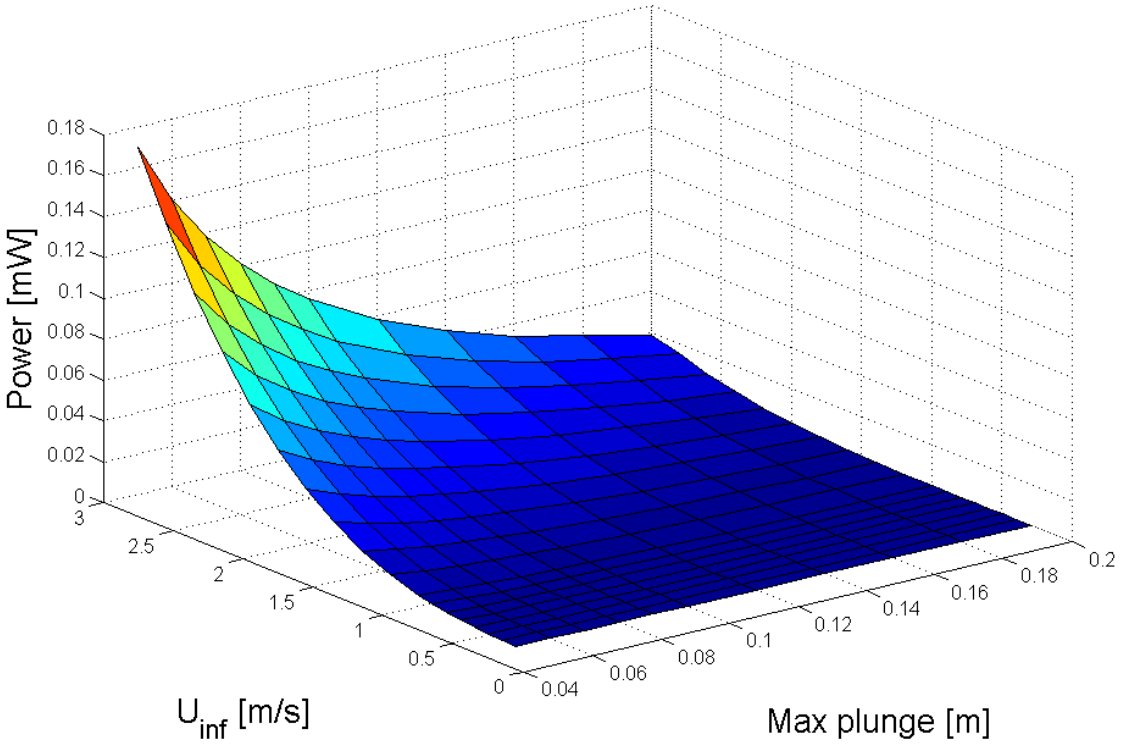


Figure 73: Adjusted generated power of a triple-morph beam attached to the pivot point of the Wingmill wing when the electrode and coating layer effects are included

### 4.3.3 Power Generated by the Electromagnetic Induction Transducer

The equation used to calculate the average electrical power generated by the inductor coils is

$$P_{avg} = \frac{1}{T} \int_{t_o}^{t_o+T} \frac{V^2(t)}{R_{load}} \, dt \tag{4.38}$$

In equation 4.38 T is the total simulation time it took for the wing to oscillate through ten full cycles in seconds, $R_{load}$ is the load resistance, and $V(t)$ is the induced voltage by the inductor. To utilize this equation the following two assumptions were made. The first assumption is the coils move perpendicular to the magnetic field and equation 4.16 represents

the induced voltage in the coils. To calculate the induced voltage the number of turns, length of wire, and magnetic field strength were parameterized. The magnets chosen to be represented in the simulation are neodymium disc magnets with a diameter of 10 mm, therefore the coils are assumed to have an inner diameter of 10 mm. These magnets are assumed to have a maximum magnetic field strength of 0.1 $T$ at a distance of up to 1/16 of its radius around the entire perimeter of the magnet(s). The wire chosen is a 41 $AWG$ copper wire, which is equivalent to having a diameter of 71.12 μm and a resistivity of 1.68X10$^{-8}$ Ωm. The number of turns, N, depends on the specific plunge amplitude, which is one half of the full stroke distance, divided by the diameter of the wire. This will give the number of turns if there is only one layer of wire but since it was assumed that the magnetic field strength is constant up to one sixteenth of the radius of the magnet, with this diameter wire four layers will be allowed. As previously mentioned, the length of the wire is equivalent to the product of the circumference of the coil and the number of turns. Also, the velocity of the magnet will be equivalent to the velocity of the wing, which is determined from the simulation. The second assumption is that the load resistance is equivalent to the resistance of the wire, which is given by equation 4.14. With these assumptions and chosen parameters the electrical power produced by the electromagnetic induction transducer is given by Figure 74.

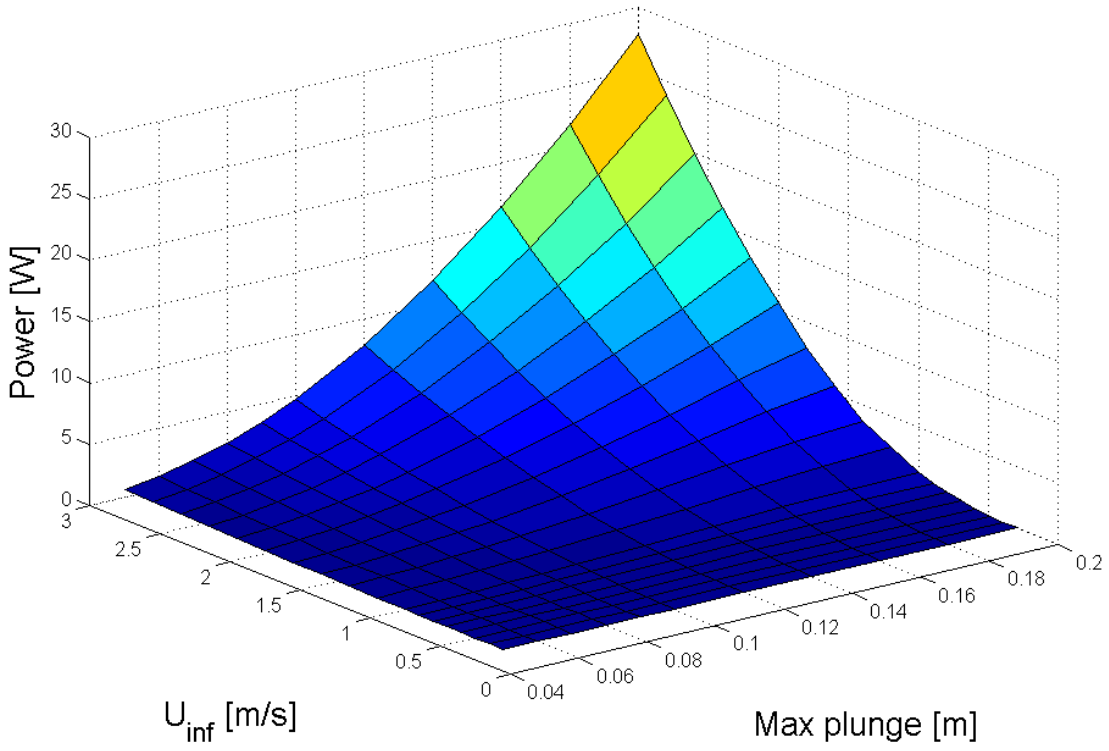


Figure 74: Power generated by the electromagnetic induction transducer

It can be seen that the maximum theoretical power output of the electromagnetic inductor transducer is approximately 27 W and occurs at the maximum plunge and free stream velocity considered. This is expected because for a coil it was mentioned that the induced voltage is proportional to the number of turns of the coil, the length of the wire that makes up the coils, and the velocity of the magnet moving through the coils. It was also mentioned that the length of the wire is $2\pi rN$, which causes the induced voltage to be proportional to the number of turns squared, and for the simulation the number of turns in the coils increases as the plunge amplitude increases. Therefore, it is expected that for a given free stream velocity the power generated by the electromagnetic inductor increases as the plunge amplitude increases, and for a given plunge amplitude the generated power increases as the stream velocity increases.

## 4.4 DISCUSSION OF RESULTS

It is not surprising that the greatest theoretical power for every given plunge amplitude produced by the PVDF and electromagnetic inductor occurred at the maximum considered free stream velocity. However, it is interesting to note that the maximum theoretical power for the PVDF spring geometries occurs at the minimum plunge amplitude for every given free stream velocity. This happens because for a given free stream velocity the maximum frequency of oscillation and minimum volume of material are found at the minimum plunge amplitude, and the generated power is more persuaded by the frequency because of its dominance in magnitude over the volume of smart material. This can be seen Figure 75, which represents the volume of material in the beam spring, and 76, which represents the frequency of oscillation of the wing.

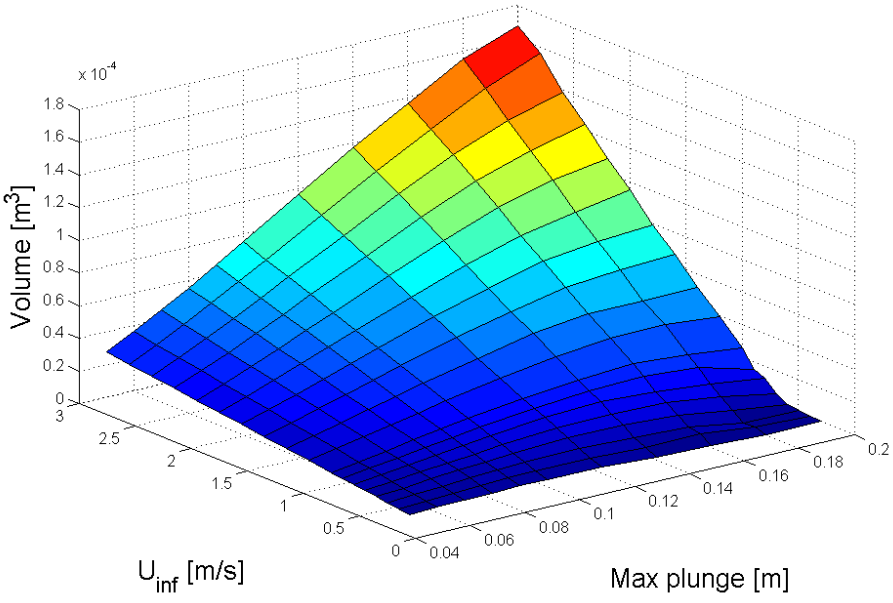


Figure 75: Volume of PVDF material in cantilever beam for a given free stream velocity and plunge amplitude

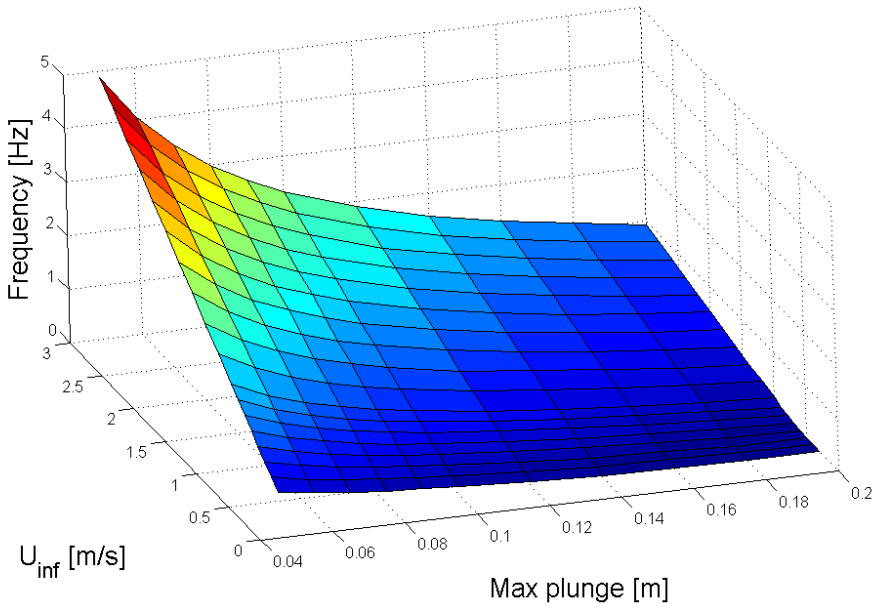


Figure 76: Frequncy of oscillation of the wing for a given free stream velocity and plunge amplitude

Also, a characteristic to notice is the frequency of oscillation has a parabolic relationship with the plunge amplitude and the volume of material seems to only increase linearly as the plunge amplitude is increased. These same trends apply to the prismatic bar geometry as well.

There are two reasons why a wingmill system with the given parameters is not a viable system to harness energy through the PVDF transducer and electromagnetic inductor simultaneously. The first and foremost is because the PVDF generates less than 1 % of the power of the inductor when the elctrode and coating layers are taken into consideration. The second is because of where the maximum theoretical power output for the PVDF transducer and the electromagnetic inductor are located with respect to the plunge amplitude at a given velocity. It would be more suitable to harness energy simultaneously from both transducers if the power generated by the PVDF was at least 10 % of the inductor and the power generated by the PVDF followed the same trend as the inductor. Since it does not and the power generated by the PVDF is negligible compared to the inductor, Figure 77 shows the sum of

the power generated by both of the transducers is still at the maximum power produced by the electromagnetic inductor.

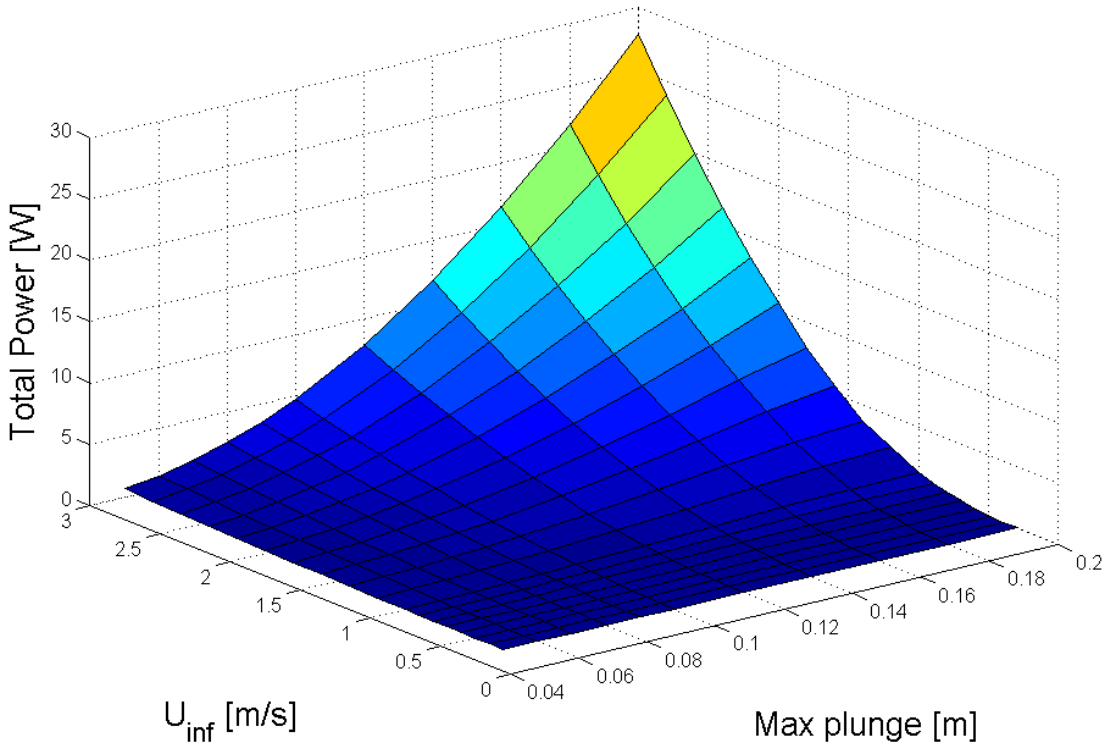


Figure 77: Total power generated by the wingmill system

To get an idea if this total generated power is realistic, it has been compared to the ideal power according to the Betz law [34] shown in Figure 78. It can be seen that the simulation approximates the Wingill to have an efficiency of about 5 % with the given parameters. This efficiency could definitely be increased for the electromagnetics has not been optimized by any means.

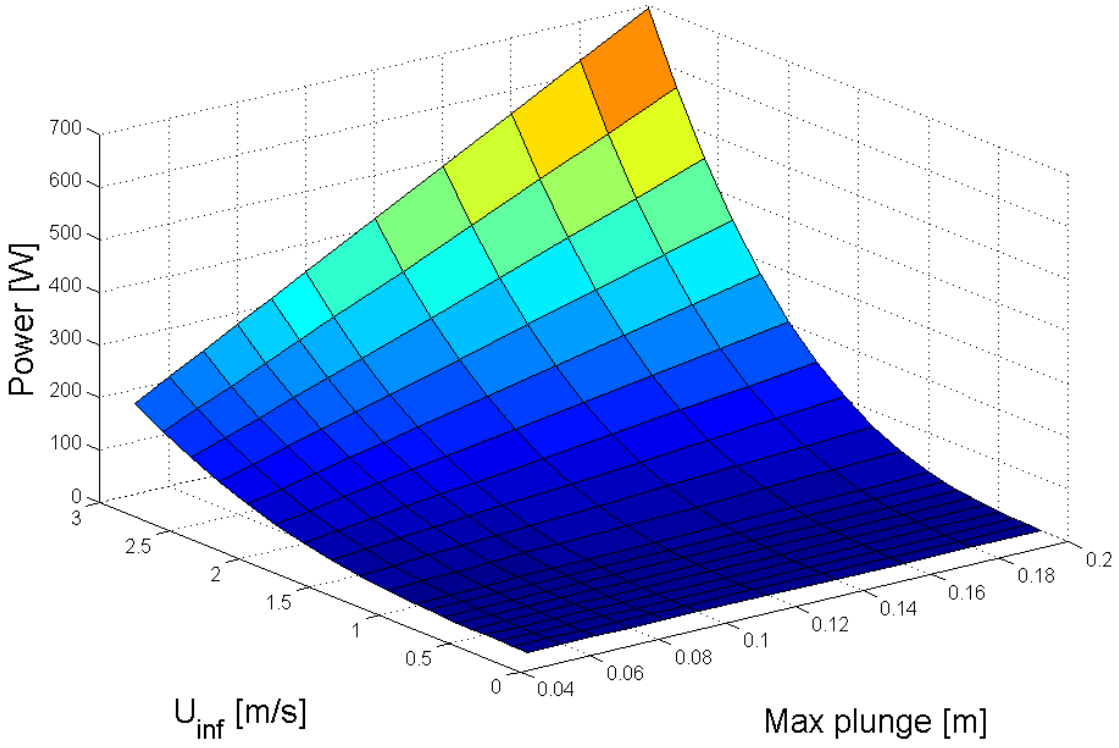


Figure 78: Ideal power according to the Betz law with the wing's width at two times its depth

# 5.0 CONCLUSIONS AND FUTURE RECOMMENDATIONS

The purpose of this thesis was to develop a feasible hydrokinetic energy conversion device that has the three following features:

1. The device must be considered an in-stream device, meaning that it can harness energy from currents.
2. The dynamics of the device must not be rotational.
3. The dynamics of the system are not velocity dependent/sensitive.

It was also expected that this device harness energy simultaneously through smart material and electromagnetic induction transducers.

## 5.1 CONCLUSIONS

The device chosen to be developed and tested was the flapping device revealed in Chapter 2. This device generated on average 25 nW from the PVDF transducer and 77 μW from the electromagnetic inductor transducer. The power rating of this device was calculated to be approximately 68 W per 4456 $m^2$ of surface area (or approximately one American football field), which proves not to be a feasible device for macro-scale power generation. Although, this device proved not to be feasible, one major conclusion was drawn about the smart material transducer that may draw interest in future work and is discussed in the Future Recommendations section.

Because the flapping device was deemed not feasible, it was decided to determine the effects of adding a smart material transducer to an existing hydrokinetic device. Specifically, interest

in how much a smart material transducer could improve the energy conversion efficiency of an existing device was desired. The device that was chosen was the Wingmill system because its characteristics fit perfectly with the three features mentioned. The mechanics of the Wingmill were discussed in Chapters 1 and 4 and a simulation was created to approximate the effects of adding the smart material transducer to the system. To illustrate this, a PVDF spring was attached to the wing of the Wingmill, which oscillates at a certain frequency according to the free stream velocity and plunge amplitude, that allowed this spring to be stressed at that frequency. The purpose of the simulation was to determine the spring stiffness, $k$, value that allowed the system to oscillate for a given pair of plunge amplitude and free stream velocity because it is this value that predicts the maximum power generated by the PVDF spring. The results were given in Chapter 4 in Figure 77. It was determined from the simulation's results that the PVDF generates its maximum power at the minimum plunge amplitudes for a given free stream velocity and the inductor generates most of its power at the maximum plunge amplitudes for a given free stream velocity. Because of this, and the fact that the generated power by the inductor is much greater than the power generated by the PVDF, the results of Figure 77 show that as soon as the plunge amplitude is decreased for a specific free stream velocity the device's overall generated power is decreased. Therefore, it was determined that coupling a PVDF transducer to the Wingmill did not improve the power rating of system.

## 5.2 FUTURE RECOMMENDATIONS

It was mentioned that the flapping device drew a major conclusion that may draw some interest in future work. In specific, the conclusion that was drawn is the effect of the electrode and coating layers on the generated power of PVDF. It was determined that a 28 μm thick element of PVDF with 6 μm thick silver electrodes could produce up to approximately 17.4 % of the theoretical power. When a 100 μm M-coat A polyurethane coating layer is added to protect both of the electrodes, the PVDF could produce up to approximately 0.2 % of the theoretical power. This is obviously detrimental if PVDF is to be used as a hydrokinetic

energy converter because not only do the coating layers protect the electrodes from the harsh environment, they prevent the electrodes from short circuiting as well. To compensate for this reduction in power, more attention must be paid to increasing the material properties of PVDF (e.g. the strain and voltage constants) or simply use a different material with better characteristics for energy harvesting. Also a coating layer that does not effect the output as severely as M-coat A polyurethane must be utilized or use a different design, for example, one that encloses the smart material so that it needs no coating at all. Therefore, if further research is to be done in converting hydrokinetic energy into electrical energy through smart material transducers these are topics that must be addressed.

Simultaneously harnessing hydrokinetic energy through a PVDF and electromagnetic inductor transducer through the Wingmill system (with all of the given parameters in Chapter 4) proved to be ineffective. Although this particular device with the given parameters was not successful in adding a smart material to the system, different parameters that allow a greater volume of material and higher stiffness values may prove to be effective. One way to do this is to increase the plunge amplitude and wing area. Another was that may improve the generated power of the PVDF is to figure out a way to stress the material in a 51-mode. The electromechanical coupling coefficients in this mode are significantly greater than any other mode, but the difficulty in doing this is electroding a mechanical structure that allow these types of stresses. Also, other hydrokinetic energy conversion devices may have a higher energy conversion efficiency (e.g. systems that do not have the three features mentioned at the beginning of this chapter, mainly some of the devices mentioned in Chapter 1) when a smart material is added to the system because it might be found that the generated power of the smart material resembles the trend of the transducer currently utilized on such a device. Therefore, smart materials should not be ruled out as a possible transducer for these other types of devices unless further investigation proves this to be the case.

# APPENDIX A

## CODE DEVELOPED TO DETERMINE THE MINIMUM K VALUES TO ALLOW OSCILLATION.

```
%Model simulation determing the optimal k values utilizing the 4th order
%Runge-Kutta estimation.

clear all, close all, clc
format long
% Conversions
deg2rad = pi/180;

% Constraints
theta_max = 65*deg2rad; %Chosen according to model (Angle where y = 0)
theta_min = -theta_max;

%max plunge values
y_maximum = [0.05 0.06 0.07 0.08 0.09 0.1 0.12 0.14 0.16 0.18 0.2];
U_inf = 1;

% Parameters needed from the user
mass = 0.907;          %Mass (kg) 0.907 kg = 2 lbs.
```

```
for a = 1:length(y_maximum);
    y_max = y_maximum(a);
    y_min = -y_max;
    delta = y_max/500;     %Error on the max and min of y

    k_array= 350:-1:1;     %Must change for each U_inf
    x1 = 0;                %Initialize position check condition

    %Initialize counter
    p = 1;

    while max(x1) < y_max; %Run through values of k until finds the one
        %that allows oscillation
        k = k_array(p);

        % Determine time step and length of simulation
        Wn = sqrt(k/mass);        %Natural freq.
        period = 2*pi/Wn;         %Period of oscillation
        T = period/500;            %Number of time steps per period
        window_length = period*4; %Look at 5 oscillations

        %Give initial conditions
        t(1) = 0;
        Y = [y_max;0];      %Y(1,:) --> Displacement, Y(2,:) --> Velocity
        theta(1) = 0;       %At maximum plunge theta is zero

        n = 1;              %Counter

        %%%%%%%%%%%%%%%%%%%%%%%%%%%%%%%%%%%%%%%%%%%%%%%%%%%%%%%%%%%%%%%%%%%%%%%%%%%
```

```
%Simulation
while t(n) < window_length
    %4th order Runge-Kutta algorithm
    Y(:,n+1) = Y(:,n) +...
        rk4_model(Y(:,n),theta(n),T,k,mass,U_inf,y_max)*T;
    t(n+1) = t(n) + T;

    if sign(Y(2,n+1)) ~= sign(Y(2,n)) & Y(1,n) < y_max-delta &...
            Y(1,n) > y_min+delta;     %Condition that does not
        %want theta to instantaneously change

        if theta(n) >= 0;             %keep theta positive if it is
            %positive at this time
            y_prime = (pi/2)*(Y(1,n+1)/y_max);
            theta(n+1) = theta_max*cos(y_prime);

            n = n+1;
            Y(:,n+1) = Y(:,n) +...
                rk4_model(Y(:,n),theta(n),T,k,mass,U_inf,y_max)*T;
            t(n+1) = t(n) + T;

            y_prime = (pi/2)*(Y(1,n+1)/y_max);
            theta(n+1) = theta_max*cos(y_prime);

            while sign(Y(2,n+1)) == sign(Y(2,n))
                %Stay in loop until another zero crossing
                n = n + 1;
                Y(:,n+1) = Y(:,n) +...
                rk4_model(Y(:,n),theta(n),T,k,mass,U_inf,y_max)*T;
                t(n+1) = t(n) + T;
```

```
        if Y(1,n+1) < y_max & Y(1,n+1) > y_min;
            y_prime = (pi/2)*(Y(1,n+1)/y_max);
            theta(n+1) = theta_max*cos(y_prime);
        else
            theta(n+1) = 0;      %Outside y_max theta = 0
        end
    end

else  %If theta is negetive at this time keep it negetive

    y_prime = (pi/2)*(Y(1,n+1)/y_max);
    theta(n+1) = theta_min*cos(y_prime);

    n = n+1;
    Y(:,n+1) = Y(:,n) +...
        rk4_model(Y(:,n),theta(n),T,k,mass,U_inf,y_max)*T;
    t(n+1) = t(n) + T;

    y_prime = (pi/2)*(Y(1,n+1)/y_max);
    theta(n+1) = theta_min*cos(y_prime);

    while sign(Y(2,n+1)) == sign(Y(2,n))
        %Stay in loop until another zero crossing
        n = n + 1;
        Y(:,n+1) = Y(:,n) +...
        rk4_model(Y(:,n),theta(n),T,k,mass,U_inf,y_max)*T;
        t(n+1) = t(n) + T;

        if Y(1,n+1) < y_max & Y(1,n+1) > y_min;
```

```
                    y_prime = (pi/2)*(Y(1,n+1)/y_max);
                    theta(n+1) = theta_min*cos(y_prime);
                else
                    theta(n+1) = 0;
                end
            end
        end

    else   %Condition where we do not need to worry about theta to
        %change instantaneously
        if Y(2,n+1) >= 0; %If velocity is positive then airfoil is
            %ascending and need to keep theta positive
            if Y(1,n+1) < y_max & Y(1,n+1) > y_min;
                y_prime = (pi/2)*(Y(1,n+1)/y_max);
                theta(n+1) = theta_max*cos(y_prime);
            else
                theta(n+1) = 0;    %Outside y_max theta = 0
            end
        else      %Velocity is negetive then airfoil is
            %descending and need to keep theta negetive
            if Y(1,n+1) < y_max & Y(1,n+1) > y_min;
                y_prime = (pi/2)*(Y(1,n+1)/y_max);
                theta(n+1) = theta_min*cos(y_prime);
            else
                theta(n+1) = 0;     %Outside y_min theta = 0
            end
        end
        n = n + 1;
    end
end
```

```
        %%%%%%%%%%%%%%%%%%%%%%%%%%%%%%%%%%%%%%%%%%%%%%%%%%%%%%%%%%%%%%%%%%%%%%%

        x1 = Y(1,3:length(Y)); %Remove the initial displacement condition
        %so that when I check for the maximum displacement
        %the code does not consider the initial codition
        p = p+1;

    end

    K_opt = k;

end


%%%%%%%%%%%%%%%%%%%%%%%%%%%%%%%%%%%%%%%%%%%%%%%%%%%%%%%%%%%%%%%%%%%%%%%%%%%%%%%
%
%These values of k do consider the contribution to the damping force from
%the electromagnetic induction with B = 0.1 and # turns = amx_plunge * 4
%B = 0.09 for U = 0.2 and y_max = 0.18 and 0.2
%
% K_opt = [9.9 6.2 4 2.63 1.76 1.18 0.5 0.17 0.02 0.01 0.001;...
% 24.24 15.75 10.64 7.38 5.21 3.72 1.9 0.92 0.37 0.1 0.01;...
% 45.2 29.9 20.7 14.7 10.6 7.8 4.3 2.4 1.22 0.55 0.15;...
% 72.4 48.5 34 24.6 18.1 13.6 7.9 4.6 2.62 1.4 0.65;...
% 106 71.5 50.6 36.9 27.5 20.9 12.5 7.6 4.6 2.7 1.42;...
% 146 99 70.5 51.9 39 30 18.4 11.5 7.2 4.5 2.6;...
% 192.4 131 94 69.8 52.8 40.7 25.3 16.2 10.4 6.7 4.2;...
% 245.7 167.7 120.7 89.7 68.5 53.2 33.2 21.5 14.2 9.4 6.1;...
% 305 209 151 112 86 67 42.8 28.2 18.9 12.5 8.5;...
% 443 605 221 165 128 99.8 64.3 43.1 29.6 20.6 14.2;...
```

```
% 607 419 304 229 177 140 91 61.8 43.1 30.4 21.7;...
% 796 550 400 302 235 186 123 83.8 59.2 42.4 30.8;...
% 1011 700 510 386 300 239 158 109.3 77.9 56.5 41.5;...
% 1251 868 634 480 374 298 199 139 99.2 72.3 54;...
% 1518 1054 770 585 457 364 244 171 124 90.8 68;...
% 1810 1258 920 699 547 437 294 207 150 112 83.7;...
% 2128 1480 1084 824 645 516 348 246 179 134 101.5;...
% 2471 1719 1260 959 752 602 407 288 211 158 120.6;...
% 2840 1977 1450 1105 867 695 470 334 246 185 141.4];

%The range of free stream velocities used are
%U = [0.2 0.3 0.4 0.5 0.6 0.7 0.8 0.9 1 1.2 1.4 1.6 1.8 2 2.2 2.4 2.6 2.8
%3];
%%%%%%%%%%%%%%%%%%%%%%%%%%%%%%%%%%%%%%%%%%%%%%%%%%%%%%%%%%%%%%%%%%%%%%%%%%%%
```

# APPENDIX B

## FUNCTION USED TO DETERMINE THE 4TH ORDER RUNGE KUTTA PARAMETERS (RK4MODEL).

```
function dYdt = rk4_model(Y,theta,T,k,mass,U_inf,y_max)
%
%dYdt = rk4_model(Y,theta,T,k,mass,U_inf,y_max)
%
%This is the function that will determine the Ki's for the Runge-Kutta
%approximation.  Y is a 2X1 column vector.
%
%Y = [displacemnt, velocity]
%theta = current angle of airfoil w.r.t. flow field vector
%T = time step
%k - stiffness constant [N/m^2]
%mass - mass of entire system  (including magnets, etc.) [kg]
%U_inf - free stream velocity
%y_max - maximum plunge amplitude [m]

%**************************************************************************
deg2rad = pi/180;
theta_max = 17*deg2rad;   %Arbitrary (Angle where y = 0)
```

```
theta_min = -theta_max;
y_min = -y_max;
Wn = sqrt(k/mass);   %Natural frequency [1/s]
pitch = sin(2*theta)/(4*pi);
zeta = 0.01;         %damping ratio
A_wing = 0.0217;     %Area of wing [m^2]
rho = 1000;          %density of water [kg/m^3]

%Damping force due to the electromagnetic induction
diam_wire = 71.12E-6;         %Diameter of a 41 AWG wire [m]
A_wire = pi*(diam_wire/2)^2;      %cross-sectional area of wire
N = floor(y_max/diam_wire*4);  %Number of turns in the coils

if U_inf == 0.3 & y_max == 0.2;
    B = 0.07;
elseif U_inf == 0.4 & y_max == 0.2;
    B = 0.08;

elseif U_inf <= 0.5 & y_max == 0.18;
    B = 0.09;                 %Magnetic field strength in Tesla
                              %www.coolmagnetman.com reports that a small NIB
                              %(neodymium iron boron) magnet has this field
                              %strength. [T]
else
    B = 0.1;
end

W_coil = y_max;          %Coil width [m]
r_coil = 0.01/2;        %Coil radius [m]
L_wire = pi*2*r_coil*N;%Total length of the wire
```

```
ydot = Y(2)^2*cos(theta)*sign(Y(2))/(U_inf*2*pi);
Cu_res = 1.68E-8;       %Resistivity of copper at ~40 degress Fahrenheit
R = Cu_res*(L_wire/A_wire); %Resistance of wire [Ohms]
c = 2*pi*r_coil*(N*B)^2*W_coil/R;  %Damping coefficient
EMI_damp = c*Y(2);

%Lift force
C_La = 2*pi;  %For thin plates according to Theodorsen theory
Lift = (1/2/mass)*rho*A_wing*U_inf^2*C_La*(pitch - ydot/U_inf);

%************************************************************************

%Approximation #1 - derivative at beginning
K1 = model(Y,theta,k,mass,U_inf,y_max,Lift,EMI_damp);

%Approximation #2 - derivative at mid-point
Y1 = Y + T*K1/2;
K2 = model(Y1,theta,k,mass,U_inf,y_max,Lift,EMI_damp);

%Approximation #3 - second estimate of derivative at mid-point
Y2 = Y + T*K2/2;
K3 = model(Y2,theta,k,mass,U_inf,y_max,Lift,EMI_damp);

%Approximation #4 - derivative at end of interval
Y3 = Y + T*K3;
K4 = model(Y3,theta,k,mass,U_inf,y_max,Lift,EMI_damp);

dYdt = (K1 + 2*K2 + 2*K3 + K4)/6;
return
```

# APPENDIX C

## FUNCTION THAT DETERMINES THE CURRENT DISPLACEMENT AND VELOCITY DEVELOPED BY THE MODEL

```
function K = model(Y,theta,k,mass,U_inf,y_max,Lift,EMI_damp)
%
%dYdt = model(Y,theta,k,mass,U_inf,y_max)
%
%Function used to evaluate the model using the 4th order Runge-Kutta method
%
%Y = [displacement;velocity]
%theta - current angle of airfoil w.r.t. flow field vector
%k - stiffness constant [N/m^2]
%mass - mass of entire system  (including magnets, etc.) [kg]
%U_inf - free stream velocity
%y_max - maximum plunge amplitude [m]
%Fext - Input force from free stream velocity
%Fluid_damp - damping force from fluid
%EMI_damp - damping force from electromagnetic induction

deg2rad = pi/180;
theta_max = 65*deg2rad;   %Arbitrary (Angle where y = 0)
```

```
theta_min = -theta_max;
y_min = -y_max;

Wn = sqrt(k/mass);   %Natural frequency [1/s]
zeta = 0.01;         %damping ratio
A_wing = 0.0217;     %Area of wing [m^2]
rho = 1000;          %density of water [kg/m^3]

%Equation of motion
K = [Y(2); Lift-Wn^2*Y(1)-2*zeta*Wn*Y(2)-EMI_damp];
```

# APPENDIX D

## CODE DEVELOPED TO DETERMINE THE POWER GENERATED BY THE TRIPLE-MORPH BEAM ATTACHED TO THE WINGMILL SYSTEM.

```
%%% Determines the beam dimensions based off of the stiffness and max
%%% plunge values, then the power produced from the beam is determined.
%%% This code limits the length of the beam to be 5 times the maximum
%%% plunge and then determines the thickness of the PVDF so that the stress
%%% in the outer layer of the PVDF does not excedd the maximum stress.
%%% There are no constraints on the width for it will be used to keep the
%%% desired stiffness.

clear all, close all, clc

%Free stream velocities
U=[0.2 0.3 0.4 0.5 0.6 0.7 0.8 0.9 1 1.2 1.4 1.6 1.8 2 2.2 2.4 2.6 2.8 3];
%max plunge values
y_maximum = [0.05 0.06 0.07 0.08 0.09 0.1 0.12 0.14 0.16 0.18 0.2];
%Optimum K values - K values are determined so that for every given flow
%velocity and max plunge these are the maximum values of the spring
%constant that allow the device to oscillate.  Anything higher than these
%values for each specific case the spring is too stiff and the device will
%not oscillate.
```

```
K_opt = [7 4.4 2.8 1.8 1.2 0.7 0.24 0.03 0.01 0.0005 0.0005;...
13 8 5.5 3.8 2.6 1.7 0.7 0.22 0.12 0.01 0.001;...
21 14 9 6.5 4.7 3.3 1.5 0.5 0.2 0.01 0.005;...
31 20 14 10 7 5 2.7 1.3 0.5 0.1 0.01;...
43 28 20 14 10 7.5 4 2 1 0.3 0.05;...
57 38 27 19 14.3 10.5 6 3.3 1.5 0.6 0.2;...
73 49 35 25 18 14 8 4.5 2.5 1.2 0.3;...
91 61 43 32 24 18 10 6 3.5 1.7 0.8;...
133 90 63 47 35 27 16 10 6 3.5 1.8;...
181 123 88 65 49 38 23 15 9 5 3;...
238 163 117 87 66 51 32 20 13 8 5;...
303 207 149 111 85 66 42 27 18 11 7;...
375 257 186 139 107 84 53 35 23 15 10;...
455 313 226 170 131 103 66 44 30 20 13;...
544 374 271 203 157 124 80 54 37 25 17;...
639 440 319 240 186 147 95 65 45 31 21;...
743 512 372 280 217 171 112 76 53 38 27;...
854 589 428 323 250 198 130 89 62 45 31];
K_opt = K_opt';

sizek = size(K_opt);

%%% Parameters and material constants
A_wing = 0.0217;        %Wing area (m^2)
rho = 999;              %density of water (kg/m^3)
mass = 0.907;           %Mass (kg) 0.907 kg = 2 lbs.

E1 = 0.01E9;            %Elastic modulus of rubber metal (acts as substrate)
E2 = 3E9;               %Elastic modulus of PVDF
stress_max = 29.6E6;    %maximum stress in PVDF before plastic deformation
```

```
d31 = 23E-12;          %Strain constant of PVDF in 31 mode
g31 = 216E-3;          %Voltage constant of PVDF 31 mode
e33 = 110E-12;         %Permittivity constant [F/m]
sm = 1/E1;             %elastic compliance of substrate
s11 = 1/E2;            %elastic compliance of PVDF

%%% I need to pick the thickness of the substrate so that there is only one
%%% variable which is the PVDF thickness
h1 = 3E-6;     %Therefore the whole thickness of the substrate is 6 micron

%%% Determine the thickness of the beam so that the PVDF is not stress
%%% higher than the maximum allowable stress before plastic deformation

%%% Make the thickness of the PVDF a variable
h2_vec = 1E-3:1E-5:1E-1;

%%% Determine the corresponding thicknesses for each specific plunge
%%% amplitudes and the corresponding widths for each specific free stream
%%% velocities
for i = 1:sizek(1);
    y_max = y_maximum(i);
    L = y_max*5;
    c = h1+h2_vec;
    stress1 = 3*E2*c*y_max/L^2;
    h2_opt(i) = interp1(stress1,h2_vec,29.6E6);

    for j = 1:sizek(2);
        k = K_opt(i,j);
        I = (1/12)*(E1/E2)*(2*h1)^3 + 2*(1/12)*h2_opt(i)^3 +...
            2*h2_opt(i)*(h1+0.5*h2_opt(i)).^2;
```

```
        W(i,j) = k*y_max*L*(h1+h2_opt(i))/(stress_max*I);

    end
end

%%% Determine the frequency of oscillation

for m = 1:sizek(1);
    for n = 1:sizek(2);

        k = K_opt(m,n);           %Current stiffness constant
        Wn = sqrt(k/mass);        %Natural freq.
        period = 2*pi/Wn;         %Period of oscillation
        freq(m,n) = 1/period;     %frequency

    end
end

%%% Determine the power produced by the PVDF beam
for x = 1:sizek(1);
    y_max = y_maximum(x);
    L = y_max*5;
    h2 = h2_opt(x);

    for y = 1:sizek(2);
        w2 = W(x,y);
        k = K_opt(x,y);

        X = 12*sm*h2^2*h1 + 8*sm*h2^3 + 6*sm*h2*h1^2 + s11*h1^3;
        K31 = d31/sqrt(e33*s11);
```

```
        N = 18*d31^2*sm^2*h2*(h1+h2)^2*L^3;
        D = e33*w2*X^2*(1+(((6*sm*h2*(h1+h2)^2)/X)-1)*K31^2);

        I = (1/12)*(E1/E2)*h1^3 + 2*(1/12)*h2^3 + 2*h2*(h1+0.5*h2).^2;
        Fo(x,y) = k*y_max;
        Energy = (1/2)*(N/D)*max(Fo(x,y))^2;  %Energy produced from device
        P(x,y) = Energy*2*freq(x,y);          %Power of PVDF, bimorph beam

        Vol(x,y) = (2*h2)*L*(2*w2);

        Stress(x,y) = k*y_max*L*(h1+h2)/(w2*I);
    end
end

[Q,Plunge] = meshgrid(U,y_maximum);

figure(1)
surf(Plunge,Q,P*0.002*1000)
xlabel('Max plunge [m]','Fontsize',20)
ylabel('U_i_n_f [m/s]','Fontsize',20)
zlabel('Power [mW]','Fontsize',20)
%title('Power production of PVDF bimorph beam')

figure(2)
surf(Plunge,Q,Vol)
xlabel('Max plunge [m]')
ylabel('U_i_n_f [m/s]')
zlabel('Volume [m^3]')
title('Volume of PVDF in beam for each specific scenario')
```

```
figure(3)
plot(y_maximum,h2_opt)
xlabel('Max plunge [m]','Fontsize',20)
ylabel('t_2 [m]','Fontsize',20)
%title('Thickness, h2, of PVDF needed to stress it to 26.9 MPa')

figure(4)
surf(Plunge,Q,W)
xlabel('Max plunge [m]','Fontsize',20)
ylabel('U_i_n_f [m/s]','Fontsize',20)
zlabel('Width [m]','Fontsize',20)
%title('Width of beam needed for each scenario to reach desired stiffness')
```

# APPENDIX E

## CODE DEVELOPED TO DETERMINE THE POWER GENERATED BY THE AXIALLY STRESSED PVDF MEMBER ATTACHED TO THE WINGMILL SYSTEM AND THE POWER GENERATED BY THE ELECTROMAGNEITC INDUCTOR TRANSDUCER.

```
%Model simulation utilizing the 4th order Runge-Kutta estimation
%
%Calculating the power production of the inductor and PVDF that is axially
%stressed

clear all, close all, clc
format long
% Conversions
deg2rad = pi/180;

%Free stream velocities
U=[0.3 0.4 0.5 0.6 0.7 0.8 0.9 1 1.2 1.4 1.6 1.8 2 2.2 2.4 2.6 2.8 3];

%max plunge values
y_maximum = [0.05 0.06 0.07 0.08 0.09 0.1 0.12 0.14 0.16 0.18 0.2];
```

```
%Optimum K values
K_opt = [7 4.4 2.8 1.8 1.2 0.7 0.24 0.03 0.01 0.0005 0.0005;...
13 8 5.5 3.8 2.6 1.7 0.7 0.22 0.12 0.01 0.001;...
21 14 9 6.5 4.7 3.3 1.5 0.5 0.2 0.01 0.005;...
31 20 14 10 7 5 2.7 1.3 0.5 0.1 0.01;...
43 28 20 14 10 7.5 4 2 1 0.3 0.05;...
57 38 27 19 14.3 10.5 6 3.3 1.5 0.6 0.2;...
73 49 35 25 18 14 8 4.5 2.5 1.2 0.3;...
91 61 43 32 24 18 10 6 3.5 1.7 0.8;...
133 90 63 47 35 27 16 10 6 3.5 1.8;...
181 123 88 65 49 38 23 15 9 5 3;...
238 163 117 87 66 51 32 20 13 8 5;...
303 207 149 111 85 66 42 27 18 11 7;...
375 257 186 139 107 84 53 35 23 15 10;...
455 313 226 170 131 103 66 44 30 20 13;...
544 374 271 203 157 124 80 54 37 25 17;...
639 440 319 240 186 147 95 65 45 31 21;...
743 512 372 280 217 171 112 76 53 38 27;...
854 589 428 323 250 198 130 89 62 45 31];
K_opt = K_opt';

b = size(K_opt);

% Constraints
theta_max = 65*deg2rad; %Arbitrary (Angle where y = 0)
theta_min = -theta_max;

% Parameters
A_wing = 0.0217;       %Wing area (m^2)
```

```
rho = 999;              %density of water (kg/m^3)
mass = 0.907;           %Mass (kg) 0.907 kg = 2 lbs.

% Material parameters
E1 = 0.01E9;        %Elastic modulus of rubber metal (acts as substrate)
E2 = 3E9;           %Elastic modulus of PVDF
t1 = 6E-6;          %Assumed thickness of rubber metal
t2 = 110E-6;         %Thickness of PVDF

stress_max = 29.6E6;    %maximum stress in PVDF before plastic deformation
d31 = 23E-12;           %Strain constant of PVDF in 31 mode
g31 = 216E-3;           %Voltage constant of PVDF 31 mode
e33 = 110E-12;          %Permittivity constant [F/m]
sm = 1/E1;              %elastic compliance of substrate
s11 = 1/E2;             %elastic compliance of PVDF

for p = 1:b(1);
    y_max = y_maximum(p);  %Max plunge amplitude
    delta = y_max/500;
    y_min = -y_max;

    for q = 1:b(2);

        U_inf = U(q);       %Current free stream velocity
        k = K_opt(p,q);     %Current stiffness constant

        % Determine time step and length of simulation

        Wn = sqrt(k/mass);        %Natural freq.
        period = 2*pi/Wn;         %Period of oscillation
```

```
freq(p,q) = 1/period;     %frequency
T = period/500;           %500 time steps per period
window_length = period*3; %Look at 5 oscillations

%Give initial conditions
t(1) = 0;
Y = [y_max;0];      %Y(1,:) --> Displacement, Y(2,:) --> Velocity
theta(1) = 0;       %At maximum plunge theta is zero

n = 1;              %Counter

%%%%%%%%%%%%%%%%%%%%%%%%%%%%%%%%%%%%%%%%%%%%%%%%%%%%%%%%%%%%%%%%%%%%%%%%%%%%
%Simulation
while t(n) < window_length
    %4th order Runge-Kutta algorithm
    [dYdt,Fext] =...
        rk4_model_inputforce(Y(:,n),theta(n),T,k,mass,U_inf,y_max);
    F_in(n) = Fext;
    Y(:,n+1) = Y(:,n) + dYdt*T;
    t(n+1) = t(n) + T;

    if sign(Y(2,n+1)) ~= sign(Y(2,n)) & Y(1,n) < y_max-delta &...
            Y(1,n) > y_min+delta;      %Condition where we do not
        %want theta to instantaneously
        %change

        if theta(n) >= 0;            %keep theta positive if it is
            %positive at this time
            y_prime = (pi/2)*(Y(1,n+1)/y_max);
            theta(n+1) = theta_max*cos(y_prime);
```

```
n = n+1;
[dYdt,Fext] = rk4_model_inputforce(Y(:,n),theta(n),...
    T,k,mass,U_inf,y_max);
F_in(n) = Fext;
Y(:,n+1) = Y(:,n) + dYdt*T;
t(n+1) = t(n) + T;

y_prime = (pi/2)*(Y(1,n+1)/y_max);
theta(n+1) = theta_max*cos(y_prime);

while sign(Y(2,n+1)) ==...
        sign(Y(2,n)) & t(n) < window_length
    %Stay in loop until
    %another zero crossing
    n = n + 1;
    [dYdt,Fext] = rk4_model_inputforce(Y(:,n),...
        theta(n),T,k,mass,U_inf,y_max);
    F_in(n) = Fext;
    Y(:,n+1) = Y(:,n) + dYdt*T;
    t(n+1) = t(n) + T;

    if Y(1,n+1) < y_max & Y(1,n+1) > y_min;
        y_prime = (pi/2)*(Y(1,n+1)/y_max);
        theta(n+1) = theta_max*cos(y_prime);
    else
        theta(n+1) = 0;     %Outside y_max theta = 0
    end
end
```

```
else   %If theta is negetive at this time keep it negetive

    y_prime = (pi/2)*(Y(1,n+1)/y_max);
    theta(n+1) = theta_min*cos(y_prime);

    n = n+1;
    [dYdt,Fext] = rk4_model_inputforce(Y(:,n),theta(n),...
        T,k,mass,U_inf,y_max);
    F_in(n) = Fext;
    Y(:,n+1) = Y(:,n) + dYdt*T;
    t(n+1) = t(n) + T;

    y_prime = (pi/2)*(Y(1,n+1)/y_max);
    theta(n+1) = theta_min*cos(y_prime);

    while sign(Y(2,n+1)) ==...
            sign(Y(2,n)) & t(n) < window_length
        %Stay in loop until
        %another zero crossing
        n = n + 1;
        [dYdt,Fext] = rk4_model_inputforce(Y(:,n),...
            theta(n),T,k,mass,U_inf,y_max);
        F_in(n) = Fext;
        Y(:,n+1) = Y(:,n) + dYdt*T;
        t(n+1) = t(n) + T;

        if Y(1,n+1) < y_max & Y(1,n+1) > y_min;
            y_prime = (pi/2)*(Y(1,n+1)/y_max);
            theta(n+1) = theta_min*cos(y_prime);
        else
```

```
                theta(n+1) = 0;
            end
        end
    end

else  %Condition where we do not need to worry about theta to
    %change instantaneously
    if Y(2,n+1) >= 0;  %If velocity is positive then airfoil
        %is ascending and need to keep theta positive
        if Y(1,n+1) < y_max & Y(1,n+1) > y_min;
            y_prime = (pi/2)*(Y(1,n+1)/y_max);
            theta(n+1) = theta_max*cos(y_prime);
        else
            theta(n+1) = 0;    %Outside y_max theta = 0
        end
    else             %Velocity is negetive then airfoil is
        %descending and need to keep theta negetive
        if Y(1,n+1) < y_max & Y(1,n+1) > y_min;
            y_prime = (pi/2)*(Y(1,n+1)/y_max);
            theta(n+1) = theta_min*cos(y_prime);
        else
            theta(n+1) = 0;     %Outside y_min theta = 0
        end
    end
    n = n + 1;
end
end
%%%%%%%%%%%%%%%%%%%%%%%%%%%%%%%%%%%%%%%%%%%%%%%%%%%%%%%%%%%%%%%%%%%%%%%%%%%%

%%%%%%%%%%%%%%%%%%%%%%%%%%%%%%%%%%%%%%%%%%%%%%%%%%%%%%%%%%%%%%%%%%%%%%%%%%%%
```

```
% Calculate the generated power from Electromagnetic Induction
% Assumptions for the following calculations:
%   1) The length of the magnets are much longer than the length
%   of the coils so that the magnetic field remains constant.
%   2) All coils cut through the magnetic field at a 90 degree
%      angle.
%       Because of the previous 2 assumptions the equation used to
%       determine the power output from the induction is V = NBLv
%       N - # of turns in coil
%       B - magnetic field strength
%       L - length of coil
%       v - velocity of magnet moving throung coil
%   3) The number of turns in the coils is dependent on the plunge
%   depth.

EMI_Pow(p,q) = emi_power(Y(2,:),y_max,U_inf,window_length,T);

%%%%%%%%%%%%%%%%%%%%%%%%%%%%%%%%%%%%%%%%%%%%%%%%%%%%%%%%%%%%%%%%%%%%%%%

Betz_Pow(p,q) = (1/2)*(16/27)*rho*0.217*(2*y_max)*U_inf^3;

vel_profile(p,q) = max(Y(2,:));

% Power generated by PVDF as an axially stressed member
% Minimum length of material needed to keep stresses in elastic
% region
%L_min_ax(p,q) = max(Y(1,:))*(2*E1*t1+E2*t2)/((t2+2*t1)*stress_max)
L_min_ax(p,q) = max(Y(1,:))*E2/stress_max;
```

```
        % Corresponding width
        %w_ax(p,q) = k*L_min_ax(p,q)/(2*E1*t1+E2*t2);
        w_ax(p,q) = k*L_min_ax(p,q)/(E2*t2);

        %A_ax = w_ax(p,q)*(t2+2*t1);
        A_ax = w_ax(p,q)*t2;
        Vol_ax(p,q) = A_ax*w_ax(p,q);
        F_ax = k*Y(1,:);
        stress_ax = F_ax/A_ax;
        freq(p,q) = 1/period;
        P_ax(p,q) =...
            max(stress_ax)^2*d31*g31*w_ax(p,q)*t2*L_min_ax(p,q)*(1/period);

    end
end

[Q,Plunge] = meshgrid(U,y_maximum);

figure(1)
surf(Plunge,Q,vel_profile)
xlabel('Max plunge [m]')
ylabel('U_i_n_f [m/s]')
zlabel('maximum velocity')
title('Maximum Velocity Profile')

figure(2)
surf(Plunge,Q,EMI_Pow)
xlabel('Max plunge [m]','Fontsize',20)
ylabel('U_i_n_f [m/s]','Fontsize',20)
zlabel('Power [W]','Fontsize',20)
```

```
%title({'Power produced via Electromagnetic Induction';...
%'B-field = 0.1 Tesla'})

figure(3)
surf(Plunge,Q,Betz_Pow)
xlabel('Max plunge [m]','Fontsize',20)
ylabel('U_i_n_f [m/s]','Fontsize',20)
zlabel('Power [W]','Fontsize',20)
%title({'Maximum Power Extracted from the Water according to the Betz Law';
%'(Airfoil width is twice as long as its depth)'})

figure(4)
surf(Plunge,Q,freq)
xlabel('Max plunge [m]','Fontsize',20)
ylabel('U_i_n_f [m/s]','Fontsize',20)
zlabel('Frequency [Hz]','Fontsize',20)

figure(5)
surf(Plunge,Q,P_ax*0.002*1000)
xlabel('Max plunge [m]','Fontsize',20)
ylabel('U_i_n_f [m/s]','Fontsize',20)
zlabel('Power [mW]','Fontsize',20)
```

# BIBLIOGRAPHY


[1] Assessment of Waterpower Potential and Development Needs. EPRI, Palo Alto, CA: 2007. 1014762.

[2] Piezo systems, internet product data specifications. Piezo Systems Inc., 186 Massachusetts Avenue, Cambridge MA 02139. USA, 617-547-1777, 1993.

[3] Piezo film sensors technical manual, internet version. Measurement Specialties, Inc., P.O. Box 799, Valley Forge, PA 19482, 610.650.1500, August 1998. www.msiusa.com.

[4] "status, research and development priorities; wave and marine current energy". DTI report number FES-R-132, AEAT report number AEAT/ENV/1054, 2003.

[5] Proceedings of the Hydrokinetic and Wave Energy Technologies Technical and Environmental Issues Workshop. Washington D.C. October 26-29, 2005. Prepared by RESOLVE, Inc., Washington, D.C., Susan Savitt Schwartz, ed., March 2006. [Proceedings (including slide presentations) may be downloaded from: http://hydropower.inl.gov/].

[6] http://www.supermagnetman.net/, March 2008. [Active].

[7] Electricity Net Generation From Renewable Energy by Energy Use Sector and Energy Source, Table 3. Energy Information Administration, 2009. [May be downloaded from: http://www.eia.doe.gov/cneaf/alternate/page/renewenergyconsump/table3.html].

[8] The pelamis wave energy converter. http://www.pelamiswave.com/content.php?id161, April 2009. [Active].

[9] Verdant power technology. http://www.verdantpower.com/, April 2009. [Active].

[10] Wave dragon technology. http://www.wavedragon.net/, April 2009. [Active].

[11] Willis Owuor Agutu. Characterization of electromagnetic induction damper. Master's thesis, Miami University, 2007.

[12] E. Anderson, M. Freeman, and C. Pringle. Ecological consequences of hydropower development in central america. River research and applications, 2006.

[13] Astroturf. http://www.astroturfusa.com/, May 2009. [Active].

[14] N.J. Baker, M.A. Mueller, M. Watchorn, S. Slee, L. Haydock, and N. Brown. "direct drive power take off for the stingray tidal current generator". University of Durham, UK The Engineering Business Limited Riding Hill, Northumberland, UK.

[15] Roger Bedard. Epri river in stream energy conversion (risec) feasibility study proposal - skagit river watershed. EPRI Ocean Energy, November 2006.

[16] M. M. Bernitsas, K. Raghavan, Y. Ben-Simon, and E. M. H. Garcia. Viivace (vortex induced vibration aquatic clean energy): A new concept in generation of clean adn renewable energy from fluid flow. Department of Naval Architecture and Marine Engineering, University of Michigan, June 2006.

[17] G. Buiques, I. Zamora, A.J. Mazon, V. Valverde, and F.J. Perez. "sea energy conversion: Problems and possibilities". E.T.S.I.I., University of Basque Country, 2005.

[18] Joseph R. Burns. Ocean Wave Energy Conversion Using Piezoelectric Material Members, U.S. patent number 4685296, 1987.

[19] Charles B. Carroll. Frequency Multiplying Piezoelectric Generators, U.S. patent number 5814921, 1998.

[20] William W. Clark and Michael J. Ramsey. Smart material transducers as power sources for mems devices. Technical report, International Symposium on Smart Structures and Microsystems, 2000.

[21] Scott T. Davids. A computational and experimental investigation of a flutter generator. Master's thesis, Naval Postgraduate School, 1999.

[22] Michael Y. Epstein. Piezoelectric Generation of Electrical Power From Surface Waves on Bodies of Water Using Suspended Weighted Members, U.S. patent number 5578889, 1996.

[23] Federal Energy Regulatory Commission. Hydropower - industry activities. http://www.ferc.gov/, October 2008. [Active].

[24] Finavera Renewables. Wave tech: System configuration. http://www.finavera.com/en/wavetech/configuration, April 2009. [Active].

[25] Elizabeth Maloney-Hahn Garcia. *Prediction by Energy Phenomenology for Harnessing Hydrokinetic Energy Using Vortex-Induced Vibrations.* PhD thesis, University of Michigan, 2008.

[26] Alexander Gorlov. Waving in energy. International Water and Power Dam Construction, 55(7), pp 29-29, 2003.

[27] Alexander M. Gorlov. Hydraulic cross-flow turbines. INEEL, October 2005.

[28] George Hagerman. U.s. marine renewable energy resource potential and technology status. Global Marine Renewable Energy Conference, April 2008.

[29] David Halliday, Robert Resnick, and Jearl Walker. Fundamentals of physics 6th edition. John Wiley & Sons, 2002.

[30] Gabor Harsanyi. Polymer films in sensor applications. CRC, July 1995.

[31] IEEE std. 176. Ieee standards on piezoelectricity. The Institute of Electrical and Electronics Engineers, 1978.

[32] D.J. Inman. *Engineering Vibration Second Edition*. Prentice Hall, Inc., 2001.

[33] B. Jaffe, R. Cook, and H. Jaffe. Piezoelectric ceramics. New York: Academic Press.

[34] G.L. Johnson. Wind energy systems. Prentice Hall, Inc., Englewood Cliffs, NJ, 1985.

[35] Kevin D. Jones, Max F. Platzer, and Scott Davids. Oscillating-wingpower generation. 3rd ASME/JSME Joint Fluids Engineering Conference FEDSM99-7050, July 1999.

[36] Sunghwan Kim. *Low Power Energy Harvesting With Piezoelectric Generators*. PhD thesis, University of Pittsburgh, 2002.

[37] Eric A. Kolm and Henry H. Kolm. Piezoelectric Fluid-Electric Generator, U.S. patent number 4387318, 1983.

[38] Donald J. Leo. *Engineering Analysis of Smart Material Systems*. John Wiley & Sons, 2007.

[39] Keon Lindsey. A feasibility study of oscillating-wing power generators. Master's thesis, Naval Postgraduate School, 2002.

[40] W. McKinney and J. Delaurier. The wingmill: An oscillating-wing windmill. *Journal of Energy*, V.5: no.2:109–115, 1981.

[41] Measurement Specialties Inc. Piezo film sensors. http://www.meas-spec.com/piezo-film-sensors.aspx, March 2009. [Active].

[42] P. Mesien and T. Hammons. "harnessing the untapped energy potential of the oceans: Tidal, wave, currents and otec". IEEE 2005 General Meeting, San Francisco, 2005.

[43] G. Miller, J. Francheschi, W. Lese, and J. Rico. The allocation of kinetic hydroelectric conversion systems (khecs) in usa drainage basins. Department of Applied Science, New York University, NY, August 1986.

[44] V. V. Miller and L. A. Schaefer. Dynamic modeling of hydrokinetic energy extraction. ASME IMECE, November 2008.

[45] E. Minazara, D. Vasic, and F Costa. Piezoelectric generator harvesting bike vibrations energy to supply portable devices. Technical report, Universite de Cergy-Pontoise, 2007.

[46] Oceanlinx. Electrical power. http://www.oceanlinx.com/electrical.asp, April 2009. [Active].

[47] Patent Application Publication. Extracting power from a fluid flow. us 2005/0099011 a1, 2005.

[48] S. Pobering and N. Schwesinger. A novel hydropower harvesting device. Munich University of Technology.

[49] M. Previsic and R. Bedard. River in-stream energy conversion (risec) characterization of alaska sites. EPRI-RP-003-Alaska, February 2008.

[50] S. Priya, Chih-Ta Chen, D. Fye, and J. Zahnd. Piezoelectric windmill: A novel solution to remote sensing. *Japanes Journal of Applied Physics*, 44:L104–L107, 2005.

[51] Wayne Saslow. Electricity, magnetism and light. Thomas Learning, 2002.

[52] J. G. Smith. Dynamic admittance matrix of piezoeletric cantilever bimorphs. *Journal of Microelectromechanical systems*, Vol.3 No.3:pp:105–112, 1994.

[53] Moncef B. Tayahi, Bruce Johnson, and Melinda Hotzman. Piezoelectric materials for powering wireless remote sensors. Technical report, University of Nevada, Reno, 2002.

[54] Geroge W. Taylor and Joseph R. Burns. Power Generation From Waves Near The Surface of Bodies of Water, U.S. patent number 4404490, 1983.

[55] Open Hydro Tidal Technologies. http://www.openhydro.com/, April 2009. [Active].

[56] The Engineering Business Ltd. Research and development of a 150 kw tidal stream generator. ETSU T/06/00230/00/REP, DTI pub URN no 05/864, 2005. [can be downloaded from: http://www.engb.com].

[57] A. M. Vinogradov, V. H. Schmidt, G. F. Tuthill, and B. W. Bohannan. Damping and electromechanical energy losses in the piezoelectric polymer pvdf. Mechanics of Materials, March 2003. [Available online at www.sciencedirect.com].

[58] Vortex Oscillation Technology Ltd. Wind - hydrogenerators with oscillating working bodies. http://www.vortexosc.com/modules, April 2009. [Active].

[59] Zaar, Linda F. [lfzarr@usgs.gov]. Long-form measurement discharge summary for station number 03048500 kiskiminetas river at vandergrift, pa. Private e-mail message to A. Michael Hudzik II [amh59@pitt.edu], 27 March 2009.